Seismic Methods Applied to Ultrasonic Testing in Civil Engineering

Von der Fakultät für Geowissenschaften und Materialtechnik
der Rheinisch-Westfälischen Technischen Hochschule Aachen genehmigte

Habilitationsschrift

von Dr. rer. nat. Ernst Axel Niederleithinger aus Potsdam

Gutachter: Univ.-Prof. Dr. rer. nat. Christoph Clauser

Prof. John S. Popovic, Ph. D.

Prof. Dr.-Ing. habil. Dipl.-Geophys. Christian Große

Tag der Habilitation: 29. 11. 2017

Seismic Methods Applied to Ultrasonic Testing in Civil Engineering

Habilitation Thesis

RWTH Aachen, Faculty of Georesources and Materials Engineering

Dr. rer. nat. Ernst Axel Niederleithinger

Wagnerstr. 16

14480 Potsdam

e.niederleithinger@posteo.de

Version revised for publication 2019-10-29

Content

List of Figures

List of Tables

List of papers used in this thesis and personal contribution

1) *Section 2.1*: Ernst Niederleithinger, Odile Abraham, Mike Mooney: Geophysical Methods in Civil Engineering. Editorial to Near Surface Geophysics special issue, 2016.
Contribution: main author and leading guest editor.
2) ** Section 4.4:* Ernst Niederleithinger, Julia Wolf, Frank Mielentz, Herbert Wiggenhauser, und Stephan Pirskawetz: "Embedded Ultrasonic Transducers for Active and Passive Concrete Monitoring". *Sensors* 15, Nr. 5 (27. April 2015): 9756–72. doi:10.3390/s150509756.
Contribution: Main Author, theoretical background, design, performance, and evaluation of two of three application experiments.
3) ** Section 5.2*: Sabine Müller, Ernst Niederleithinger and Thomas Bohlen: "Reverse Time Migration: A Seismic Imaging Technique Applied to Synthetic Ultrasonic Data". International Journal of Geophysics, Volume 2012, Article ID 128465, doi:10.1155/2012/128465, accepted 25 May 2012.
Contribution: Supervisor of the master thesis of Sabine Müller (background of this work), idea for using RTM for ultrasonic echo data, parts of the theory, design of synthetic models used, data interpretation.
4) *Section 5.3:* Sabine Müller and Ernst Niederleithinger: "Anwendung der Reverse Time Migration auf Ultraschall-Echo-Messungen in der zerstörungsfreien Prüfung im Bauwesen (Application of Reverse Time Migration on Ultrasonic Echo Measurements in Nondestructive Testing in Civil Engineering)". DGZfP-Jahrestagung 2014, Potsdam, Germany.
Contribution: Supervisor of Ph.D. work of Sabine Müller (ongoing), design of experiments, interpretation
5) ** Section 5.4:* Maria Grohmann, Ernst Niederleithinger, und Stefan Buske: "Geometry Determination of a Foundation Slab Using the Ultrasonic Echo Technique and Geophysical Migration Methods**".** Journal of Nondestructive Evaluation 35, Nr. 1 (March 2016). doi:10.1007/s10921-016-0334-z.
Contribution: Supervisor of the master thesis of Maria Grohmann (background of this work), concept for this study, parts of theory, data processing and interpretation.
6) ** Section 6.2.2:* Ernst Niederleithinger and Carolin Wunderlich: "Influence of small temperature variations on the ultrasonic velocity in concrete". In *Proceedings of QNDE 2012*, 390–97. Denver, 2012. doi:10.1063/1.4789074.
Contribution: Idea, design of experiment, part of the measurements, entire data processing and evaluation.
7) *Section 6.2.3:* Ernst Niederleithinger, Rolf Krompholz, Sabine Müller, Rainer Lautenschläger, and Jan Kittler: "36 Jahre Talsperre Eibenstock – 36 Jahre Überwachung des Betonzustands durch Ultraschall (36 years Eibenstock dam – 36 years monitoring the concrete condition by ultrasound) "**.** *38. Dresdner Wasserbaukolloquium 2015 "Messen und Überwachen im Wasserbau und am Gewässer"*. Dresden, 2015.
Contribution: Idea, design of experiment, part of the measurements, entire data processing and evaluation.
8) ** Section 6.3:* Simon Stähler, Ernst Niederleithinger and Christoph Sens-Schönfelder: "Monitoring stress changes in a concrete bridge with Coda Wave Interferometry". *Journal of the Acoustical Society of America*, 129(4), 1945–1952, doi:10.1121/1.3553226 (2011).
Contribution: Lab experiments, part of interpretation.

9) *Section 6.4:* Chinaemerem Kanu, Roel Snieder, Ernst Niederleithinger and Sven Grothe. "Time-lapse imaging of localized weak changes with multiply scattered waves: Laboratory experiment." Part of dissertation thesis, Colorado school of Mines, 2015.
Contribution: Idea and design for first experiment, partly for the second one. Parts of data evaluation and interpretation.

10) * *Section 6.5:* Johannes Douma, Johannes, Ernst Niederleithinger, und Roel Snieder: "Locating Events Using Time Reversal and Deconvolution: Experimental Application and Analysis". *Journal of Nondestructive Evaluation* 34, Nr. 1 (März 2015). doi:10.1007/s10921-015-0276-x.
Contribution: Concept of this study, idea design of experiments, parts of data evaluation and interpretation.

* Peer reviewed, Web of Science listed journal/conference papers

Preface

This thesis is the written part of my habilitation ("schriftliche Habilitationsleistung") as a part of my endeavors to acquire the "venia legendi" at RWTH Aachen University.

It is a compilation of research papers I have authored or co-authored in my post-doctoral time since 2010. The papers have been edited in format and content to make them fit to each other and to avoid too many repetitions. However, some repetitions are still there because I wanted the papers to remain recognizable. As far as possible, I have updated the references to account for newest research in the related field. A list of the papers compiled is given before this preface. I have added some sections to provide the necessary background and frame for this work.

My work and the work of others hasn't stopped after I decided which papers to use here. See sections 5.5 and 6.6 for further developments and section 7 for an outlook.

This is my own thesis, but I had help and most of the research was teamwork. See the acknowledgements (section 8) for details.

Potsdam, April 2017

Ernst Axel Niederleithinger

This version was edited after submission, before publication. While most of the changes are just correction of typos, formatting issues or updating of references (e. g. from submitted to published), one issue had come up during the review: Section 6.4.5 contains a simplification concerning the temperature development in the specimen under test, which is not properly discussed. While this does not affect the demonstration of the coda wave imaging presented there, one of the reviewers thought (and the author agreed) that a more detailed discussion and further calculations would be of benefit. During this work, additional doubts have come up about some sensor readings. Again, this does not affect the main purpose of research presented in this section on this thesis. However, it must be addressed. For this reason, an addendum/erratum was added to the thesis (chapter 11) and sent to the co-authors of this research for further proceedings.

Note, that no new references have been added after submission in 2017.

Potsdam, October 2019

Ernst Axel Niederleithinger

1 Summary

The application of ultrasonic testing in civil engineering started several decades ago, mainly limited to pulse velocity measurements in transmission mode for concrete quality control. Starting in the late 1990s, more and more emphasis was put on echo techniques for structural investigations of concrete constructions. Starting with the arrival of point contact transducers without the need of coupling agents these techniques have raised the capabilities of nondestructive testing (NDT) to a new level. Ultrasonic testing (UT) in civil engineering so far mainly benefitted from methods developed for traditional NDT of metals.

However, there are still gaps in the currently applied technologies due to their inherent limitations. These gaps might be at least partially closed by applying geophysical techniques, which have been developed for a totally different scale in terms of penetration depths and wavelengths but aiming at similar physical/mathematical challenges (e.g. complex geometries, multiple scattering). This thesis deals with two examples of geophysical methods, which have been adapted to concrete testing.

One of the major drawbacks of the imaging techniques currently applied in ultrasonic echo testing for concrete is the limitation to simple geometries. SAFT (synthetic aperture focusing technique), which is widely and successfully used in many variants in NDT, is closely related to geophysical Kirchhoff or Stolt migration. All these techniques aim to focus the reflected energy recorded at the surface back to the reflector, but only direct single reflections are correctly dealt with. Vertical reflectors or the backside of internal features in a construction can`t be imaged. In this thesis, Reverse Time Migration (RTM), another geophysical imaging technique based on the correlation of forward and backward propagating wavefields, is proposed as an alternative for imaging complex geometries. It is shown, that vertical boundaries as those at thickness changes of foundations slabs can be imaged correctly as well as the full geometry of inclusions (voids, tendon ducts). Examples are given based on simulated and measured data. RTM has some drawbacks, as the significant computation time required and artifacts mainly close to the surface, which require additional research and development before widespread practical application in NDT.

The second development documented in this thesis is the adaption of algorithms borrowed from seismology to detect subtle changes in concrete due to various loads or degradation in ultrasonic transmission measurements. Since about 10 years several research groups are working on the application of Coda Wave Interferometry (CWI) to evaluate very small changes in the elastic wave velocity (e. g. by stress) or changes in the scattering pattern (e.g. by cracks) inside concrete. Various lab investigations, but also a few first field experiments have shown, that this technology is in fact able to contribute to monitoring of concrete constructions, revealing changes in the material properties (here e. g. by stress or temperature) and to localize the affected area. New instrumental developments as robust and reliable ultrasonic transducers help to path the way for long term implementation in concrete infrastructure (e.g. bridges). Methods to separate different influence factors or to simplify imaging are currently under development.

2 Introduction

2.1 Geophysics in civil engineering: A short overview[1]

Geophysics and civil engineering (CE) are strongly connected. Even though a much larger budget is spent in hydrocarbon exploration and in the search for mineral resources, geophysical methods have been adapted to a much smaller scale and have been applied and accepted in civil engineering projects for many decades. Obviously, the focus has been on geotechnical projects for a long time. Seismic, resistivity, induction and potential methods are applied from the surface or in boreholes in the investigation of the often complex and changing near-surface part of the underground, as a base for large engineered structures such as dams, roads, railway tracks, airports, bridges or buildings. A recent overview of the state of the art in practice is given in the book of Reynolds (2011). The author has contributed to this field by the evaluation of geophysical methods for the investigation of river embankments (Niederleithinger et al., 2012). The investigation and quality assurance of foundations is closely related to this part of engineering. Geophysical and geophysics-like methods mostly deployed from boreholes and adapted to the needs of the tasks on hand are meanwhile applied on a regular basis. This field of work is one of the focal points of the author's research (e. g. Spruit et al.,2014; Niederleithinger & Ranz Garcia, 2014; Niederleithinger, 2012, Ertel et al., 2016), but will not be reported in this thesis.

Meanwhile geophysical tools are applied in structural investigations as well, covering all kinds of tasks between quality assurance of foundations to long-term bridge monitoring. One of the most prominent geophysical methods used to explore the interior of constructions is ground penetrating radar (GPR). The first applications of GPR go back by about 25 years, starting with the appearance of high frequency antennas used for pipeline detection and pavement investigation. Soon they were also used in reinforcement and tendon-duct localization, filling a gap, as they have a much larger penetration depth compared to traditional magnetic or inductive tools. The book compiled by Bendetto & Pajewski (2015) in the frame of the EU COST Action TO 1208 is a valuable source of information. Several manufacturers have offered dedicated antennas, data acquisition units and software. This has attracted the interest of some of the big players in the electronic industry who now try to grab their share of the market.

Various seismic, electromagnetic or other techniques have found regular applications here as well. One example is the "Wenner Probe", a simple fixed distance four electrode tool, which is used to measure the electrical resistivity of concrete in corrosion studies on a regular basis. Some geophysical methods are even part of standards and recommendations.

Other techniques have been developed in parallel. The geophysical míse-a-la-màsse method, which is used for near surface ore exploration is based on the very same physical principle as the potential method used for corrosion detection of reinforcing steel: Measurement of electrochemical potentials generated by oxidizing metal. Some other methods as impact-echo have been developed for NDT-CE only.

Recently several modern geophysical methods have been adapted to structural investigations in various fields. They help to improve the quality of imaging of the interior of structures and to detect small changes in concrete. For example, seismic migration techniques such as reverse time migration (RTM) has been successfully used in imaging the interior of concrete constructions using ultrasonic echo data. So far only near offset

[1] This section is edited from Niederleithinger et al., 2016.

measurements are performed on a regular basis. Imaging is mostly done with techniques closely related to Kirchhoff migration. Wide-offset data processed using RTM have been shown to be able to map more complex structures and to look behind obstacles. Other methods such as Coda Wave Interferometry developed in seismology play an important role in ultrasonic monitoring, an upcoming technique to detect subtle changes in concrete.

The other discipline which had an influence in testing methods for civil engineering (much stronger, so far) is nondestructive testing of steel and other metals, which is well-established and has been standardized since several decades. However, as geophysics has the experience to deal with inhomogeneous, porous, multiphase materials (a core drilled from concrete does not look much different from certain rocks, and it contains pieces of rocks anyway), there is a partial advantage for geophysical technologies. However, both fields are based on the same physical and mathematical principles, even though they use different words, tricks and shortcuts.

Synergy means transfer from and to both sides. Seismic developments might e.g. benefit from scale experiments using partially automatized, very effective ultrasonic test devices and sensors developed for civil engineering and properly designed concrete (or other) test models. This type of experiments can be used to assess certain capabilities and limitations of seismic methods. They are especially of interest in validation as they include the use of real (physically measured) data with all their issues and, other than field geophysics, a subject of investigation which is almost fully known. Scale experiments have been popular in geophysics until the 1980s when they became slowly less fashionable due to the increased use of numerical simulations. Chapter 6.5 shows an example involving a concrete cube with ultrasonic transducers to verify certain ideas about the improvement of time reversal techniques.

A couple of other developments, which are not covered in this thesis have been reported in a recent special issue of Nears Surface Geophysics (Niederleithinger et al, 2016).

2.2 Organization of the thesis

After this introduction, some background of the theory used in this thesis is given. The length is kept to a minimum, but a basis for the developments described in the following sections had to be made. The focus in on convolution and correlation, operations on time series playing an important role in the entire work.

Ultrasonic instrumentation is discussed in section 4. The author thought this to be necessary, as there are significant differences to the tools used on geophysics. And novel, robust transducers for embedment in concrete have opened new possibilities for research and practical application. Section 5 shows advances in ultrasonic imaging by adapting the recently developed Reverse Time Migration technique, now heavily used in oil exploration. It highlights that this enables us to see far more details in the interior of concrete structures. Developments in the application of ultrasonic monitoring of concrete are compiled in section 6. Methods borrowed from seismology as Coda Wave Interferometry show to have a yet unknown sensitivity to subtle changes in the material. Time Reversal methods might be the right tools to improve the detection and characterization of acoustic events in concrete.

The remaining section give conclusions, an outlook and a summary as well as acknowledgments to all who have contributed.

3 Short notes on theory

3.1 Convolution, cross-correlation and Fourier transform

Many sections of this work make use of two basic operations involving two signals (time series, waveforms, seismic traces etc.). In fact, both are integral transforms and closely related to each other.

Convolution is often seen as a modification of a function f(t) by another function g(t) and is defined as the integral of the product of both functions, after one has been reversed and shifted:

$$\begin{aligned} f * g = (f * g)(t) &= \int_{-\infty}^{\infty} f(\tau) g(t-\tau)\, d\tau \\ &= \int_{-\infty}^{\infty} f(t-\tau) g(\tau)\, d\tau \end{aligned} \tag{3-1}$$

The numerical equivalent (convolution for discrete time series) is:

$$\begin{aligned} f * g = (f * g)[n] &= \sum_{m=-\infty}^{\infty} f(m) g(n-m) \\ &= \sum_{m=-\infty}^{\infty} f(n-m) g(m) \end{aligned} \tag{3-2}$$

The practical calculation of convolution benefits from the use of the convolution theorem involving the Fourier transform $\mathcal{F}$:

$$\begin{aligned} \mathcal{F}\big(f(t)\big) = F(\omega) &= \int_{-\infty}^{\infty} f(t) e^{i\omega t}\, dt \\ f(t) &= \frac{1}{2\pi} \int_{-\infty}^{\infty} F(\omega) e^{-i\omega t}\, d\omega \end{aligned} \tag{3-3}$$

It holds that

$$\begin{aligned} H = \mathcal{F}(f * g) &= \mathcal{F}(f) \cdot \mathcal{F}(g) \\ &= F \cdot G \end{aligned} \tag{3-4}$$

An important example for convolution, which will be used later, can be found in signal theory. If an infinitesimal short impulse δ(t) is sent into a linear system S, it will answer with a specific response s(t) (impulse response). If a different impulse, say w(t), is sent into the very same system, the response will be s*w (see also section 3.2.2).

Cross-correlation is a measure of the similarity of two functions depending on the time shift of one of them:

$$f \star g = (f \star g)(\tau) = \int_{-\infty}^{\infty} f(t)^* g(t+\tau)\, dt \tag{3-5}$$

where * indicates the complex conjugate. For discrete functions, this leads to

$$f \star g = (f \star g)(n) = \sum_{m=-\infty}^{\infty} f(m)^* g(m+n) \tag{3-6}$$

If f and g are real (as most functions used in seismics and ultrasonics), the conjugate complex operator * is not required and often not given in the literature.

In many applications, e.g. in image processing by substracting the mean and dividing by the product of the standard deviations, the cross-correlation is normalized to give the value 1 for identical function and 0 for completely unrelated functions. Like convolution, cross-correlation can be calculated in the Fourier domain by:

$$\begin{aligned} \mathcal{F}(f \star g) &= \mathcal{F}(f)^* \cdot \mathcal{F}(g) \\ &= F^* \cdot G \end{aligned} \tag{3-7}$$

Convolution and cross-correlation are closely related. It holds, that

$$f \star g = f(-t)^* * g \tag{3-8}$$

If f is Hermitian ($f(t)^*=f(-t)$), it holds that

$$f \star g = f * g \tag{3-9}$$

Autocorrelation is the cross-correlation of a signal with itself, e.g. to identify repeated patterns in a signal:

$$(f \star f)(\tau) = \int_{-\infty}^{\infty} f(t)^* f(t+\tau)\, dt \tag{3-10}$$

3.2 Wave propagation

3.2.1 Acoustic and elastic waves

The research described in this work is based on the propagation of elastic waves in concrete. This includes complex phenomena, as a concrete body contains a large amount of scatterers with various size and properties (aggregates, cracks, pores), areas of different material properties (e.g. steel rebar, tendon ducts, areas of varying concrete quality) causing refraction and reflection and (other than the earth) free surfaces with edges and corners. The theory of wave propagation is described in various textbooks and manuscripts, e.g. in

Langenberg et al. (2009) for nondestructive testing and in Aki & Richards (2009) or Müller et al. (2007) for seismology.

As the details of the interior structure of a concrete construction are never fully known, most ultrasonic methods assume an at least piecewise homogeneous material. In homogeneous, isotropic, linear elastic media the analysis of stress and strain leads to the differential equations for planar waves in full space (here for cartesian coordinates x_i,x_j, x_k and propagation direction along the x_i-coordinate):

$$\frac{\partial^2 u_i}{\partial x_i^2} - \frac{1}{c_p^2}\frac{\partial^2 u_i}{\partial t^2} = q \qquad (3\text{-}11)$$

and

$$\frac{\partial^2 u_j}{\partial x_i^2} - \frac{1}{c_s^2}\frac{\partial^2 u_j}{\partial t^2} = q\ ; \qquad \frac{\partial^2 u_k}{\partial x_i^2} - \frac{1}{c_s^2}\frac{\partial^2 u_k}{\partial t^2} = q \qquad (3\text{-}12)$$

with u_i, u_j, u_k as the spatial components of the translation of a point in the medium and q describing the source in space and time. (3-11) describes the propagation of longitudinal waves (p-waves, translation in the direction of propagation), (3-12) of shear waves (s-waves, translation perpendicular to the direction of propagation). c_p and c_s are the respective velocities:

$$c_p = \sqrt{\frac{E(1-\nu)}{\rho(1+\nu)(1-2\nu)}}\ ; \qquad c_s = \sqrt{\frac{G}{\rho}} \qquad (3\text{-}13)$$

with E being the Young's modulus, G shear modulus, ρ density and ν the Poisson's ratio of linear elasticity. Typical velocities for concrete are from 3500 $m \cdot s^{-1}$ to 5000 $m \cdot s^{-1}$ for p-waves and from 2200 $m \cdot s^{-1}$ to 2800 $m \cdot s^{-1}$ for s-waves. Densities are between 2100 $kg \cdot m^{-3}$ and 2500 $kg \cdot m^{-3}$.

In addition, at a free surface or at specific structures other wave types might develop (Rayleigh, Love or Scholte waves). All wave types may convert into each other due to reflection, refraction and scattering at boundaries. As wave type conversion and the occurrence of different wave types in a single set of measurements is difficult to handle it has become popular in ultrasonic echo testing for civil engineering to use arrays of shear wave transducers polarized perpendicular to the line of measurements (say: in x_j direction) and to position the lines of measurements in a way, that the subsurface can be assumed to be at least approximately two-dimensional (changes only in direction of x_i (line of measurement) and x_k (depth)). This way, wave conversion is averted and only s_h-waves (s-wave polarized horizontally) are to be dealt with. This leaves the first part of (3-12) as the only relevant wave equation.

Naturally, for materials with G = 0 (fluids, gases) no shear waves exist. Only p-waves can propagate, and wave conversion does not occur. The acoustic wave equation can be written as:

$$\frac{\partial^2 p}{\partial x_i^2} - \frac{1}{c_p^2}\frac{\partial^2 p}{\partial t^2} = q \qquad (3\text{-}14)$$

with p being the pressure.

As this equation is easy to handle and a vast amount of very effective numerical tools to solve it even in large inhomogeneous volumes exist, the acoustic wave equation is used in many simulation and imaging applications for p- or s-waves in elastic media. For the case of s_h-waves polarized perpendicular to the line of measurements in two-dimensional media this leads kinematically to correct results, if the shear wave velocity is used instead of the p-wave velocity. However, the amplitudes e.g. for reflections are not treated correctly as the boundary conditions at interfaces are different for p-waves and s_h-waves (see e.g. Müller et al., 2007, p. 66 ff.).

In many cases, it is effective to express the wave equation in the Fourier domain. This leads to equations of the Helmholtz type. For the acoustic wave equation, this is:

$$\frac{\partial^2 P}{\partial x_i^2} + k^2 P = Q, \quad k = \frac{\omega}{c_p} \tag{3-15}$$

With P =P(ω) and Q = Q(ω) being the pressure and the source term in the Fourier domain. The Helmholtz equations are simpler to handle for certain theoretical treatises. They are easier to solve numerically as they involve just three instead of four dimensions. As a tradeoff, the results must be transformed back by the inverse Fourier transform. However, they are preferred e. g. in simulations of narrow banded applications in ocean acoustics.

3.2.2 Greens functions

In the analysis of seismic wave propagation Green's functions are very frequently used. In general mathematics, they are defined as the impulse response of an inhomogeneous differential equation for specific initial and boundary conditions in a specified domain. For (3-14) this leads to:

$$\frac{\partial^2 g}{\partial x_i^2} - \frac{1}{c_p^2}\frac{\partial^2 g}{\partial t^2} = \delta(t - t_0) \tag{3-16}$$

with g(t) being the Green's function and $\delta(t\text{-}t_0)$ the Dirac delta function as an infinitesimal short impulse source (point force in a specific direction) at a specific time and place. The Green's function changes, if the source changes in space and time or if any boundary or initial condition changes. To be accurate it must be stated that the Green's function is in fact a 3 by 3 tensor as the point force may act in any of the three spatial directions.

The wave equation can be considered as a linear operator. Thus, if u_a is the response to a source q_a and u_b to q_b, the response a combined source $q_{ab} = q_a+q_b$ would be $u_{ab} = u_a+u_b$. As any source term can be represented by a set of properly scaled and delayed delta functions, the response can be derived from the Green's function by:

$$\begin{aligned} u(t) &= g(t) * q(t) \\ U(\omega) &= G(\omega) \cdot Q(\omega) \end{aligned} \tag{3-17}$$

This relation can be applied many ways. Most popular is to use deconvolution to sharpen the measured seismic response u(t) of a system if the source function q(t) or its spectrum are known. However, there are many numerical caveats as shown e.g. in section 6.5.

3.2.3 Reflection, refraction, diffraction and scattering

If an acoustic or elastic wave meets a change in material properties, it is influenced in terms of direction, speed, amplitude and phase. All related phenomena may be summarized under the term scattering. In practice, it is often distinguished between the influence of material changes on a scale significantly larger than the signal wavelength (reflection, refraction of waves) and those of material changes of comparable or even smaller size than the signal wavelength (diffraction, scattering). The general theory of elastic wave scattering is given e.g. by Snieder (2002).

The first case (scale of inhomogeneity large compared to wavelength) appears in structural investigations of concrete objects e. g. at the reflection at a free surface of an object (thickness measurements), large voids, large diameter tendon ducts or layers of different material. For the simplest case (plane waves and planar boundaries) the theory is well known and described e.g. by Aki & Richards (2009) or Müller et al. (2007). In case of spherical waves this theory is still useful as a decomposition into planar waves can be made. If the size of the object is comparable to the wavelength and the material property contrast is sufficient (e.g. steel rebar, small tendon duct, void of sufficient size, edge in a boundary) the waves are diffracted (scattered) in a specific pattern. If the respective signals have sufficient amplitude in seismic or ultrasonic experiments, imaging or migration algorithms can be used to trace them back to their origin and provide information about the interior geometry of an object (chapter 5).

Concrete contains inherently a large amount of scatterers, which have a similar size as the wavelength or smaller (aggregates, cracks, pores). Each of them produces an individual scattered wavefield, which is again scattered at other inhomogeneities, generating a diffuse background in any ultrasonic experiment. The amplitudes of these diffuse waves are hard to predict as concrete properties (e.g. type and shape of aggregates) vary a lot. Signals from distinct reflectors may be masked. However, the diffuse wave field can be used to detect subtle changes in the medium by repeated experiments (chapter 6).

If the inhomogeneities are much smaller than the wavelength (e.g. fine aggregates, small pores, microcracks) they are still influencing the wave propagation, but can't be seen directly in seismic or ultrasonic experiments. Wave speed and amplitudes are affected in a way which is described by effective medium theory. Various models exist, starting with the well-known Gassmann formulas (Schön, 2004).

3.2.4 Simulation

Real structures (or the earth) are far too complicated for analytical solutions of the wave equations provided above. Numerical simulations are required to investigate wave propagation. In the past decades, a vast number of tools has been developed. All of them subdivide the medium in small elements in which the material properties are constant. As these elements have a finite size, spatial resolution is limited. The boundaries of the model must be treated according to their nature (free surface, reflecting or adsorbing planes). The time is divided in small finite steps as well. Certain criteria must be met for the size of elements, time steps and signal wavelength to ensure accuracy and stability.

In geophysics, most simulation programs are based on finite difference techniques. Two different seismic finite difference codes have been used in this work. The first one, a parallel 2D code originally developed by Bohlen (2002) is applied in sections 5.2 and 5.3. In section 5.4, a 2D code from the public domain software package Madagascar (Fomel et al., 2013) is used.

4 Ultrasonic instrumentation for civil engineering

4.1 General remarks

About 25 years ago, it was said that ultrasonic testing would never make it to on-site investigations. This claim was due to a lack of easy to use, affordable transducers as well as measuring devices including sufficient computing power and visualization capabilities. Fortunately, this has not come true. A whole new generation of transducers has been developed, without whom most of the material shown in this work would not have been possible. The continuous development of digital computing has given us the resources to use sophisticated algorithms for data evaluation, e.g. the reverse time migration method or interferometric techniques, which are used here. In addition, automated scanning devices have been developed at Bundesanstalt für Materialforschung und -prüfung (BAM), which can collect data with an unprecedented accuracy and speed. This section gives an overview on these developments with emphasis on the recently developed sensors to be embedded in concrete, a work, in which the author was heavily involved.

4.2 Surface mounted transducers

Concrete is an extremely inhomogeneous material on different scales. Most prominent are the aggregates contained with a size typically varying between less than a millimeter and a few centimeters. To avoid scattering, the ultrasonic wavelength should be significantly larger than this. However, many structures of interest are in the centimeter range and a larger wavelength would lead to a reduced resolution (or even invisibility) of these features. Compromises must be made. Typical frequencies used in ultrasonic concrete investigations are between 50 kHz and 400 kHz for p-waves and 25 kHz and 100 kHz for shear waves, all of them much lower than for traditional ultrasonic testing. Assuming typical velocities of 4000 $m \cdot s^{-1}$ for p-waves and 2600 $m \cdot s^{-1}$ for shear waves, this leads to wavelengths between 1 and 10 cm. A detailed investigation on ultrasonic transducers for civil engineering, including air coupled ones, is given by Maack (2012).

The transducers used for ultrasonic investigations are, besides few exceptions, piezoelectric and can be used both for transmitting and receiving. Various types exist, from large, flat phased array to horn types (see e.g. Figure 4-1). In parts of this thesis, a relatively new type of transducers was used, developed about 15 years ago at ACS Ltd. (Moscow Russia). These so-called point contact transducers exist and are available in several variants for vertical and horizontal component signal generation and detection (Figure 4-2). The sensors are small and don't require a coupling agent. For many applications, they are coupled to linear or planar arrays, where each transducer is spring loaded to ensure coupling even on rough surfaces. The point contact transducers are normally coupled to linear or planar arrays to increase the signal-to-noise-ratio and to improve the directional characteristics (example in Figure 4-3).

Figure 4-1: Conventional ultrasonic transducers for concrete investigations (Low-frequency transducer S0208, longitudinal, 100 kHz, ACS Ltd.)

Figure 4-2: Point contact ultrasonic transducers as used in most state of the art devices for concrete (Low-frequency transducer S1802, shear waves, 50 kHz, ACS Ltd.)

Figure 4-3: Ultrasonic array with 24 transducers of the type shown in Figure 4-2. The upper four by three are directly coupled and work a transmitter array, the lower four by three as a receiver array. (ACS Ltd.)

4.3 Automatized surface measurements

For detailed investigation of concrete constructions using up-to-date imaging methods, a large amount of measurements and a sufficient positioning accuracy are required. Manual sensor placement is tedious and incorporates the danger of sensor mispositioning or unintended gaps in the data. For this reason, the development of automated scanning systems for methods as, e.g., radar, impact-echo or ultrasound has started at BAM more than 20 years ago (see e.g. Streicher et al., 2006; Krause et al., 2008). Most models consist of two perpendicular rails, which are used to move a sensor head with sub-centimeter accuracy (Figure 4-4). Pneumatic cylinders are used to press a sensor onto the surface (or to lift it up) if required. Vacuum pods (red "feet" in Figure 4-4 left) keep the device in place at vertical surfaces or overhead. Scanning areas are between 1 m^2 and 40 m^2. A special version has been developed for the investigations discussed in chapter 5. Meanwhile BAM has developed scanning systems which can climb a wall or move autonomously (Stoppel et al., 2011; Schubert et al., 2015).

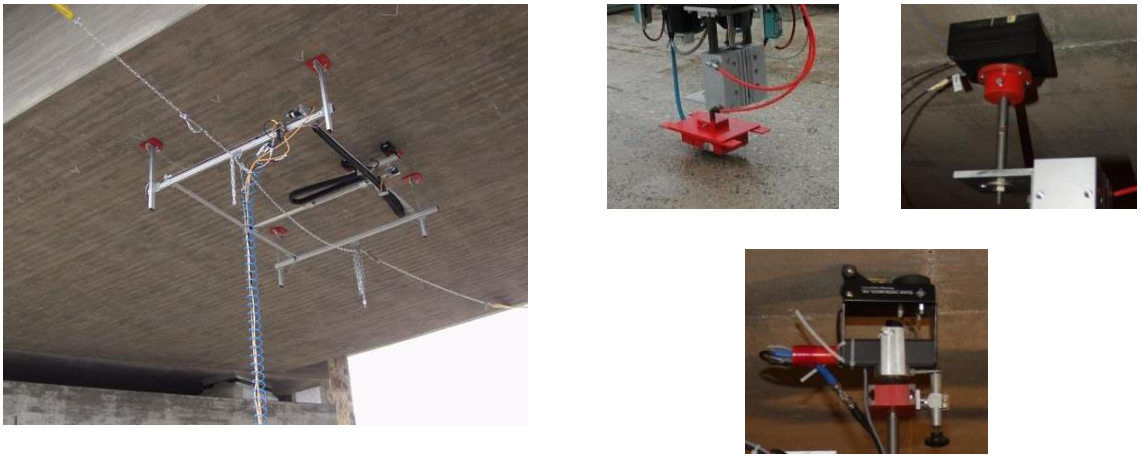

Figure 4-4: Left: BAM NDT scanning system mounted below a concrete bridge. Right: The scanners can be used with various radar, ultrasonic impact-echo or other sensors. Pictures: BAM.

4.4 Embedded sensors[2]

4.4.1 Introduction

Concrete is a complex, multi-phase material. It is made of hydraulic cement, water and aggregates in many variations. The first two ingredients start to hydrate and crystallize when in contact with each other. This process is fast in the first hours and days but can continue for months or years. The aggregates, gravel or crushed stone of various types and sizes (µm-cm range), are used as a filler to save cost and energy. Concrete contains pores, either filled with unbound water or air.

Concrete is mankind's most produced material. It is strong, resistive and durable. Some early concrete structures as the cupola of the Roman Pantheon have been standing tall for almost 2000 years. However, under certain conditions (hostile environments, adverse load conditions) concrete constructions require attention. For example, the apparently ever-increasing traffic load (number and individual load of trucks) on bridges may lead to deterioration much earlier than expected at the time of design. Currently, inspections are still based on visual methods mainly, but sophisticated nondestructive methods are used more and more often. The use of bridge instrumentation increases rapidly (Karbhari et al., 2009). But so far monitoring is limited to local sensors (e. g. strain gauges), which are probing just their close vicinity, or global methods as modal analysis. There is a gap in between. A method which would look at a certain critical volume of concrete with a very limited number of sensors would be of great value.

Ultrasonic transducers with frequencies from 25 kHz to 400 kHz have been used for concrete for decades. They are used in the laboratory on samples (and sometimes on site) in transmission mode to measure elastic properties and to assess degradation. New point contact transducers have revolutionized the use of echo techniques for thickness measurements and structural imaging. Even the detection of voids in tendon ducts is claimed to be possible (Krause et al., 2011). All transducers used in practice so far are for surface mounting. For monitoring this approach shows three strong disadvantages. First, the need for constant coupling, which is hard to realize on the surface in practice. Second, the high influence of surface and external effects (temperature and others) leads to

[2] This section is edited from Niederleithinger et al. (2015a).

unwanted effects on the measurements. Third, in practical field applications the transducers are prone for accidents or vandalism. Therefore, we started to develop a novel transducer, which can be permanently embedded in concrete.

This is not the first or only attempt to embed ultrasonic transducers in concrete. Similar ideas have been proposed e. g. by Song et al. (2008), Kee & Zhu (2013) or Zhao et al. (2016), but demonstrated only in experimental setups for lab applications. They are often marketed as "smart aggregates". For practical applications, a robust approach would be required. An experiment conducted more than 35 years ago, monitoring the hardening of concrete at a massive water dam in Saxony, Germany, by embedded ultrasonic transmitters and receivers, recently gave us the opportunity to prove that this kind of sensors might survive in concrete for decades (Niederleithinger et al., 2015a) (see section 6.2.3).

4.4.2 A novel ultrasonic transducer to be embedded in concrete

4.4.2.1 Transducer design and description

New ultrasonic transducers ("SO807") have been designed by ACS Ltd., Moscow, Russia in cooperation with and exclusively for BAM (Figure 4-5). The main part is a hollow piezoceramic cylinder of 20 mm diameter and 35 mm length. The electric connections are on the inside. On both ends metallic pieces are clamped to the piezoceramic part. The outer diameter of 15 mm allows stacking of several transducers along a line using standard PVC tubes. Having all cables inside ensures good coupling of the piezo to the concrete and protects the electrical connections during installation. Total length of the transducer is 75 mm.

Figure 4-5: Photograph of the novel ultrasonic transducer for embedment in concrete (Manufacturer: ACS Ltd., Moscow, Russia. Photo: BAM).

4.4.2.2 Installation

The transducers can be installed easily at the time of construction. To ensure that they keep their position during casting and vibration, they should be mounted either directly to the reinforcement or using a kind of stabilizing construction. In bridge installation done lately (section 6.2.4), L-shaped pieces of rebar welded to the reinforcement have been used to hold the transducers at the specified position (Figure 4-6). Another possibility would be to mount stacked series of transducers using PVC tube segments (like the method used for installation in existing structures described below).

Figure 4-6: Photograph of an ultrasonic transducer mounted at a bridge construction site before casting (Photo: neostrain S. A.).

For existing structures, a method has been developed to install one or several transducers at the required depth(s) in a drill hole and ensuring coupling to the concrete. The hole is drilled with a slightly larger diameter than the transducers and slightly deeper than the installation depth. The transducer(s) and the tube segments are connected to a sealing cap at the surface (Figure 4-7). The cap contains an inlet, which is connected to a grout reservoir and to the space between the transducers/tubes and the concrete. By connecting a suction pump via an outlet in the cap to the inner hollow space of the transducers and the tubes the grout is sucked into the drill hole and via the top of the tubes into the inner space (Figure 4-7(c)). When the grout appears at the outlet one can be sure (at least almost) that the entire space is filled, and the transducers are coupled to the concrete. A fast hardening, slightly expanding type of grout is used for this purpose.

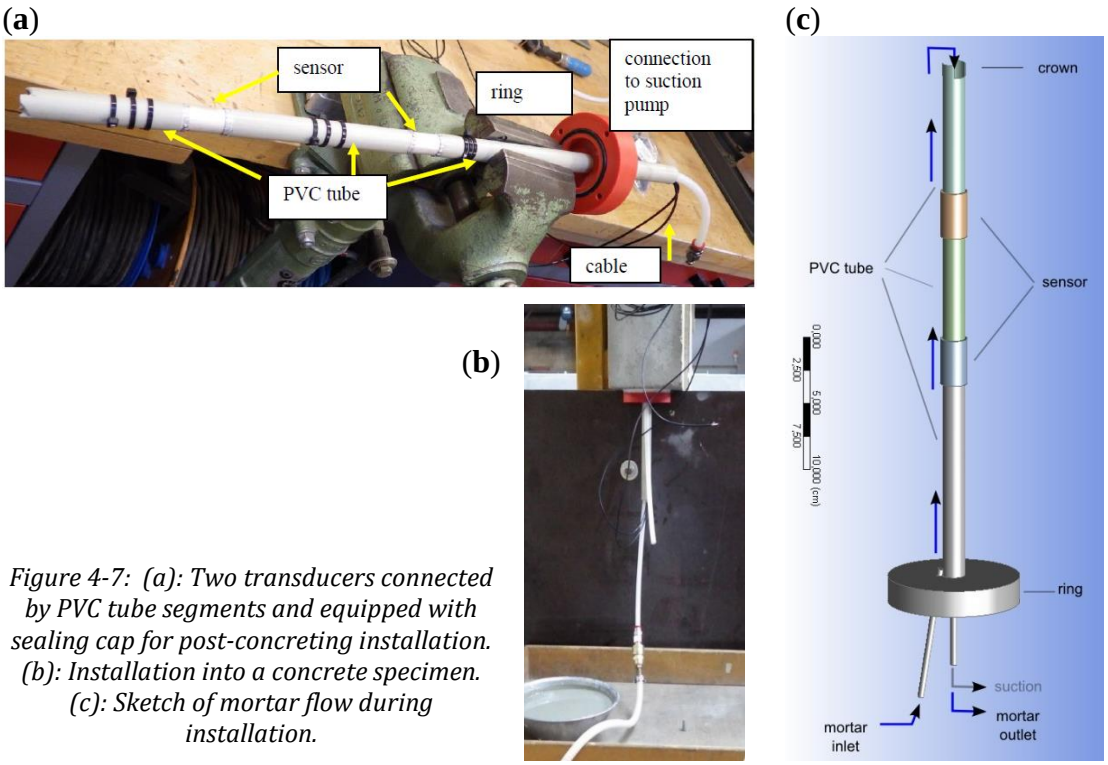

Figure 4-7: (a): Two transducers connected by PVC tube segments and equipped with sealing cap for post-concreting installation. (b): Installation into a concrete specimen. (c): Sketch of mortar flow during installation.

4.4.2.3 Characterization

The transducers have been characterized by some basic experiments. First, two transducers of the same type have been installed back to back directly without any medium in between to evaluate the frequency spectrum. A short impulse (t = 2 µs) was used as input. The signal recorded by the transducer is displayed in Figure 4-8. The signal recorded shows a wavelet with about 20 periods and a total duration of ca. 0.3 ms. The reverberations show a lack of damping of the piezo material. As we don't intend to use the transducers for imaging applications, where a sharp response (broadband in frequency domain) would be more beneficial, this behavior is fully satisfactory.

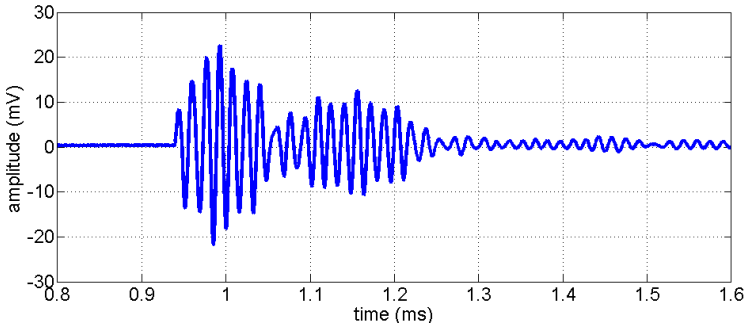

Figure 4-8. Response of the novel transducer to a short electrical impulse (2 µs), recorded by a second, identical one with no distance in between them. Time of onset due to recording hardware settings.

The amplitude spectrum of the data of Figure 4-8 is shown in Figure 4-9. There is a prominent frequency peak at 62 kHz and a significant second one at 65 kHz. Smaller peaks appear around 50 and 85 kHz. There is no significant energy with frequencies lower than 40 or higher than 90 kHz. A frequency of 62 kHz relates to a wavelength in concrete (compressional wave speed of about 4000 $m \cdot s^{-1}$) of ca. 65 mm. This is at least twice the size of most aggregates (max aggregate size 32 mm in many types of concrete).

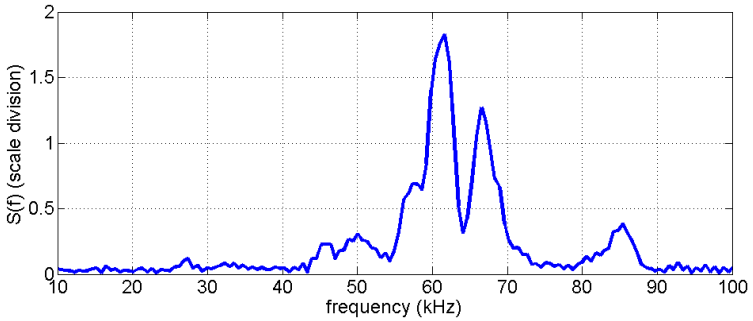

Figure 4-9. Amplitude spectrum of data shown in Figure 4-8.

To evaluate the directivity pattern of the new transducer, two experiments have been conducted, the first in a water pool, the second using transducers embedded horizontally or vertically in two separate cylindrical concrete blocks, respectively (Figure 4-10). In the first case, an identical transducer (oriented vertically) was used as receiver in the water pool. In the second experiment, a laser vibrometer was used to record the surface vibrations of the concrete. The laser vibrometer's position was fixed while the block was rotated in 10° intervals before each excitation. In both cases the measurements were taken using a) vertical and b) horizontal orientation of the transmitting transducers.

Figure 4-10. Experimental setup for measurement of directivity patterns. Transmitting transducers are embedded in the center of the concrete block. Surface movements are recorded by a laser vibrometer (in front).

The results of the directivity measurements are shown in Figure 4-11. To produce these plots, the amplitude of the direct arrivals (maximum of the first cycle) have been taken in 10° steps and normalized to the maximum value of all of them. For a vertical transmitter (left in Figure 4-11) an almost perfect circular pattern was recorded in water. This had to be expected as the transmitter is rotational symmetric round its vertical axis. In concrete, the circular radiation pattern is still recognizable, but far from being perfect, probably due to the inherent inhomogeneities in concrete.

For horizontal transmitter orientation (right in Figure 4-11) the directivity pattern in water resembles something close to a number eight. Apparently (and not unexpected as applying a voltage to the cylindrical piezoceramic leads mainly to changes in diameter, not in length) the amplitudes emitted in the direction of the transducer's rotational axis are much smaller than in the perpendicular direction. The experiment with the same configuration in concrete showed that the amplitude is similar in all directions (but has significant variation). The interpretation is that due to scattering at the concrete's aggregates, pores and cracks, the directivity pattern is somewhat obscured.

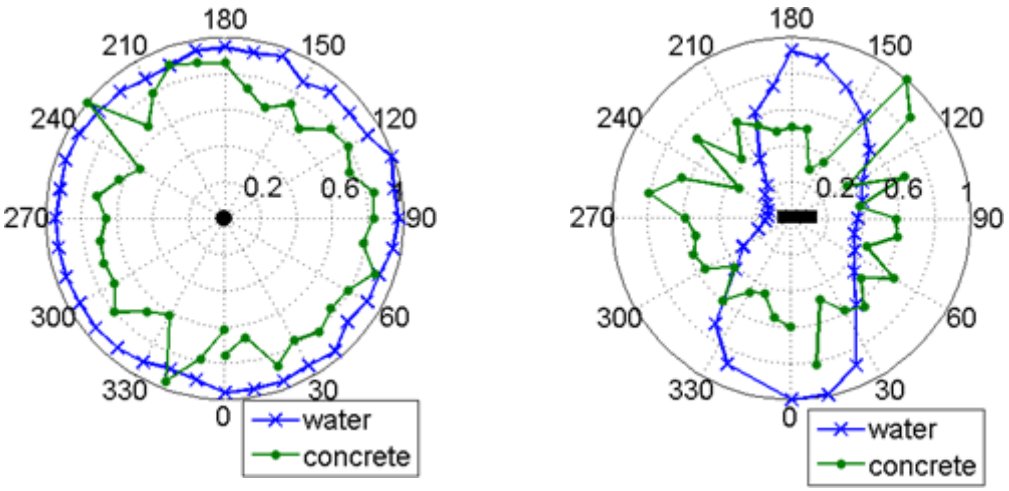

Figure 4-11. Directivity patterns for the new transducer, measured in water (blue crosses) and concrete bodies (green dots). Left: vertical orientation. Right: horizontal orientation. Axis from center to perimeter: relative amplitude. Seen from above.

Additional experiments have been performed to get an idea on the range of our new transducers. This was done to assess the maximum possible distance between transmitters

and receivers in future sensor networks in massive concrete structures. For this purpose, a set of transducers was installed in two concrete blocks partly with, partly without reinforcement. Some transducers were installed before casting, some afterwards (see section 4.4.2.2). One block had a maximum aggregate size of 16 mm, the other 32 mm. For all scenarios (aggregate size, reinforcement, and installation type) the same measurement setup was used. One of the transducers, excited with a 100 V square pulse, was used as transmitter. At two others (distance r = 0.25 and 0.75 m, respectively, from the transmitter) the amplitudes A (maximum of first cycle) of the first arrivals were recorded. The amplitude ratios are shown in Figure 4-12. It shows, that the attenuation is mainly dependent on the installation type, but not on aggregate size or reinforcement (the latter not shown here). The applicable range of our transducers was estimated from these data to be around three meters [6, 7]. For this we calculated the material and frequency specific damping constant α from the amplitudes (A_1, A_2) of the first arrival after r_1 = 0.25 m and r_2 = 0.75 m using

$$-\alpha = \left[ln\left(\frac{A_2}{A_1}\cdot\frac{r_2}{r_1}\right)\right]\frac{1}{(r_2 - r_1)} \qquad (4\text{-}1)$$

For an estimate for the maximum applicable range r_E, r_2, A_2 have been replaced in this equation by r_E, A_E and resolved for r_E. Under the assumption for the amplitude A_E at r_E to be at least twice the noise level, which might be different for every measurement environment, we have calculated values between 3 m and 5.5 m for our experimental setups [6, 7]. The amplitudes for transducers installed after concreting are larger, probably because the special expanding grout used guarantees perfect coupling.

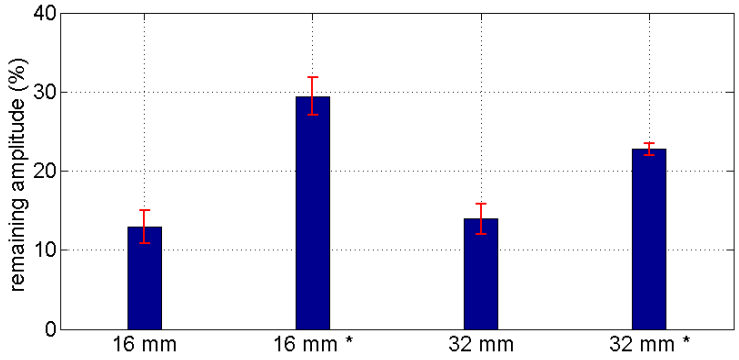

*Figure 4-12. Amplitude ratios between near and far receivers in the attenuation experiment for the two specimens (16 mm and 32 mm max. aggregate size). The * marks values for transducers installed after concreting.*

4.4.3 Short notes on ultrasonic transmission experiments

4.4.3.1 Wave propagation in concrete

Piezo transducers are inducing elastic waves into a concrete body. The propagation of these wavefields depends on the transducer, signal type and frequency as well as the body's material, and geometry. The theoretical background for a homogeneous linear elastic material is given in section 3.2

Concrete is neither homogeneous nor fully linearly elastic. In addition, ultrasonic waves are subject to reflections at internal boundaries or scattering at small (similar or smaller than the wavelength used) objects as aggregates, small cracks or reinforcement rebars. At the same time, the amplitudes of the ultrasonic waves are affected by geometric and intrinsic (material related) attenuation. From literature, it is known that the following factors (and potentially also others) have an influence on ultrasonic velocities and the amplitudes:

- Concrete type and compressive strength (Jones & Facaoaru, 1969; Crawford, 1997; BS EN 12504-4)
- Stress (Sayers, 1988; Shokouhi et al., 2012; Suaris & Fernando, 1987; Wu & Lin, 1998; Zhang et al., 2012)
- Temperature (Wolf et al., 2014; Crawford, 1997; BS EN 12504-4;0 Niederleithinger & Wunderlich, 2012; Zhang et al., 2013)
- Moisture (Ohdaira & Masuzawa, 2000; Hedenblad, 1993; Lencis et al., 2013)
- Degradation and microcracking (Suaris & Fernando, 1987; Pavan et al., 2013; Ramamoorthy et al., 2004; Pavan et al., 2009)

Traditional time of flight measurements are considering direct waves only (first arrival at the receiver in most cases). The area of influence is limited to a narrow band ("first Fresnel zone") between transmitter and receiver (Figure 4-13 left). Many other waves arriving much later at the receiver have undergone reflections and scattering, potentially even wave type conversion. It is quite often difficult to evaluate these arrivals separately. However, they contain useful information as they are covering larger areas of the concrete body (Figure 4-13 right) and are more sensible to velocity changes due to the longer travel paths.

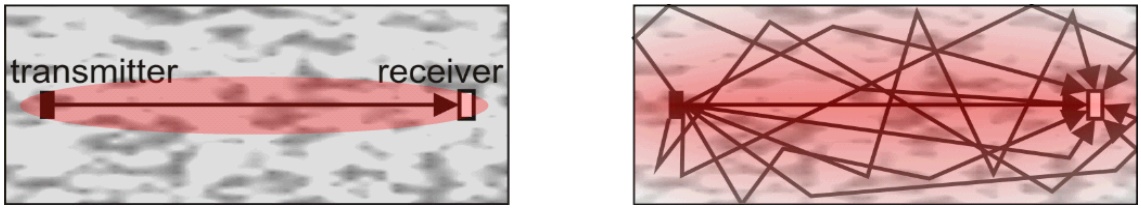

Figure 4-13: Sketch of ray paths (black lines) and area of influence (red) for the direct wave (left) and the full signal including coda (right).

4.4.3.2 Data evaluation

The traditional way to interpret transmission data ("time of flight") is described in the corresponding standards on ultrasonic pulse velocity measurements (see e. g. BS EN 12504-4; ASTM C597-09). Picking of the first arrival travel times is often done manually. Many different automatic picking algorithms have been proposed from simple threshold pickers to more sophisticated ones based on statistical criteria. Based on our experience we prefer the AIC (Aikake information criterion) picker as described by Tronicke (2007). This picker has been used successfully in many of our applications (e. g. Niederleithinger et al., 2015a). The main disadvantage of the time of flight method is that changes in the medium under investigation may result in very small changes of the arrival times which are hard to detect. In addition, we would need a dense network of transducers in a construction to cover the entire volume by the relatively narrow Fresnel zones.

Recently methods have been introduced to ultrasound investigations in concrete, using the entire signal and not just the first arrival. Online monitoring systems can benefit from the use of correlation calculations (of a time series measured during/after load/damage against a reference one). Some more details and preliminary results have been published in Niederleithinger et al. (2014). For quantitative evaluation, a novel method called Coda Wave Interferometry may be used, which can calculate velocity changes from ultrasonic data with high sensitivity. This method is discussed in detail in section 6.

4.4.4 Application examples

4.4.4.1 Monitoring of load changes

A 1.5 x 1.5 x 1.5 m^3 concrete block ("GK32") was cast in the BAM labs for various tests of the embedded ultrasonic transducers (Figure 4-14). The lower half contains a certain amount of reinforcement, the upper one is not reinforced. 18 ultrasonic transducers were been embedded, partly during partly after casting the block. Just ten of those were used for a load monitoring experiment due to limitation of the available data acquisition equipment. The experiment is described in more detail by Niederleithinger et al. (2014). A two-channel multiplexer connected the transducers to an ultrasonic transmitter (rectangle pulse, 50 kHz) or a data recording system. All 90 transducer combinations could be interrogated within seconds or minutes, depending on the number of repetitions. In the upper half of the concrete block a hole was drilled to insert a thread bolt. Some of the transducers were just a few cm away from the center of the load, some almost 1 m. Nuts, 10 cm x 10 cm load distributing plates and a piezo load cell provided a way to introduce localized compressional stress in a controlled, repeatable way. The direction of the main compressional load is perpendicular to the front surface shown in Figure 4-14. However, stresses parallel to the front face are generated as well. Load steps of 5 kN or 10 kN were applied in various cycles up to a maximum load between 20 kN and 100 kN, more than one order of magnitude below the compressive strength of the concrete.

Figure 4-14. Concrete specimen GK32 with embedded transducers and load application system. From Niederleithinger et al. (2014).

The applied loads, even very small ones, had a clear influence on the ultrasonic signals. A simple but valuable tool to provide a measure for the change is calculating the correlation coefficient between a reference measurement (here: zero load) and all consecutive measurements under various load conditions. Figure 4-15 shows the development of the correlation coefficient for transmission data between two embedded transducers close to the loading point. Both transducers have the same embedment depth (seen from the front face). Thus, direct waves are traveling perpendicular to the main load direction, but later parts of the signals (reflections, scattering) contain also information from different propagation directions. Even small load changes of 5 kN can clearly be seen, even in the presence of noise. Tomographic coda wave evaluation of the entire embedded transducer data set showed that the area of significant influence of the load is limited to about 0.3 m away from the loading point (Niederleithinger et al., 2014).

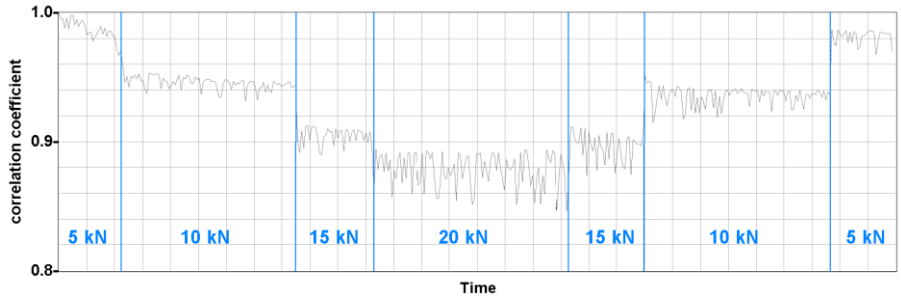

Figure 4-15. Correlation coefficient of 5 ms time series (reference: measurement at zero load) of ultrasonic signals measured by embedded transducers in a concrete block under small local compressional load. Line represents very dense consecutive measurements. From Niederleithinger et al. (2014).

4.4.4.2 Acoustic emission

The acoustic emission (AE) technique monitors acoustic waves produced by newly developing micro cracks, opening and closure of existing cracks, friction, etc., all of which are caused by internal stress variations (Suaris & Fernando, 1987; Große & Schumacher, 2013). Based on techniques used in seismology, the source of the acoustic emission can be localized. Traditionally the sensors used to detect AE events are arranged on the surface of the monitored element. The distance between them is restricted by the attenuation of the waves within the material. The frequency spectrum of the acoustic events in concrete is below 200 kHz (Wu & Lin, 1998). If a set of embedded transducers could perform both passive (AE, localization of active cracks) and active measurements (determination of changes of velocity/attenuation/material parameters) simultaneously, this would be a great step forward for structural health monitoring of concrete structures.

Laboratory tests on the use of the embedded transducers for AE were conducted using a similar specimen as discussed in section 4.1 ("GK16"). All twelve embedded transducers were used with an AMSY6 recording system (Vallen Systeme GmbH) to detect acoustic emission events within the specimen and on its surface. All following measurements were repeated three times. In a first step, the embedded transducers were used one at a time as artificial acoustic emission sources by sending a voltage pulse to each transducer successively. The average velocity of the compressional waves, measured during this automatic sensor test, was around 4500 $m \cdot s^{-1}$. Figure 4-16 shows the corresponding event localizations (green dots) calculated by the location processor option "Planar, plane" of the software Vallen VisualAE. They are coincident with the transducer locations.

In a second set of experiments pencil breaks on the specimen's surface were performed, a commonly used test for AE systems (ASTM E976). Again, the experiments were repeated three times at points marked by circles in Figure 4-16 and the events were recorded and evaluated using the AMSY6 system. The localization (red dots in Figure 4-16) in areas with good transducer coverage lies on the mark within ±3 cm. Those events outside the transducer array were not located accurately.

The experiment shows that the joint use of the embedded transducers in active and passive measurements is possible. The source needs to be within the sensor network for an accurate localization. Future research will focus on the appropriate distance between the receivers for detecting and localizing acoustic emissions of different frequency and energy.

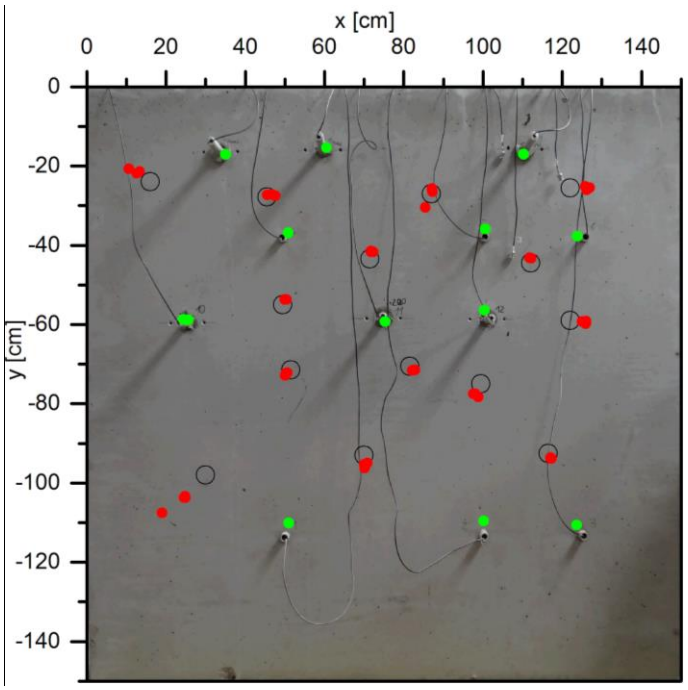

Figure 4-16. Location of acoustic emissions monitored with embedded ultrasonic transducers. Green marks: events localized by AE within the specimen (sources: one of the embedded transducers). Red marks: event localized by AE on the specimen's surface (source: pencil breaks in black circles).

4.4.4.3 Time reversal experiment

The novel transducers have also been used for a time reversal experiment. This application example illustrates the use of the embedded transducers for model experiments in geophysical research. In geophysics, the validation of new approaches for measurement techniques or data evaluation is often limited to simulations as the real subsurface (especially in exploration when talking about several kilometers depth) can never fully be explored. Therefore, full scale experiments often lack ground truth. Scaled model experiments might be helpful.

The experiment is described in section 6.5.

4.4.4.4 Other applications

The embedded transducers have been applied in two other fields of applications so far. In several experiments they were used to instrument concrete lab samples (typical size 15 x 15 x 40 cm[3]). These samples have been put into climate chambers or CDF[3] test devices to evaluate the influence of temperature (Niederleithinger & Wunderlich, 2012) and moisture on ultrasonic data. This evaluation is required in real world monitoring application as the influence of loads or deterioration is often covered by environmental influences. Instrumented lab samples may also be used in CDF test for freeze thaw resistance evaluations. The measurement of ultrasonic pulse velocity is already part of these evaluations, but the samples must be removed from the CDF test chambers so far. Embedded transducers would make these tests much easier.

We have started to use the embedded transducers in full scale monitoring applications as well. An existing, degraded bridge in Turkey has been monitored for more than two years by a set of eight transducers. A new bridge in Poland has been equipped with eight

[3] CDF: Capillary suction of de-icing agent and freeze-thaw-test, a recognized test method the check the freeze-thaw resistance of concrete.

transducers before concreting. The hardening of the concrete could be monitored during the first 28 days. A load experiment has followed and is described in section 6.2.4.

4.4.5 Conclusions

The ultrasonic transducers developed for embedment in concrete have shown to be valuable tools for various tasks in structural monitoring. They met our expectations in frequency (around 60 kHz), directivity (almost circular around the main axis) and range (at least three meters). The transducers proved to be very robust. We have developed deployment systems for existing and newly built structures. Early versions are now embedded and used in lab samples and real structures for a few years and are still fully operational. We have shown that the transducers are useful in many applications. They can be used for active transmission experiments as well as for collecting passive acoustic emission data. They proved to be useful in lab samples, scale experiments and real-world monitoring systems. Load changes can be detected and localized as well as environmental influences (temperature, moisture) and various degradation mechanisms. If we add novel interpretation tools as Coda Wave Interferometry to the package, we have very sensible methods for the detection of changes in concrete at hand. The embedment in concrete has various advantages: The coupling to the concrete is constant, transducers at lab samples have not to be removed before putting them into climate chambers, chemical baths or similar and installations are more vandal proof and less accident prone on real constructions.

5 Seismic algorithms for ultrasonic echo testing

5.1 General remarks

Until 25 years ago, it was claimed that ultrasonic echo testing would never be applicable in practice due to the scattering of elastic waves at aggregates, cracks and pores, the lack of suitable transducers and the cost and ineffectiveness of available measurement devices. Meanwhile ultrasonic echo testing is applied on a regular basis and suitable devices are commercially available. Producing reliable images of the interior of concrete construction is of major concern to determine the geometry of the object or to locate built in features (e. g. tendon ducts) or to detect flaws (e.g. cracks or honeycombing).

Imaging ultrasonic echo data is a major issue in ultrasonic echo testing no matter whether it is applied to concrete, steel or in medical applications. Using a single transmitter and receiver, the reflected energy is not focused, and it can't be determined from which direction or depth the backscattered energy is coming. Two main approaches are followed to produce focused images of the subsurface. First, phased arrays (sets of transmitters sending/receiving signals with a controlled time delay) are used to send focused energy in a certain direction or to a certain point at depth (Figure 5-1). Arrays can be used as receivers as well. This approach is followed primarily in ultrasonic testing of metals and medical imaging. While some impressive research was done on implementing the phased array approach to concrete imaging (see e.g. Mielentz, 2007; Mielentz et al., 2015), it has not yet been used in practice. The main reason might be that it is extremely difficult to ensure constant coupling conditions for all transceivers in an array on a never fully smooth concrete surface.

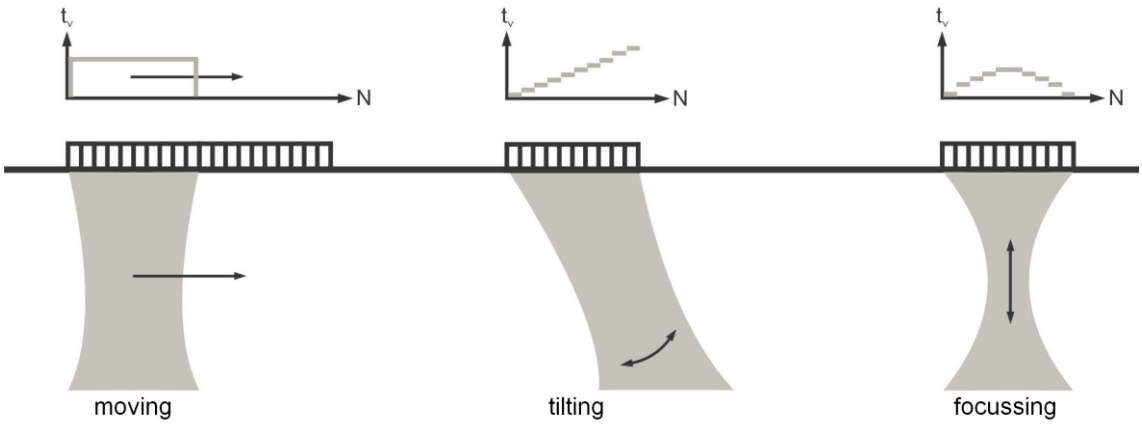

Figure 5-1: Schematic of the use if phased arrays in ultrasonic testing: By specific time delays (top) applied on a set of transmitters the sound field is either moved, tilted of focused (or any combination of those). From Mielentz (2007).

The second way to produce a focused image is to perform the transmitting and receiving by various combinations of point-like transducers or small arrays with zero-time lag ("multi-static arrays"), which is followed by an imaging procedure (Top: Figure 5-2). This approach has been up to now much more successful and applied in practice, especially after commercial multi-array devices with built-in imaging capabilities are commercially

available from more than one vendor ( ). Recently, a system with separated transducer arrays for deep penetration ("LAUS") has been introduced at BAM (Wiggenhauser et al., 2016). All are based on s_h-wave point contact transducers.

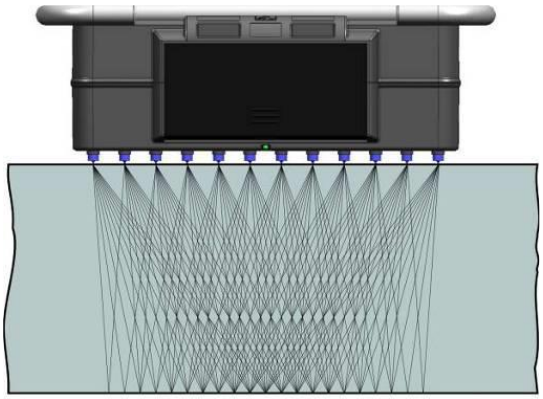

Top: Figure 5-2: Multistatic array in ultrasonic concrete testing: point contact transducers work and various combinations as transmitters and receivers. Drawing: BAM.

Right: Figure 5-3: Multistatic arrays ACS 1040 "Mira"(top) and Proceq Pundit 250 Array (bottom) with built in imaging capabilities. Pictures: BAM/Proceq.

Research on imaging procedures for ultrasonic echo concrete testing goes back more than two decades. Simple algorithms using a constant velocity assumption have been used to correct the time of arrival of echoes (and thus the depth of reflectors) before 1995. More sophisticated algorithms have been developed since, most of them summarized under the family name "Synthetic aperture focusing technique" (SAFT). Many developments have been come from (or are heavily influenced by) the group of the late Karl Langenberg at University of Kassel, Germany (Langenberg et al., 1997; Langenberg et al., 2009). The most used variants resemble well established geophysical migration techniques in the time domain (e. g. Kirchhoff migration) or the frequency domain (e.g. Stolt migration). Most of the time the developments in NDT and geophysics have been totally separate. However, there have been a few successful attempts to transfer geophysical imaging methods to concrete NDT. For example, Ballier et al. (2012) applied the one-way wave equation method to ultrasonic data to detect voids in tendon ducts. The state of the art of ultrasonic imaging is summarized by Krause et al. (2011). A corresponding software package for research ("InterSAFT") is supplied by Mayer (2012). Special versions e.g. for the new deep penetration device LAUS have been introduced recently (Mayer et al., 2015).

As mentioned earlier, all relevant commercial devices and most instrumentation used in ultrasonic echo research use s_h-waves polarized parallel to the measurement surface and

perpendicular to the direction of measurement (axis transmitter-receiver) to increase efficiency and to avoid wave mode conversion as much as possible. Beniwal et al. (2016) recently proposed a way to include wave mode conversion to improve the imaging result.

As in geophysics, all imaging techniques applied have specific issues. One of the main limitation of SAFT methods is the inability to image steeply dipping or even vertical boundaries. This is related to the fact, that these techniques (as Kirchhoff and many other geophysical methods) do not consider energy, which is reflected more than one time from the same or different boundaries. For this reason, they are incapable to image vertical cracks, thickness changes in the lower boundary of the construction or the backside of built-in objects as tendon ducts correctly.

Novel seismic imaging techniques, such as "Reverse Time Migration" (RTM), have the potential to overcome this limitation and to open new fields of application for ultrasonic echo testing. RTM has been developed in the last two decades and has seen regular application in hydrocarbon exploration in recent years. Section 5.2 shows the potential of RTM for ultrasonic concrete testing based on synthetic data, verified in section 5.3 on polyamide models. Section 5.4 shows one the first applications on concrete.

5.2 Reverse Time Migration (synthetic data)[4]

5.2.1 Introduction

Quality assurance and damage assessment of concrete structures as buildings, bridges, and dams are major tasks in civil engineering. On the one hand construction drawings may be missing or are considered to be unreliable, which is a drawback for maintenance and rehabilitation measures. On the other hand, parts of the public infrastructure, namely bridges, suffer from aging, increased traffic, and increasing individual truck weight. In addition, nondestructive inspection methods are required to provide a reliable quality assurance for new, repaired, or rebuilt structures. Since some twenty years ultrasonic techniques have been used more and more frequently to map the interior of structures, for example, to locate layers, voids, objects, or other features. The localization and characterization of tendon ducts is of major importance. These ducts are used to apply external forces to the concrete via prestressed steel wires to enhance its tension resistance. After stretching these wires, the duct is grouted with mortar to couple the stressed wires and the concrete as well as to avoid corrosion. Remaining air voids are a problem for the durability of the structure. In many cases the first step in an assessment is to locate the tendon ducts, because often they are not placed in accordance with the design plans. Until 20 years ago, ultrasonic testing in civil engineering had been limited to relatively simple methods, such as time of flight transmission measurements to assess concrete quality. Meanwhile echo measurements are a well-established nondestructive testing method in civil engineering. Recently, the introduction of new transmitters and receivers, array techniques, and data processing methods has led to the development of imaging applications in research and practice. The data acquisition geometries as well as wave phenomena are like those in seismic techniques, but on a different scale. Imaging is mainly done using SAFT (synthetic aperture focusing technique), which is closely related to Kirchhoff migration. Thereby it suffers from the same limitations, for example, problems with imaging of vertical or steeply dipping interfaces. Measurements are done mainly using a zero-offset geometry. This means that receiver and transmitter have a constant distance of some centimeters. For this reason, only the top of, for example, tendon ducts can be

[4] This section is an edited version of Müller et al., 2012.

imaged. The duct also shadows the back wall and any other structural features behind it. Details on SAFT algorithms applied to measurements on concrete have been published by Mayer et al. (1990) and Schickert et al. (2003). Krause et al. (2011) have compiled the state of the art on imaging grouting faults in tendon ducts. An extension of the method using phase analysis of the measured signal reflections was published by Krause et al. (2008). In exploration seismics several methods have been introduced to image complex structures including steeply dipping interfaces. A promising technique called reverse time migration (RTM) was originally introduced by Baysal et al. (1983), Loewenthal & Mufti (1983), and McMechan (1983). However, due to the required computing power, it was not until after 2000 that RTM became a practicable method. Some examples of recent applications of RTM in hydrocarbon exploration are shown by Farmer et al. (2009). Other authors have experimented successfully with the application of RTM in structural health monitoring of composites, for example, crack detection (Zhou et al., 2007, Wang, 2005). In this section, the potential of RTM for ultrasonic testing in civil engineering and the advantages compared to SAFT using synthetic models is shown.

5.2.2 Reverse Time Migration

The basic idea of RTM is a three-step procedure of (a) forward modelling of a wavefield through an appropriate velocity model as well as (b) back propagation of the measured data through the very same model and (c) superposition of both using an imaging condition. The complete wave equation is used for the simulation. There are no dip restrictions for imaging because the entire wavefield including multiple reflections is used. Thus, even vertical boundaries or lower edges of objects can be imaged. The RTM algorithm used in this paper is based on a finite difference modelling code by Bohlen (2002). Currently we are using the two-dimensional acoustic wave equation. Some improvements for full waveform inversion, acoustic modelling with perfectly matched layers as boundary condition, and shot parallelization were done by Kurzmann et al. (2009). The code can be applied to different tasks from high frequency ultrasonic measurements to exploration seismics. It provides a set of parameters to be adapted to the specific problem. For example, arbitrary source functions can be chosen to mimic ultrasonic transducers or explosive sources. In our examples, a Ricker wavelet was used as source signal and perfectly matched layers as boundary condition.

Figure 5-4 shows the principle of RTM for a 2D case with coordinates x (horizontal) and z (vertical). In an experiment data are acquired using several sources and receivers. The recording time must be sufficiently long to include multiple reflections. A velocity model must be chosen for the imaging process. A homogeneous or smoothed model is used in most cases. For all shot point configurations two simulations are performed using the very same model: (a) forward simulation using an appropriate source function at the shot point to calculate the wavefield $S_s(t,x,z)$ and (b) reverse modelling using the reversed measured data as a source function at the corresponding receiver points to calculate a second wavefield $R_s(t,x,z)$. After the simulation, an imaging condition is applied. In this case, a zero-lag cross-correlation was used, which is normalized by the square of the source illumination strength. The correlation images of all shots are summed up to get the image I(x,z) (Kaelin & Guitton, 2006):

$$I(x,z) = \sum_s \frac{\sum_t S_s(t,x,z) R_s(t,x,z)}{\sum_t S_s^2(t,x,z)} \qquad (5\text{-}1)$$

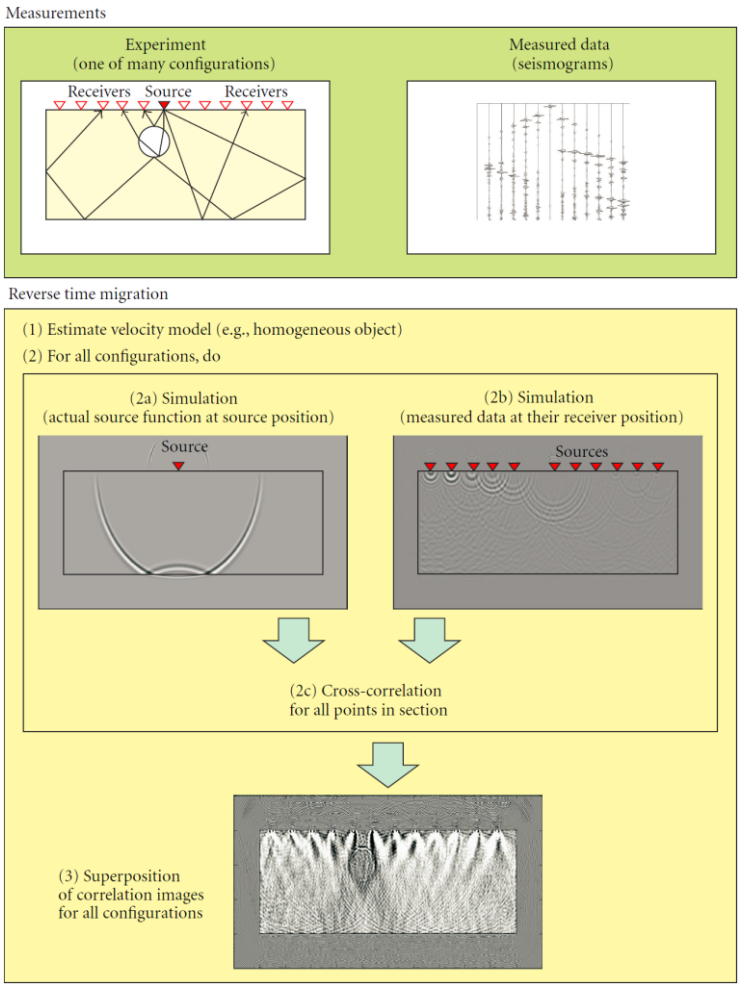

Figure 5-4: Principle of reverse time migration

5.2.3 Simulation of typical problems in nondestructive testing

We have tested the RTM with synthetic data, which we had generated with the forward modelling part of the RTM code. Several synthetic models have been created to study different tasks in nondestructive testing. The first models represent polyamide specimen, a homogeneous, diffraction-free material. In a second step, a concrete-like structure with multiple scatterers was simulated. Four polyamide models have been chosen to show the capabilities of the algorithm: one step (in the lower boundary), two steps, an air inclusion, and a step with an air inclusion. The models consist of 1200 by 500 grid points with a distance between grid points of 0.001 m. The specimens have a maximum size of 1 m by 0.30 m and compressional wave velocity of 2687 $m \cdot s^{-1}$. The specimens are surrounded by an 0.10 m width air layer with a velocity of 333 $m \cdot s^{-1}$. On the top surface of the polyamide specimen we positioned the 12 sources and coincidental receivers with 0.08 m between them. If a Ricker wavelet with f = 100 kHz is inserted at every shot point, all 12 receivers are in recording mode. The recording time is t = 0.6 ms with a time step of 0.1 µs. This way even multiple reflections are recorded.

For all following RTM reconstructions, a homogeneous, rectangular velocity model (c_p = 2687 $m \cdot s^{-1}$ as in data generation) was used, shown in Figure 5-5. This way, the algorithm has no information about the real structure, except for the outer limits and the material velocity.

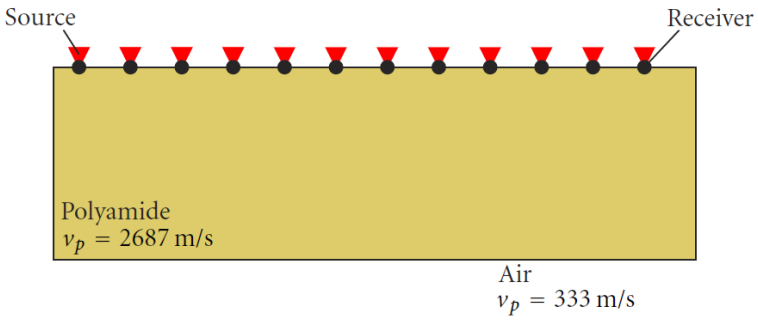

Figure 5-5: Homogeneous velocity model used for migration.

Model 1: One step. The first synthetic model includes a small step in the lower boundary of the polyamide specimen (Figure 5-6(a)). The step has a height of 0.10 m. Figure 5-6(b) shows the result of the RTM calculated with the homogeneous velocity model. The step is imaged in the correct position and height. The vertical border of the step is clearly visible. There are also artifacts at every multiple height of the step, which are not completely explained until now. They are probably an effect of the cross-correlation, as the velocity model used here intentionally does not include the step. So, the forward wavefield contains no information about the step while the back propagation (using the measured data) does. This way, one gets a high signal in the cross-correlated image at the real step position, but also lower signals in multiple distances. The longer the recording time, the more multiple reflections are recorded. That is why the amplitude of the artifacts increase with longer recording time. This result shows the importance of choosing a proper recording time for experiments, long enough to image the entire structure, but not too long to enhance artifacts.

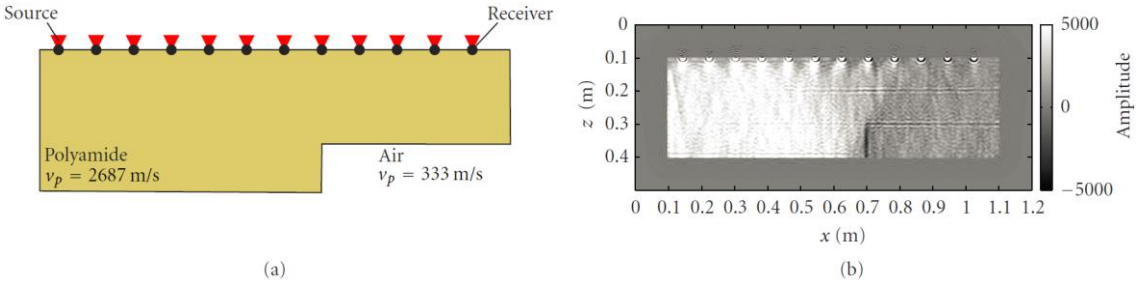

Figure 5-6: (a) Synthetic step model. (b) RTM imaging result using velocity model of Figure 5-5.

Model 2: Two steps. The next model consists of two steps with a height of 0.06 m for each step (Figure 5-7(a)). Figure 5-7(b) shows the migrated image generated with the homogeneous rectangular model. Now only the first step is imaged at the right height and with a clear vertical border. However, the second step is missing. Only artifacts by multiple reflections are imaged. Apparently, RTM fails, if the model used for reconstruction is too far from reality. The reason is, that the backwall is serving as a kind of a mirror for travel paths including the vertical face. If this mirror is not included in the velocity model at the correct position, the imaging fails. Thus, we have tried a kind of two-stage RTM. We used the information from the first reconstruction, the imaged step at the left, and created a new velocity model (Figure 5-8 (a)). Figure 5-8(b) shows the result of the second RTM using the improved velocity model. Now the second step is clearly visible. This example illustrates that for more complicated models a multistage RTM is required if insufficient a priori information is available about the structure.

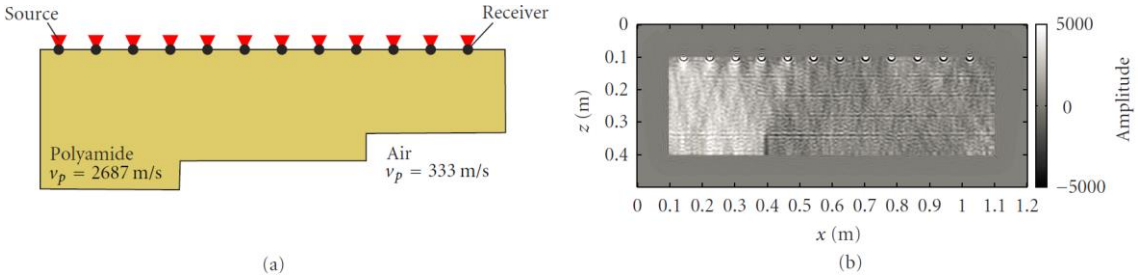

Figure 5-7: (a) Two-step model. (b) RTM imaging result using velocity model of Figure 5-5.

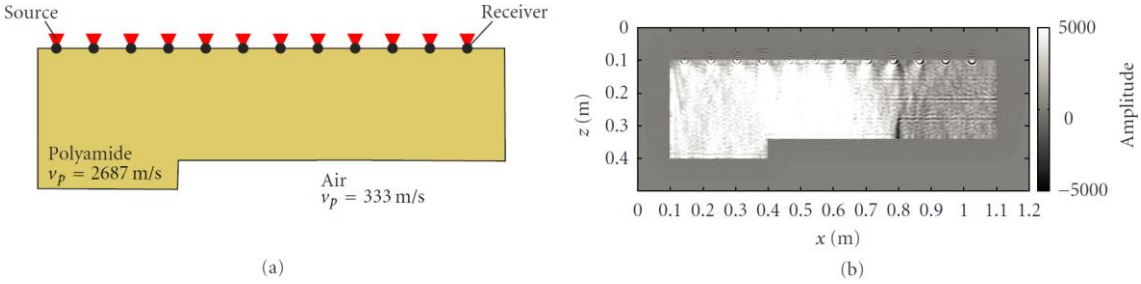

Figure 5-8: (a) Modified velocity model for migration. (b) RTM imaging result of the two steps using the modified velocity model.

Model 3: Air inclusion. The next model includes a circular-shaped air inclusion in polyamide. The circle has a radius of 0.05 m. The midpoint is at x = 0.5 m and z = 0.2 m (Figure 5-9 (a)). Figure 5-9(b) shows the result of the RTM, again calculated using the homogeneous velocity model. The complete circular boundary of the inclusion is imaged. This is a significant improvement compared to Kirchhoff migration or SAFT, which can image the upper side of the inclusion only.

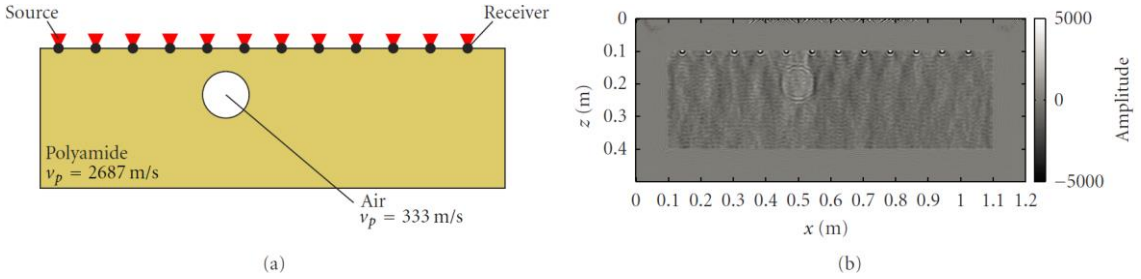

Figure 5-9: (a) Synthetic air inclusion model. (b) RTM imaging result using velocity model of Figure 5-5.

Model 4: Step with air inclusion. The last polyamide model is a combination of the step model and a smaller air inclusion. The step has again a height of 0.10 m. The midpoint of the inclusion is located at x = 0.4 m and z = 0.25 m, and it has a radius of 0.03 m (Figure 5-10 (a)). Figure 5-10(b) shows the migrated image. This example shows that also different defects inside a specimen can be located simultaneously. The vertical border of the step is imaged as well as the boundary of the inclusion. As already seen in the first model (Section 3.1), artifacts are generated by imaging the step using a rectangular velocity model.

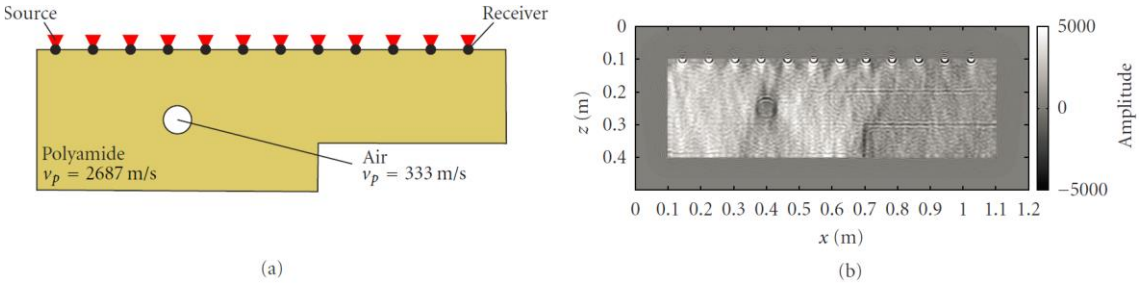

Figure 5-10: (a) Step with air inclusion model. (b) RTM imaging result using velocity model of Figure 5-5.

Model 5: Scattering Model with Air Inclusion. To simulate experiments on concrete, we have designed an additional model, which includes the scattering effect of aggregates. In real concrete, the size of the aggregates (e.g., gravel) is in the same order of magnitude as the ultrasonic wavelength. 300 circular scatterers have been arranged in the synthetic specimen. Figure 5-11(a) shows the model. The model consists of 1200 × 700 grid points with a spacing of 0.001 m between them. The size of the specimen is 1 m by 0.5 m surrounded by an air layer of 0.1 m thickness. The background velocity of the specimen is 4000 m·s^{-1} and of the surrounding air layer 333 m·s^{-1}. The 300 randomly arranged scatterers have a velocity range from 3000 m·s^{-1} to 4000 m·s^{-1} and a size between 2 mm and 16 mm. The midpoint of the air inclusion is located at x = 0.5 m and z = 0.3 m, with a radius of 0.05 m. RTM was performed with a source/receiver distribution like the geometry used for the polyamide models. These experiments showed no success as the scattered wave energy blurs the image. To achieve better results, additional receivers were added to average the signal. Finally, 10 sources were placed with a distance interval of 0.1 m, and 45 receivers with a distance interval of 0.02 m. A Ricker wavelet with f = 100 kHz was used as source function. The signal was recorded for 0.6 ms with a time stepping of 0.1 µs. For the RTM, we have chosen a homogeneous model again with the same background velocity as the real model, v_p = 4000 m·s^{-1}, but without the scatterers and the inclusion (Figure 5-11(b)). Figure 5-11(c) shows the migrated image. The boundary of the inclusion is completely visible, but the amplitude is significantly lower than in the previous examples. Especially the left and right sides of the inclusion are imaged weakly. Increasing the recording time did not improve the result. Indeed, by using a longer recording time more multiples and reflections from the boundaries of the specimen are included as well as scattering noise. For this reason, the signal-to-noise ratio decreases, and the image of the boundaries of the inclusion weakens.

Comparison to SAFT: A quantitative comparison between RTM and SAFT imaging is not possible in the current stage. The decisive difference between them is the acquisition geometry. All the examples for RTM quoted above are calculated with a multi-offset geometry. The SAFT algorithms available at the time of this study for nondestructive testing required constant offset measurements. In addition, the distance between shot points used for RTM is large compared to SAFT. For a detailed SAFT imaging of concrete a distance of 0.02 m is used usually. For RTM, we used 0.08 m. However, it was possible to show that RTM is capable to image vertical and circular inhomogeneities, which is not feasible with aperture limited approaches, such as SAFT. An example for results acquired by SAFT and RTM on a real concrete block supporting the findings given here was published by the same authors (Müller et al., 2010; Müller & Niederleithinger, 2014), another is given in section 5.4.

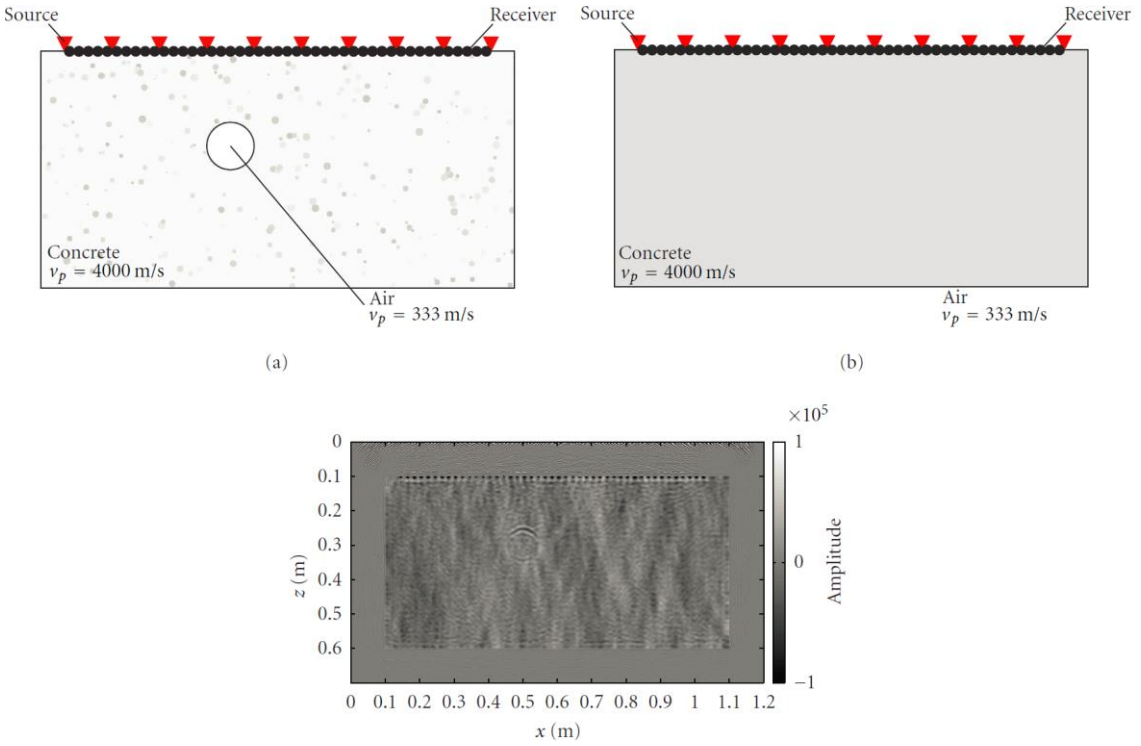

Figure 5-11: (a) Concrete-like synthetic model with an air inclusion. (b) Homogeneous velocity model for migration. (c) RTM imaging result using velocity model of (b).

5.2.4 Conclusions and outlook

By using different polyamide models and a concrete-like synthetic model the potential of the RTM for nondestructive testing in civil engineering was demonstrated. Vertical borders and lower parts of built-in elements can be imaged clearly. The image quality can thus be improved, and more faults can be found compared to conventional imaging techniques. Artifacts which have been seen in RTM images must be carefully analyzed and eliminated. For this task, imaging conditions other than cross-correlation may be used but have not been explored for NDT so far. In addition, improved velocity models should be chosen for the RTM to improve the resulting image. For more complicated tasks a multistage RTM can be helpful to image all features. Experiments on test specimens of polyamide and concrete under laboratory conditions are currently performed to evaluate the synthetic results. Measurement equipment as well as acquisition parameters should be tested and optimized to obtain a good signal-to-noise ratio. The RTM code so far assumes point sources, while many sensors used in practice have a contact area of a size greater than the wavelength. Another topic to be worked on is to expand the algorithm to three dimensions and to use the full elastic wave equation. In nondestructive testing on concrete most measurements are carried out using shear waves, as smaller defects can be detected this way. To include this, other imaging conditions have to be adapted and the computing efficiency should be improved as well.

5.3 Verification on polyamide model data[5]

5.3.1 Introduction, Reverse Time Migration, synthetic data

The methodology of RTM has been presented in the paper reproduced in section 5.3. In the same section, it was shown using simulated data, that RTM can image ultrasonic echo data and maps vertical faces as well as the full perimeter or circular voids. This section is focused on the verification of these findings on a real data set.

5.3.2 Test specimen and measurement setup

For our evaluation experiments, a Polyamide specimen of 1 x 0.6 x 0.3 m^3 was cast (Figure 5-12). Polyamide was chosen for our first trials for its homogeneity. It allows to acquire ultrasonic echo data without the large amount of scattering inherent to concrete. A hole was drilled into the specimen parallel to the measurement surface from one side to the other, which was widened stepwise from 0.02 m to 0.05 m diameter. As the hole is off center we have the possibility to perform detection trials with different depth to surface and to avoid any overlap of (multiple) reflections.

Figure 5-12: Polyamide test specimen

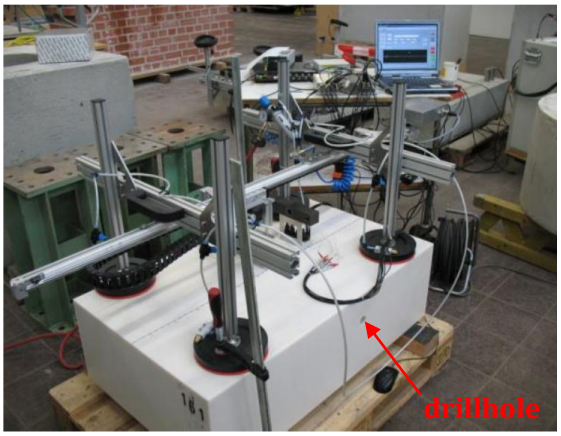

Figure 5-13: Ultrasonic scanning system on Polyamide test specimen

Measurements were performed with one of the ultrasonic scanning systems developed for automatic deployment at BAM. The system used here consists of a transmitter, which must be positioned manually and a receiver, which is moved by the system (Figure 5-13). This allows a fast and precise data acquisition. Both transmitter and receiver have been arrays of four point-contact transducers, mounted in a single row perpendicular to the direction of the measurement line with 0.02 m between transducers (Figure 5-14). Using this array reduces the amplitude of surface and direct waves propagating sidewards. The energy is focused along the line of measurement. In a vertical 2D section along the measurement line (which is considered in the 2D RTM performed later) these arrays are still point sources/receivers. Measurements were performed from both sides with p- and s_h-wave-transducers, but only data from s_h-waves (polarization perpendicular to the measurement line) are presented here. The radiation characteristics of the s_h-array used has been tested using measurements on a polyamide half sphere. They match the characteristics of the simulated source in the 2D acoustic RTM code.

Ultrasonic data were acquired using 12 source positions (distance 0.08 m) and 45 receiver positions (0.02 m distance). Due to the physical dimensions of the arrays we had to skip not only the receiver position coincident with the transmitter, but also two more ones to the left

[5] This section is an edited version of Müller & Niederleithinger, 2014.

and right. The transmitter was connected to a signal generator producing a rectangular signal with 100 kHz (p-waves) or 50 kHz (s_h-waves). Due to the limited bandwidth, the real signal transmitted into the material resembles one period of a sine wave. Acquisition time at the receivers was 2 ms. Only a part of the signals was used for RTM to avoid artifacts by multiples.

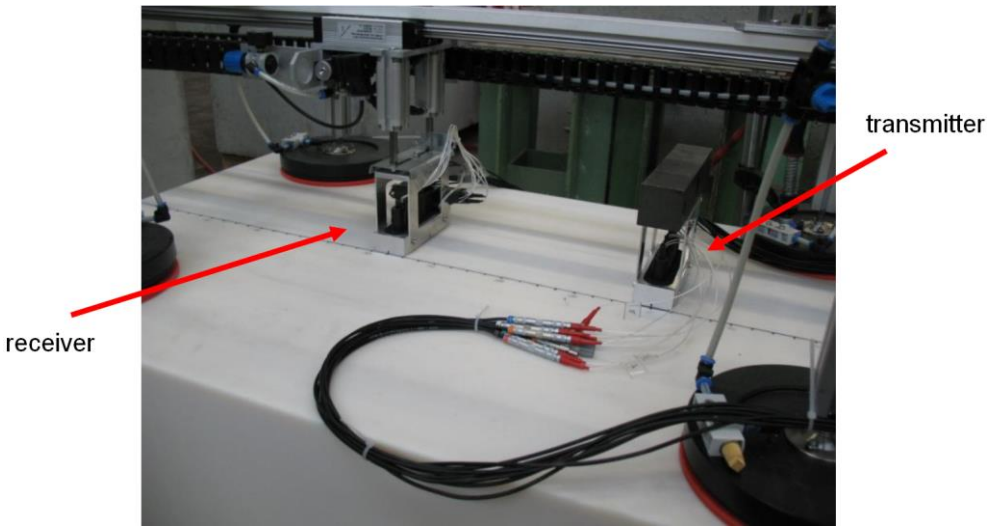

Figure 5-14: Transmitter and receiver array on the surface of the Polyamide test specimen

5.3.3 Migration results

Migration has been performed using the same 2D acoustic RTM code as for the synthetic data in section 5.2. A homogeneous velocity model, using the known dimensions of the Polyamide specimen and an experimentally determined velocity, was used. An air layer was simulated around the Polyamide. The velocity model did not contain any information about the drill hole.

Figure 5-15 and Figure 5-16 show the migrations results for ultrasonic s_h-data acquired on the Polyamide specimen with drill hole diameters of 0.02 m or 0.04 m, respectively. In both case energy is nicely focused at the lateral edges and at the bottom of the specimen, as the velocity model was exact for these features. Figure 5-15 shows, that the drill hole is visible at the exact location as an almost circular feature even for a size smaller than the dominant wavelength used (here: $\lambda = 0.025$ m). For larger diameters (Figure 5-16) the diameter can be easily determined with an accuracy of about 5 mm.

5.3.4 Conclusion

Reverse Time Migration has great potential for nondestructive testing in civil engineering. The results achieved with real data from a Polyamide model confirm the promising results achieved with synthetic data. The four-element transceiver s_h-arrays allowed the use an acoustic 2D RTM code. The migration results showed the drill hole in the full perimeter.

The methodology has now to be applied on concrete constructions. We expect more difficulties due to the irregular scattering of ultrasonic waves inherent to concrete.

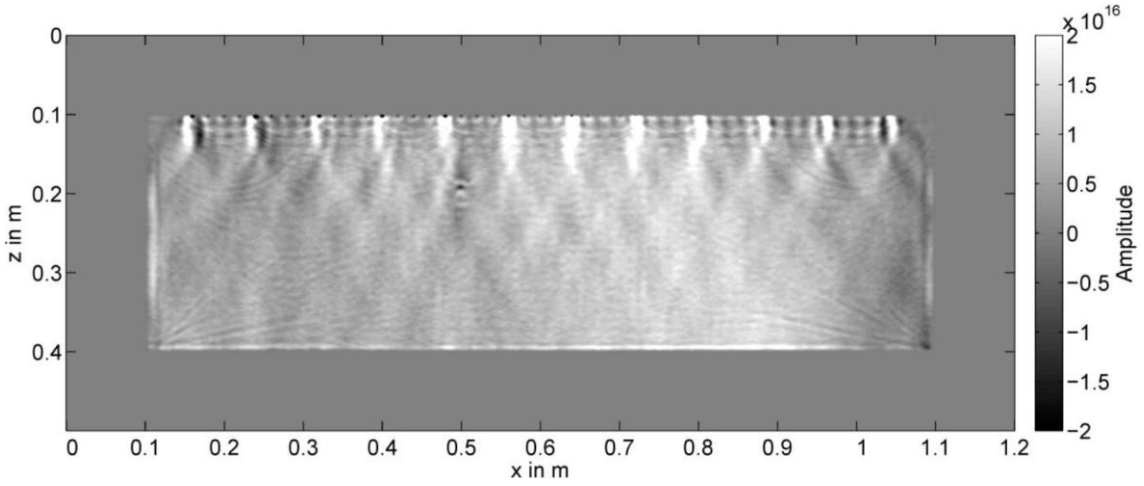

Figure 5-15: RTM migration result for ultrasonic s_h-wave data on a Polyamide specimen containing a 0.02 m diameter horizontal drillhole

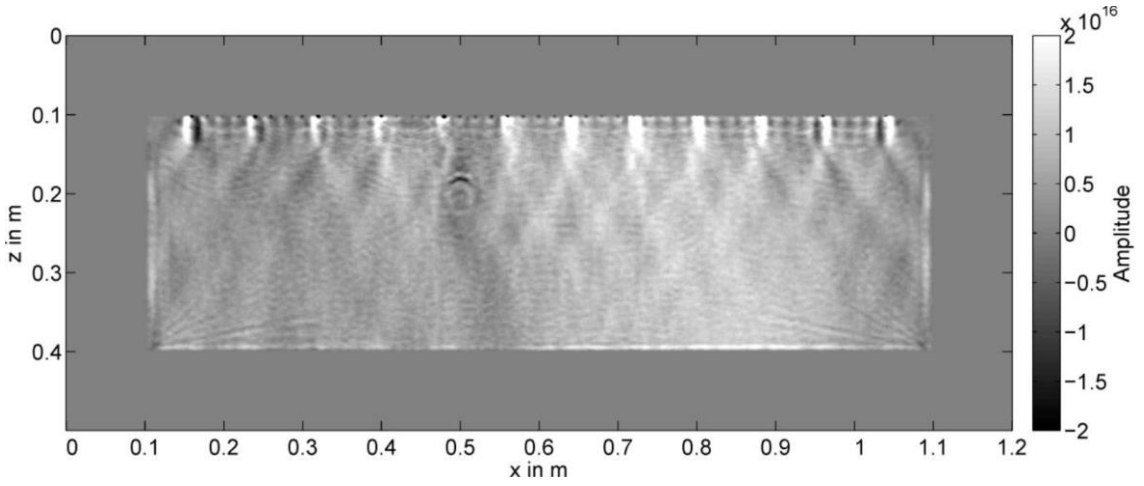

Figure 5-16: as above, drillhole diameter 0.04 m.

5.4 Application to real data (concrete)[6]

5.4.1 Introduction

The previous sections have shown that RTM has great potential to overcome some of the issues of conventional imaging techniques currently used in nondestructive testing (NDT) of concrete constructions. Hu et al. (2014) meanwhile tested RTM using synthetic ultrasonic data obtained with a two-dimensional numerical model consisting of a flaw embedded in a concrete structure. A recent example for the usage of RTM on focused synthetic and experimental ultrasonic data was published by Beniwal et al. (2015). The authors showed that RTM is suitable for detecting defects around steel rebar in a concrete medium.

This section demonstrates the use of RTM for a data set acquired on a real scale concrete foundation slab. The results are compared to the SAFT algorithms (Schickert et al., 2003; Krause et al., 2008; Mayer et al. (2008); Mayer et al., 2008), which had been meanwhile extended to cope with variable and arbitrary transmitter-receiver offsets. However, the SAFT imaging technique has still inherent difficulties in imaging vertically dipping interfaces and complicated structures such as steps and lower boundaries of voids. In

[6] This section is edited from Grohmann et al., 2016.

addition, the RTM results will be compared to pre-stack Kirchhoff migration, a ray-based migration algorithm (Bleistein & Gray, 2001) closely related to SAFT. This method was the dominant migration algorithm in the oil and gas industry in the late 1990s.

Within the next subsection the test specimen is introduced. Thereafter, an overview over the geophysical migration methods used is given. The following two subsections demonstrate the application of the geophysical migration methods and SAFT to synthetic and experimental ultrasonic echo data as well as a comparison of the imaging results. This is followed by a discussion of the reconstruction results as well as conclusion s and outlook.

5.4.2 Test specimen: foundation slab RuFUS

The test object, a reinforced concrete foundation slab (Figure 4-17), was built in 2003 at the test site of the Federal Institute for Materials Research and Testing (BAM) as part of the EU funded research project RuFUS (Re-use of Foundations on Urban Sites). The foundation slab is embedded in compacted sand and consists of areas of different thickness, ten different reinforcement levels, a strip foundation and two piles. A 0.05m thick layer of lean concrete is located below the bottom of the foundation slab. Figure 5-18 shows this layer and the different levels of reinforcement before concreting. The tasks with respect to the foundation slab were thickness determination as well as imaging the vertical step, the two pile heads and the strip foundation. In addition, the dependency of the resolution on various factors (such as 3D effects and the reinforcement) was investigated.

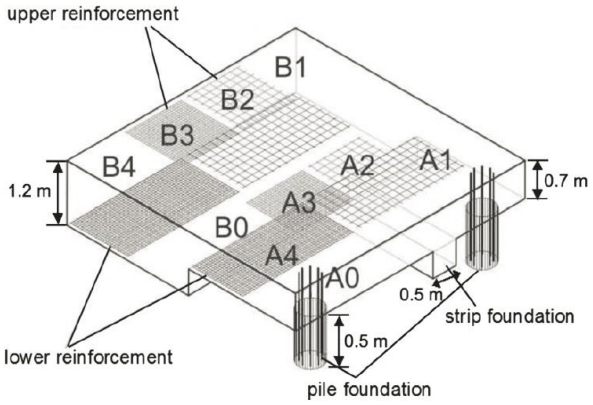

Figure 5-17: Geometry of the RuFUS foundation slab (from Taffe, 2008).

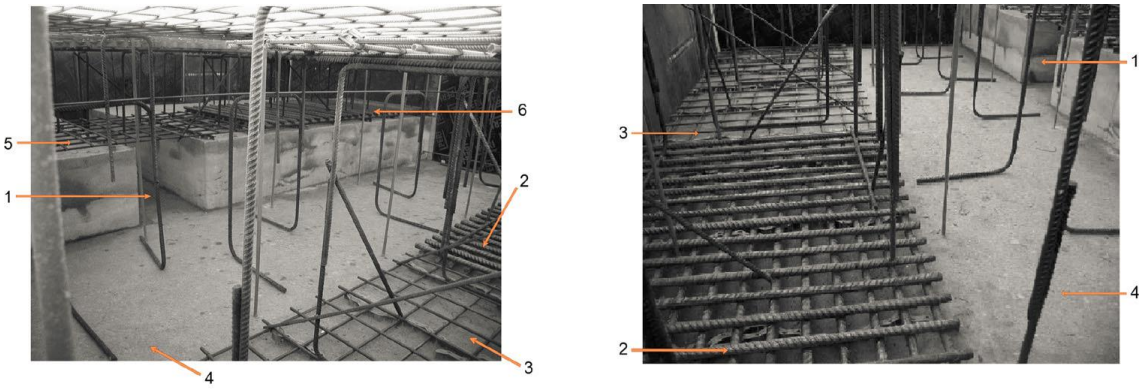

Figure 5-18: (a) and (b): Views on the lean concrete layer and different levels of reinforcement before concreting (1: Strip foundation, 2: Reinforcement mesh B4, 3: Reinforcement mesh B1, 4: Lean concrete layer, 5: Reinforcement mesh A1, 6: Reinforcement mesh A4). From Krause et al. (2008).

Figure 5-19 shows a vertical cross-section of the homogeneous 3D-SAFT reconstruction for a line profile on the foundation slab calculated with the InterSAFT Software (Mayer & Cinta, 2012). The data was measured and processed as is state of the art in practical applications in civil engineering. Due to the heterogeneity of the concrete and correspondingly rather complex waveform of the reflected signals, the envelope of the signal was calculated before the summation to obtain a more robust result. The ultrasonic measurements were made using the device A1220 (ACS Ltd., 2014) in 2005. This array consists of 12 transmitting and 12 receiving dry point contact transducers in a fixed distance which excite shear waves (bistatic measuring setup). In the SAFT reconstruction the image of the lower boundary of the slab has several gaps. The pile head, imaged as a gap in the boundary, is shown in the correct position. The pile shaft and the vertical border of the step were not reconstructed. The result clearly illustrates the limitations of the SAFT algorithms since no vertical reflectors inside the slab were imaged.

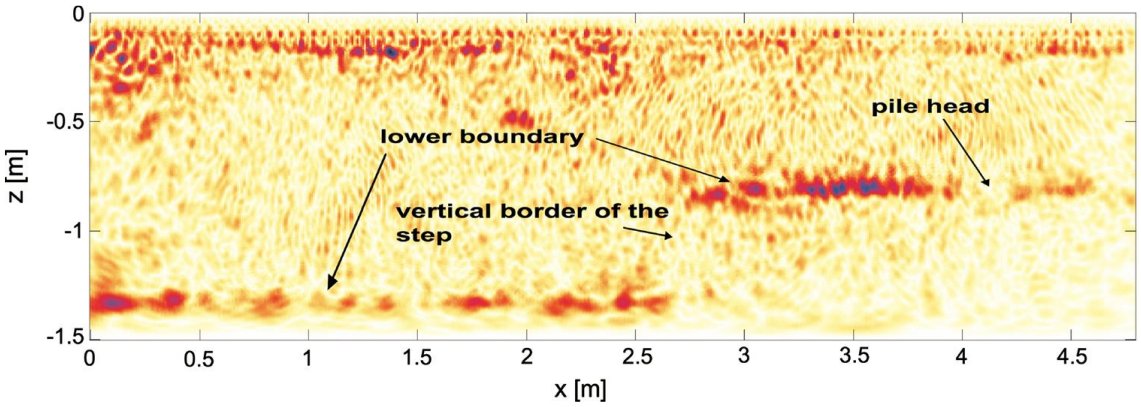

Figure 5-19: 3D-SAFT reconstruction of fixed offset ultrasonic data collected 2005 on the foundation slab with a pile head and the vertical step. Blue/Red corresponds to high and white to low values of the amplitude envelope.

5.4.3 Geophysical imaging methods

In geophysics, the process of placing the recorded seismic reflection energy in its proper subsurface location and thus producing an image of the investigated underground is called migration. A migration process converts the received information as a function of recording time to features in subsurface depth. Over the past decades, a wide range of geophysical migration methods have been developed for the exploration of hydrocarbons. Here, two pre-stack depth migration techniques were applied. For these methods, the data of each single shot are migrated prior to stacking all information into one image. Advantages of pre-stack migration techniques are preservation of amplitude information and a significant improvement of the signal-to-noise-ratio (Buske, 1994). The pre-stack Kirchhoff migration method was selected because of its similarities with SAFT algorithms and the pre-stack Reverse-time migration technique due to its capability to use more information than just direct reflections.

5.4.3.1 Reverse Time Migration

The principle of Reverse Time Migration (RTM) is explained already in section 5.2.2. Other than for the synthetic and real data experiments using a Polyamide model shown before, we have used a different computer code here. The algorithm we worked with is based on a 2D-finite difference modeling code included in the Madagascar software package (Fomel et al., 2013). The modeling program we worked with uses a regular grid and is accurate fourth-order in space and second-order in time. Madagascar is a package for multidimensional data analysis and reproducible computational experiments and mainly used by researchers working with imaging and data processing of geophysical data. Since we applied a

geophysical migration technique to ultrasonic data collected on concrete, we had to build our own reproducible RTM code using the functions already implemented in Madagascar. For ultrasonic imaging, we had to adapt several simulation parameters and conditions as for example the implementation of the free surface boundary condition.

Figure 5-20 shows the principle of RTM. For demonstration, a two-dimensional model is chosen, containing a concrete structure embedded in sandy soil. Steps two to four are performed separately for each source-receiver configuration:

1. Estimation of a velocity and density model for the imaging process.
2. The source wavefield S_s is propagated forward in time using the source location, the source wavelet and the estimated velocity and density model.
3. The receiver wavefield R_s is propagated backward in time, from all receiver locations using the recorded data and the estimated velocity and density model. For the reverse modeling, the migration algorithm converts the receivers into sources and propagates the recorded data back into the subsurface.
4. The imaging condition used here computes the zero-lag local cross-correlation between the two simulation results at all model grid points to find the positions of subsurface reflectors (e. g. Sava & Hill, 2009):

$$I(x,z) = \sum_s \sum_t S_s(t,x,z) R_s(t,x,z) \quad [7] \qquad (5\text{-}2)$$

   where I (x, z) is the image intensity at location (x, z) and t is the recording time.
5. For the result, the correlation images of all configurations are superimposed ("stacked").

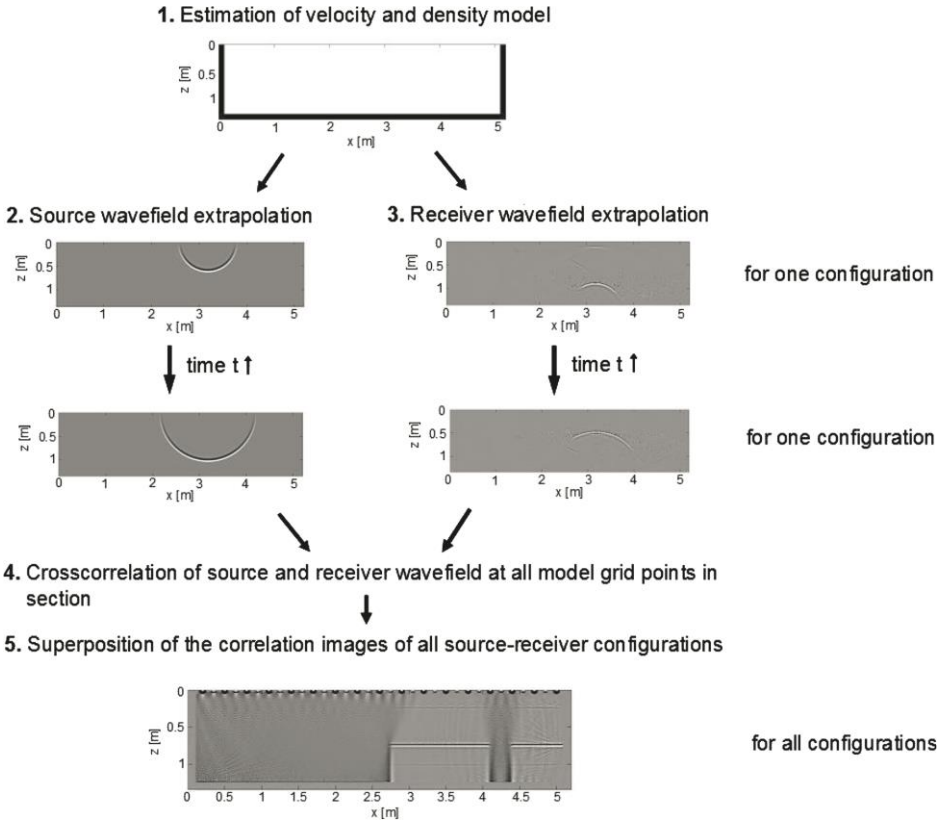

Figure 5-20: Principle of Reverse Time Migration

[7] This formula differs from (5-1) used in section 5.2.2 by omitting the scaling term. Experiments have shown, that the effect on the features of interest in the images shown in this section is negligible.

5.4.3.2 Kirchhoff migration

The pre-stack Kirchhoff migration method is, in principle, a weighted diffraction stack. The algorithm is based on the Kirchhoff integral solution of the scalar wave equation (Schneider, 1978). An implementation by Buske (1999) was used here, where the basis is the three-dimensional wave equation without a source term. The migrated section follows from the approximate Kirchhoff integral solution of the latter by (e. g. Buske, 1999):

$$M(x,y,z) \approx \frac{1}{2\pi c} \iint_A \frac{z}{r^2} \frac{\partial p}{\partial t}(x',y',z'=0,t_s+t_r)\,dx'dy' \qquad (5\text{-}3)$$

where p is the acoustic pressure and c denotes the acoustic velocity. According to (5-3), M(x,y, z) can be formulated as a surface integral over the aperture A and can be calculated by spatial integration of the weighted time derivatives of the recorded wavefield along the diffraction surfaces. t_s and t_r are the travel times from the source and receiver position to the image point in the subsurface, respectively.

For travel time calculation, a finite difference solution of the eikonal equation based on Podvin & Lecomte (1991) was used. The weighting factor z/r^2 in (5-3) is used to account for the correct treatment of amplitudes, i.e. it involves the adjustment of the amplitudes for geometrical spreading. It depends on the depth z and the distance r of the subsurface point (x, y, z) to the corresponding receiver position (x', y', z' = 0) (Buske, 1999):

$$r = \sqrt{(x'-x)^2 + (y'-y)^2 + z} \qquad (5\text{-}4)$$

Alternatively, Kirchhoff migration can be described by smearing the wavefield p along the corresponding two-way travel time isochrones. The final image is then generated by constructive interference of these isochrones along the reflectors.

5.4.4 Application to synthetic data

5.4.4.1 Simulation

In a first step, we tested Kirchhoff migration and RTM with synthetic 2D data to prove the concept of both geophysical migration techniques to image ultrasonic echo data and to obtain information about appropriate parameters for the later following ultrasonic measurements (e.g. number and positions of sources and receivers, recording time, measurement frequency). We chose a 2D section through the foundation slab, which contains the vertical step, a pile and the reinforcement meshes A1 and B1 (Figure 5-21).

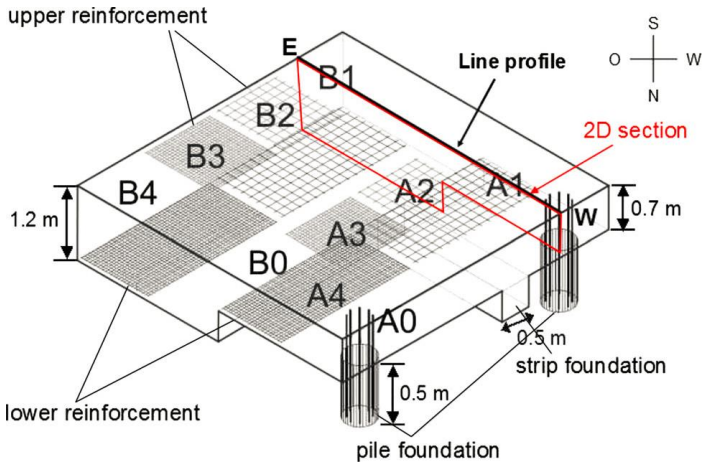

Figure 5-21: 2D section through the foundation slab (marked red) and line profile for the ultrasonic measurements (marked black). From Krause et al. (2008).

The material parameters used in the velocity and density models for the simulation process are listed in Table 5-1. The geometry of the velocity and density model as well as the boundary conditions used are shown in Figure 5-22. For simplification, both models are idealized. They do not contain any small-scale scattering obstacles inherent to concrete, since their precise distribution is not known. The 0.05 m thick lean concrete layer is included in the concrete part of the model since both layers have similar material properties. The reinforcement was neglected.

Table 5-1: Shear wave velocity vs and density values ρ for the simulation

material	velocity vs ($m \cdot s^{-1}$)	density ρ ($kg \cdot m^{-3}$)
reinforced concrete	2750	2400
compacted sand	300	1800

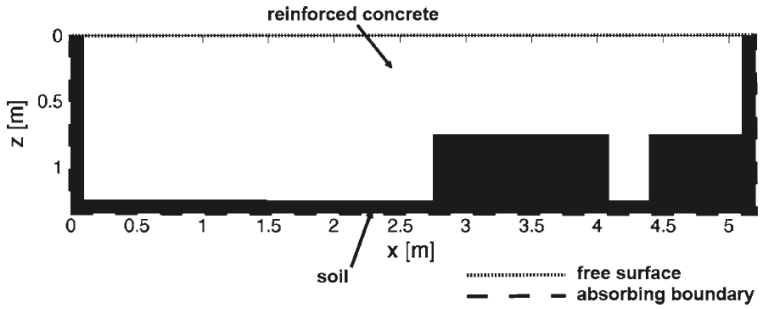

Figure 5-22: Structure of the velocity and density model for the synthetic data simulation, including a vertical step and a pile head.

Table 5-2 summarizes the simulation parameters used. The model consists of 5200×1350 grid points with a grid spacing of 0.001 m. A Ricker wavelet with a center frequency of 25 kHz was used as source signal.

Table 5-2: Parameters for the simulation process

Parameter	value
Model size	5200 × 1350 grid points
Distance between grid points	0.001 m
Frequency of the Ricker wavelet	25 kHz
Time step dt	$1 \cdot 10^{-7}$ s

5.4.4.2 Migration results: Reverse Time Migration

Table 5-3 contains the parameters for the synthetic data generation and RTM, which led to the most accurate image. We simulated 33 shots using 242 receiver positions (distance 0.02 m). Simulated recording time was 1.11 ms with a time step of $1 \cdot 10^{-7}$ s. Figure 5-23 shows the structure of the velocity and density model used for RTM. The outer limits of the foundation slab are assumed to be known. The model does not contain the step and the pile.

Table 5-3: Parameters for the synthetic data generation and RTM

Parameter	value
Number of sources	33
Number of receivers	242
Distance between sources	0.15 m
Distance between receivers	0.02 m
Source position no. 1	0.02 m
Receiver position no. 1	0.02 m
Recording time	0.00111 s
Velocity—simulation	c_{sc} = 2750 m·s^{-1}, c_{ss} = 300 m·s^{-1}
Velocity—RTM	c_{sc} = 2750 m·s^{-1}, c_{ss} = 300 m·s^{-1}
Density—simulation	ρ_c = 2400 kg·m^{-3}, ρ_s = 1800 kg·m^{-3}
Density—RTM	ρ_c = 2400 kg·m^{-3}, ρ_s = 1800 kg·m^{-3}
Thickness of concrete	*1.25 m*

c_{sc} shear wave velocity of the concrete layer, c_{ss} shear wave velocity of the sand soil layer, ρ_c density of the concrete layer, ρ_s density of the sand soil layer

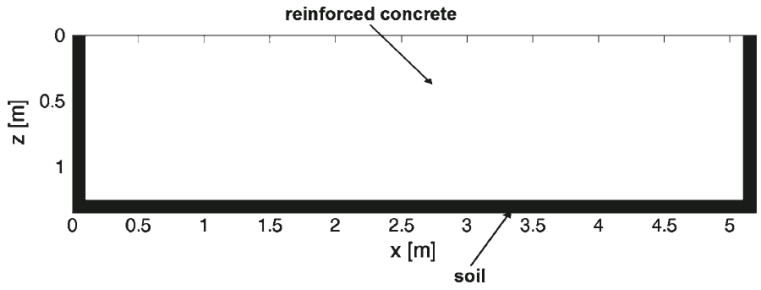

Figure 5-23: Velocity/density model used for RTM of the synthetic data set. White area: Concrete. Black area: Soil.

The migrated image is shown in Figure 5-24 The vertical step is reconstructed perfectly in terms of width and height. Furthermore, the lower boundary of the foundation slab as well as the lower part of the pile shaft and the pile base are clearly imaged. The semi-circular artifacts at the source positions ("1" in Figure 5-24) are caused by the direct waves traveling from the source to the receivers. These arrivals have not been suppressed before the application of the migration scheme. The events parallel to the lower boundary of the foundation slab ("2" in Figure 5-24) are generated by multiple reflections from the lower boundary in the synthetic data. The upper part of the pile shaft is not well visible in the image.

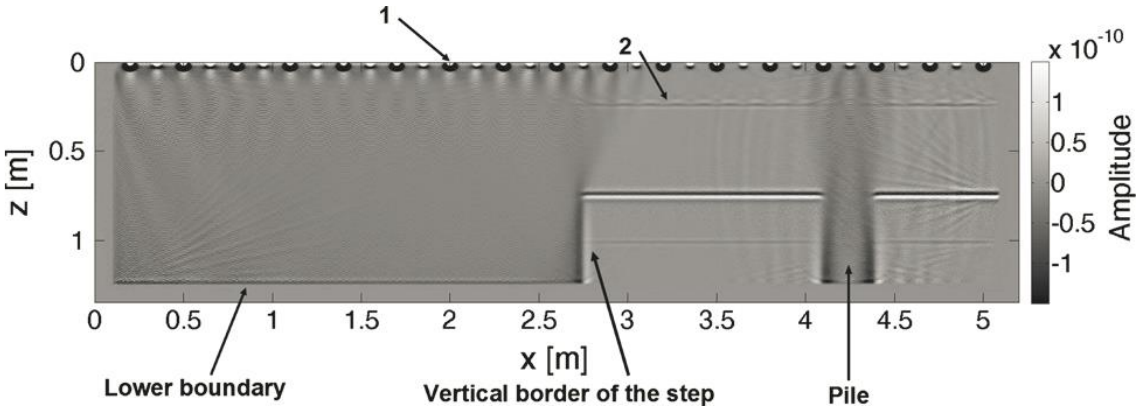

Figure 5-24: RTM image obtained with optimized migration parameters for the synthetic data set. 1: semi-circular artifacts caused by the direct waves, 2: artifacts generated by multiple reflections from the lower boundary in the synthetic data set.

The use of the two-way wave equation produces artifacts in the reconstructed images. These events are usually considered noise and exist due to the correlation of waves which are not accounted for in the cross-correlation imaging condition (Díaz & Sava, 2016). In the left part of the migration result and at the pile head these artifacts are clearly visible (dark shade). The reason is, that in these areas the position of the lower boundary of the concrete layer in the models used for RTM matches the real depth. Thus, the simulated source and receiver wavefields have the same propagation paths along which the cross-correlation does nor vanish.

5.4.4.3 Migration results: Kirchhoff migration

The first step of Kirchhoff migration comprises the calculation of the travel times from the source and all receivers to the image points. For all Kirchhoff migration results presented in this paper we used a homogeneous velocity model with a grid spacing of 0.001m. Furthermore, we performed true-amplitude stacking of the migrated shot sections. The result in Figure 5-25 was calculated with the same synthetic data as used in Section 5.4.4.2. For the homogeneous velocity model, we chose the true shear wave velocity of c_s = 2750 m·s^{-1}. The source and receiver positions corresponded to the parameters listed in Table 5-3. All reflectors except the vertical interfaces are imaged perfectly. The result shows, compared to the RTM result (Figure 5-24), less artifacts particularly at the source positions and model boundaries. However, the amplitude of the lower boundary of the slab decreases towards the vertical boundaries and arc-like artifacts appear ("1" in Figure 5-25). These events result from the smearing of the wavefield along the corresponding two-way travel time isochrones although only small parts of the isochrones contribute to the image of the reflector. The migration algorithm itself does not consider multiple reflections. For that reason, the lower boundary of the slab is reproduced a second time at a depth of approximately 1.5 m ("2" in Figure 5-25).

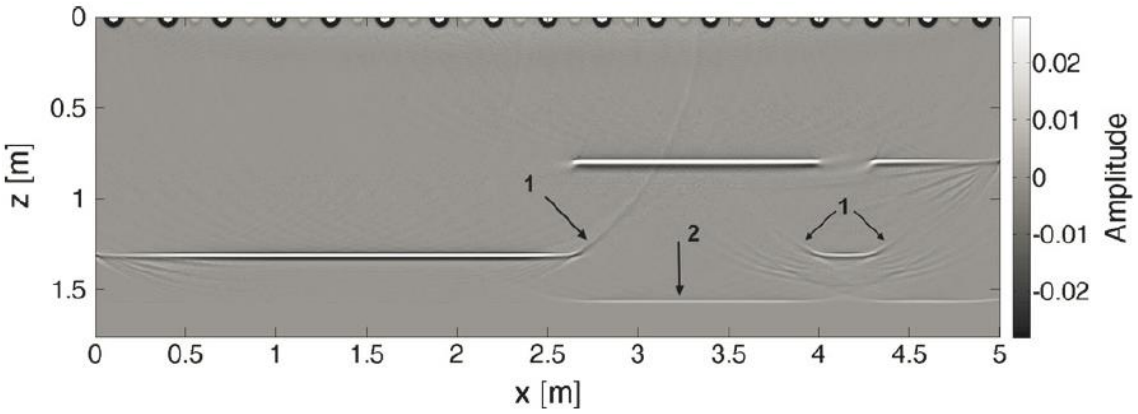

Figure 5-25: Result of Kirchhoff migration for the synthetic data set (1: arc-like artifacts, 2: artifact due to multiple reflections from the lower boundary in the synthetic data set).

5.4.5 Application to real data

5.4.5.1 Ultrasonic measurements

The main goal of this work was to test Kirchhoff migration and RTM with real ultrasonic data, which were recorded along one profile on the foundation slab (Figure 5-21). This profile corresponds to the profile that was used in 5.4.4. The distance from the southern boundary was 0.96 m. We used a multi-static arrangement to collect the ultrasonic echo data. Two ultrasonic transducer array were moved independently over the surface. Each transducer array (Figure 5-26) consists of 32 dry point piezoelectric contact transducers, which excite shear waves polarized perpendicularly to the profile direction. The

measurement frequency was set to 25 kHz. For moving the transducer arrays from one measuring point to the next one they were taken off from the concrete surface. During recording time, both were pressed against the surface of the slab without any couplant. An automatic scanner was used which moves the receiving transducer automatically (Figure 5-27). The range of the scanner is 1.2 m. For the synthetic RTM result in Figure 5-24 we used 242 receiver positions (placed along the entire line profile) for each source position. For the real measurements, it was not possible to scan the whole profile with the receiving transducer for each source position due to time and equipment restrictions. We decided to measure only the receiver positions lying in the positive profile direction. Furthermore, source-receiver offsets were limited to a maximum of 2.3 m due to the length of the scanner of 1.2 m (the scanner was moved just once). We used 32 source positions and a receiver spacing of 0.02 m. Before carrying out the measurements we applied RTM to synthetic data obtained with the parameters mentioned above (32 source positions and varying receiver positions). The result is shown in Figure 5-28. Compared to Figure 5-24 the imaging of the lower boundary of the slab, the vertical step and the pile head does not lose quality.

Figure 5-26: Ultrasonic transducer array consisting of 32 dry point contact transducers

Figure 5-27: (a): Scanner on the foundation slab moving the receiving transducer array (E) and (b): scanner with transmitting (S) and receiving (E) transducer arrays.

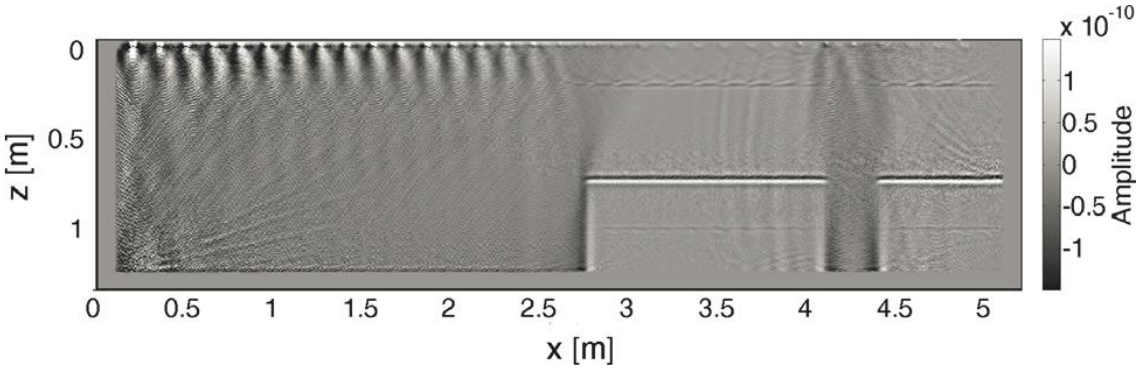

Figure 5-28: Result of RTM obtained by using the parameters of the measurement setup.

Figure 5-29 shows the recorded raw data for source position no. 8 at 1.15 m (distance from the eastern edge of the foundation slab). The direct wave (1) and the reflection at the lower boundary (2) of the foundation slab as well as a multiple reflection (3) at this boundary are visible. Furthermore, the reflection of the direct wave at the eastern (4) (E in Figure 5-21) and western (6) (W in Figure 5-21) upper edges of the foundation slab are shown. The apex of a reflection hyperbola is visible at 92 cm caused by a metal bracket inside the slab (5). Prior to migration we performed the following processing steps on the data: muting electronic crosstalk, time interpolation and zero-phase bandpass filtering (cut-off frequencies: 8 kHz/100 kHz). Significant and strong reflections from the southern (lateral) boundary of the slab are not visible in the data of all shots since the radiation pattern of the shear wave is mostly focused vertically downwards (Figure 5-30). Every single point contact transducer of the 32 shear wave transducers (Figure 5-26) produces lateral (in direction perpendicular to the line profile) p-waves, which may be reflected at the southern boundary and thus may be visible in the measured data.

However, the wavefields of the 32-point contact transducers interfere mostly destructively in the direction perpendicular to the profile due to phase shifts. Latter form because of the distances between the 32-point contact transducers. Considering the spacing between the single point contact transducers as well as the measurement frequency of 25 kHz we get no perfect destructive interference, but the wavefields still overlap destructively (for perfect destructive interference the distance between the point contact transducers should be one-half wavelength).

In the vertical direction, the wavefields of all 32 transducers interfere constructively as the signals of all transducers are in phase. In the vertical direction, the situation is somewhat in between, but signals are stronger than laterally as the size of the array is smaller in this direction resulting in less destructive interference.

In earlier investigations, the radiation pattern of the arrays was determined by evaluating measurement data acquired on four half-sphere specimens of self-compacting concrete (Figure 5-30) with a grain size of 4 mm. The diameters of the specimens ranged from 200 mm to 650 mm. Measurement frequency was set to 50 kHz (the center frequency of the point contact transducers). Theoretical details as well as information concerning the measurement setup were published in Maack (2012) and Spies et al. (2012). Compared to Figure 5-30 a less directional radiation pattern is expected at 25 kHz. Future work will include the determination of the radiation pattern at 25 kHz.

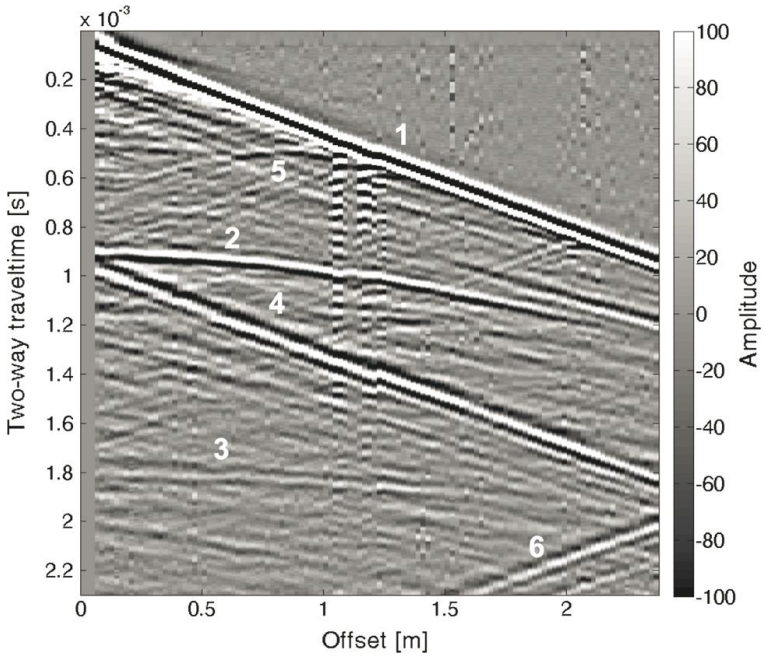

Figure 5-29: Ultrasonic-echo raw data for source position no. 8 at 1.15m (1: direct wave, 2: reflection at the lower boundary, 3: multiple reflection at the lower boundary, 4: reflection of the direct wave at the eastern upper edge, 5: reflection hyperbola caused by a metal bracket, 6: reflection of the direct wave at the western upper edge).

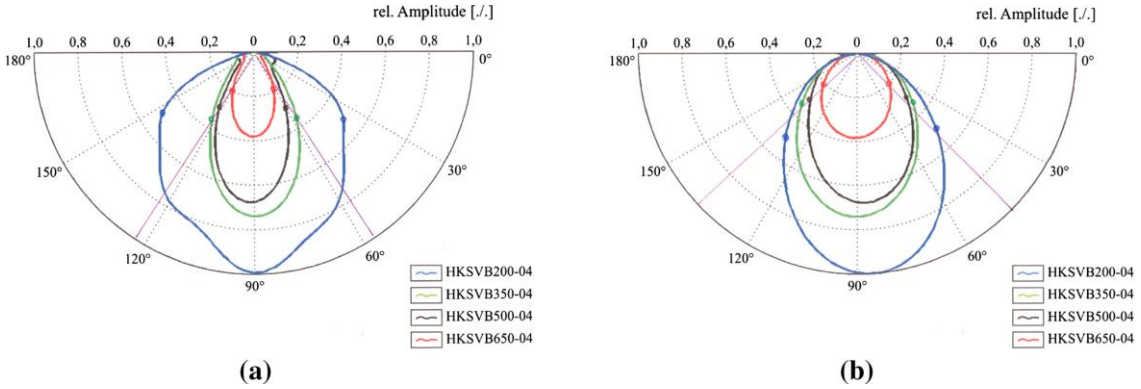

Figure 5-30: Radiation pattern of the shear wave transducers in polar diagrams at 50 kHz. (a): Radiation pattern in the plane parallel to the measurement direction and (b): Perpendicular to the measurement direction. HKSVB200-04 to HKSVB650-04 represent the four concrete specimens used.

5.4.5.2 Migration results: Reverse Time Migration

The structure of the velocity and density model which we used for RTM is shown in Figure 5-23. For the reinforced concrete, we chose a shear wave velocity of 2740 m·s^{-1}, based on a preliminary velocity analysis. The other migration parameters are summarized in Table 5-4. The recording time was 0.0017 s.

In the resulting RTM image, the lower boundary of the foundation slab is reproduced at the correct depth, showing a low amplitude at the model boundaries (Figure 5-31). The structure of the lower boundary shows some roughness and some dip near the vertical step. The pile head (gap in the lower boundary reflection) is visible at the correct position. The position of the step is shifted by about 0.1 m to the right. The pile shaft and pile base are missing. At x = 2.1 m and z = 0.3 m a circular reflector is reconstructed, which can be assigned to a metal bracket (Figure 5-32). Figure 5-33 shows the RTM image after stacking the images obtained from only shot points no. 27 to 32. The lower boundary of the slab is now imaged clearly with a higher amplitude and a small depth offset. Furthermore, a phase

reversal can be recognized, which is possibly caused by debonding in this area. The stacking of the images of shot points no. 7 to 15 only illustrates clearly that the vertical edge of the step is reproduced (Figure 5-34). In a next step, we carried out a crude 3D/2D-correction of amplitude and phase in addition to bandpass filtering, automatic gain control (AGC) and trace normalization because our RTM and Kirchhoff migration algorithms are 2D implementations and our data originate from a 3D source and a 3D medium. Therefore, as a first step, we multiplied the data by $\sqrt{t}$ [8] and the second step included a convolution with $\sqrt{1/t}$ (Crase et al., 2012). The lower boundary of the slab is now more clearly visible right next to the vertical step ("1" in) in comparison to the result in Figure 5-31. Using the x^2-t^2-method we determined an average shear wave velocity of the reinforced concrete of 2811 m·s^{-1} and an approximate depth of the lower boundary of the slab of 1.2132 m and 0.7269 m. This led to the conclusion that most of the energy of the wavefield was reflected at the lower boundary of the reinforced concrete layer rather than at the lower boundary of the lean concrete layer. The RTM image calculated with the average shear wave velocity of 2811 m·s^{-1} shows stronger artifacts on the left side of the image, caused by the effects described in Sect. 5.4.4.2 (Figure 5-36). Furthermore, the lower boundary of the slab on the left side of the pile head was reproduced more precisely compared to the result in Figure 5-35 due to the usage of a more accurate migration velocity.

Table 5-4: Parameters for RTM

Parameter	value
Model size	5200 × 1350 grid points
Distance between grid points	0.001 m
Frequency of the Ricker wavelet	25 kHz
Time step dt	1 ·10^{-7} s
Number of sources	32
Number of receivers	Varies
Distance between sources	0.15 m
Distance between receivers	0.02 m
Source position no. 1	0.02 m
Receiver position no. 1	0.031 m
Recording time	0.0017 s
Velocity—RTM	c_{sc} = 2740 m·s^{-1}, c_{ss} = 300 m·s^{-1}
Density—RTM	ρ_c = 2400 kg·m^{-3}, ρ_s = 1800 kg·m^{-3}
Thickness of concrete	*1.25 m*

v_{sc}: shear wave velocity of the concrete layer, v_{ss}: shear wave velocity of the sand soil layer, ρ_c: density of the concrete layer, ρ_s: density of the sand soil layer

[8] Geometric dispersion should be formally compensated by scaling with the square root of the traveling distance. As constant velocity is assumed in the concrete, scaling by $\sqrt{t}$ gives the same result.

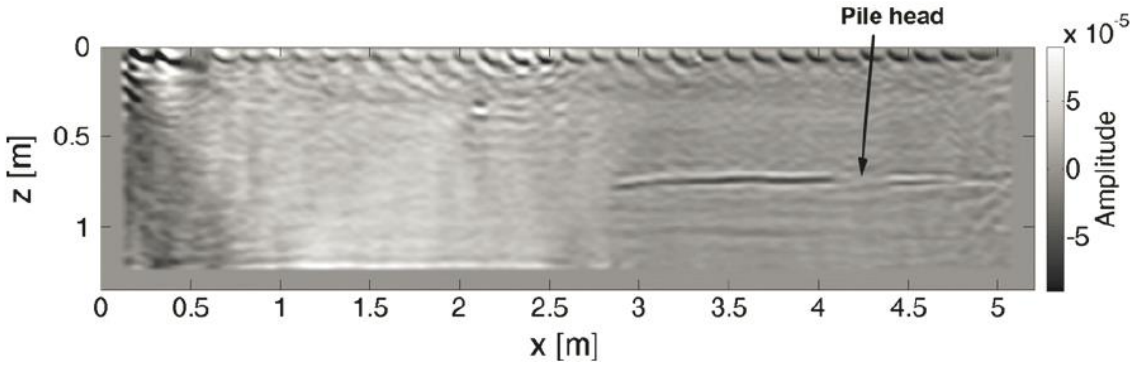

Figure 5-31: RTM image of the line profile.

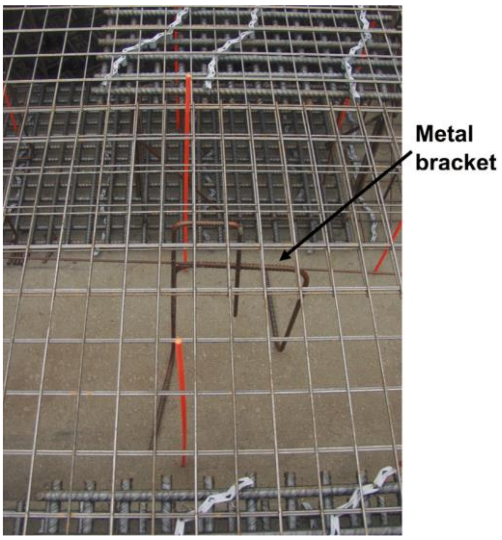

Figure 5-32: Metal bracket inside the foundation slab.

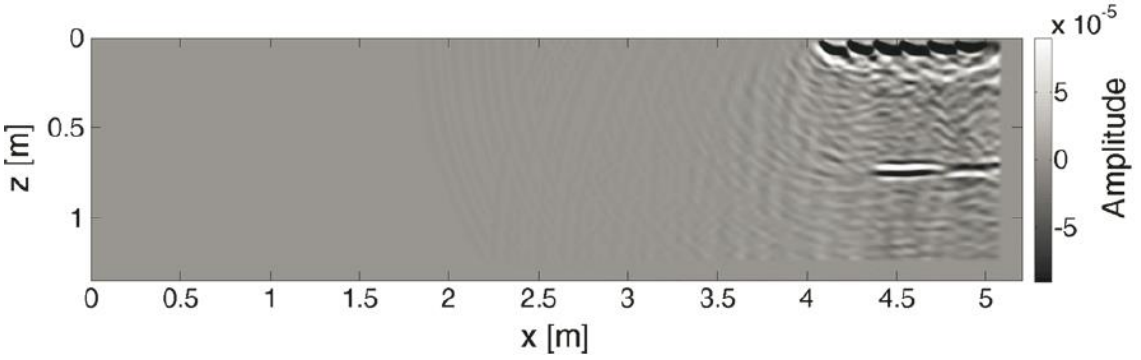

Figure 5-33: RTM image after stacking the images obtained from shot points no. 27 to 32.

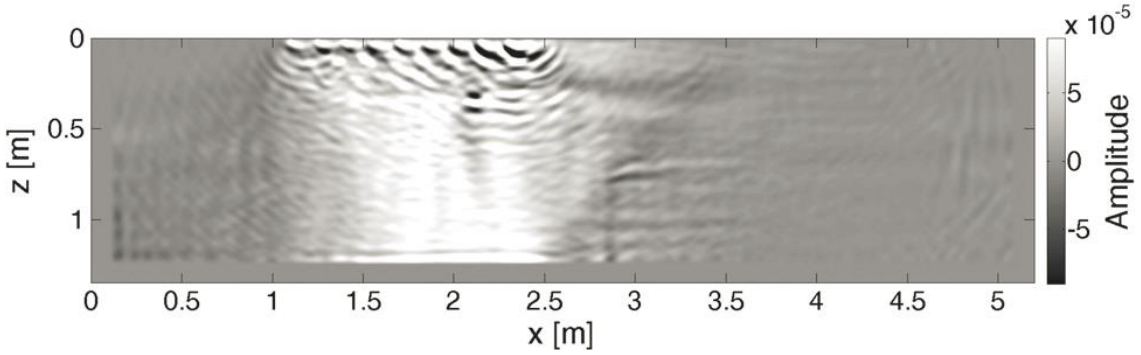

Figure 5-34: RTM image after stacking the images of the shot points no. 7 to 15.

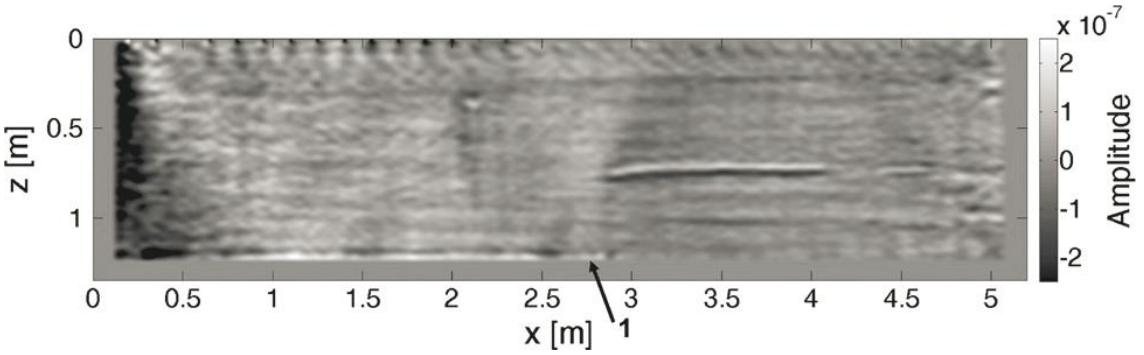

Figure 5-35: RTM image after applying a 3D/2D-correction (1: the lower boundary of the slab is more clearly visible in comparison to the result in Figure 5-31).

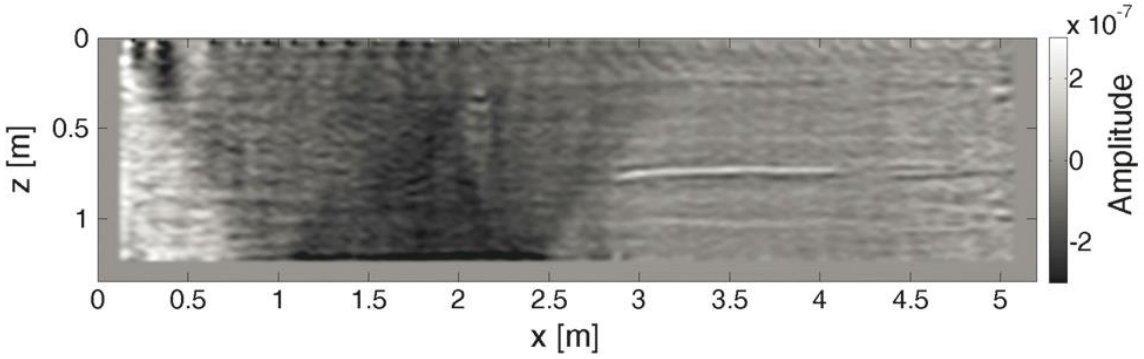

Figure 5-36: RTM image using the calculated average shear wave velocity of 2811 m·s^{-1}.

5.4.5.3 Migration Results: Kirchhoff Migration

The Kirchhoff migration results shown in Figure 5-37, Figure 5-38, Figure 5-39 and Figure 5-40 were calculated using a migration velocity of 2740 m·s^{-1} and the time interpolated measurement data. The recording time was 1.7 ms. For the result displayed in Figure 5-37 we applied a bandpass filter (cut-off frequencies: 8 kHz/100 kHz) to the data. Furthermore, we eliminated the direct waves and the reflections of the direct waves at the lateral boundaries of the foundation slab, if a clear separation of other relevant events was possible.

The lower boundary of the slab, the pile head and the metal bracket are clearly visible. Similar as in the RTM results the horizontal shift of the position of the step, the dip of the lower boundary of the slab near the vertical step as well as the roughness in the structure of the lower boundary were reconstructed. The cause for the event parallel to the lower boundary of the slab at a depth of z = 1 m is not clear yet ("1" in Figure 5-37). It is imaged in the RTM result as well but with a lower amplitude (Figure 5-31). A reflector caused by multiple reflections in the data can be observed at a depth of z = 1.43 m ("2" in Figure 5-37).

Analogous to the RTM results shown in Figure 5-33 and Figure 5-34 we stacked the migration images of shot points no. 27 to 32 and 7 to 15 only (Figure 5-38 and Figure 5-39). Compared to the respective RTM image (Figure 5-34) the vertical border of the step could not be imaged by using Kirchhoff migration. Furthermore, compared to Figure 5-33 it was not possible to reconstruct the lower boundary of the slab till the right model boundary.

For the image in Figure 5-40 we additionally applied AGC, trace normalization and 3D/2D-correction of amplitude and phase to the data. Now, like the RTM results, the lower boundary of the slab is imaged better near the vertical step ("1" in Figure 5-31).

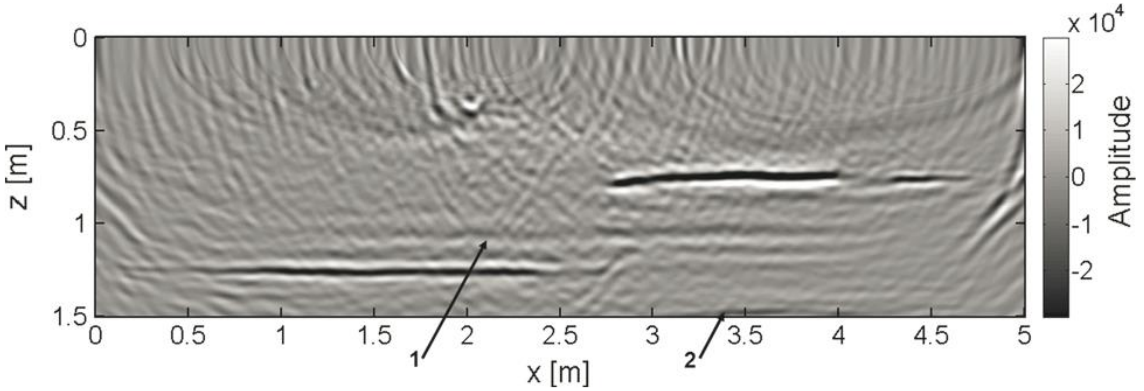

Figure 5-37: Result of Kirchhoff migration after applying a bandpass filter and eliminating the direct waves in the measurement data (1: unknown event, 2: reflector caused by multiple reflections).

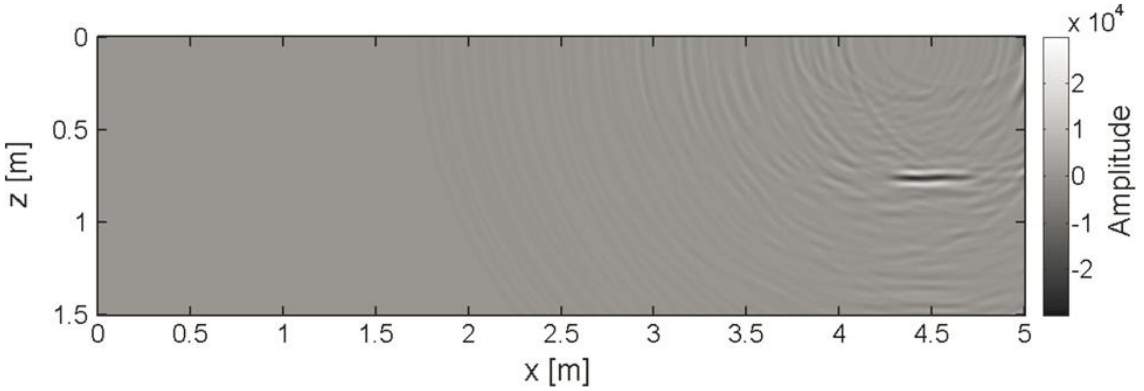

Figure 5-38: Result of Kirchhoff migration after stacking the images obtained from shots no. 27 to 32.

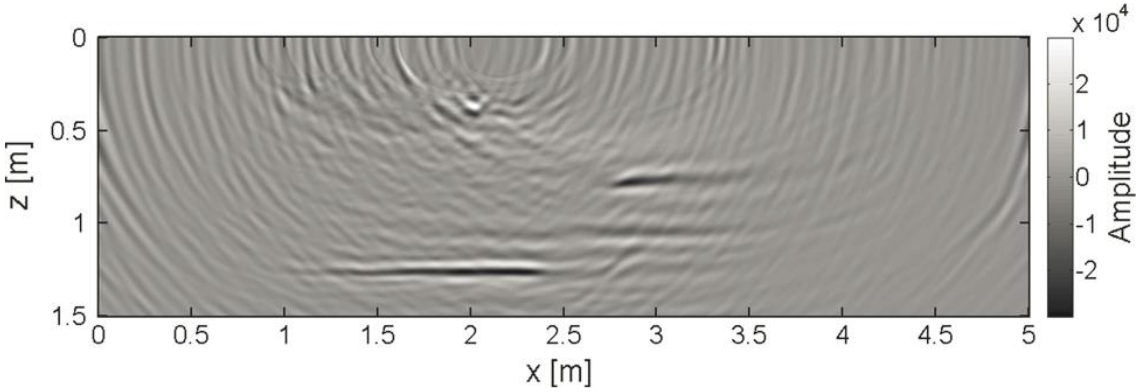

Figure 5-39: Result of Kirchhoff migration after stacking the images obtained from shots no. 7 to 15.

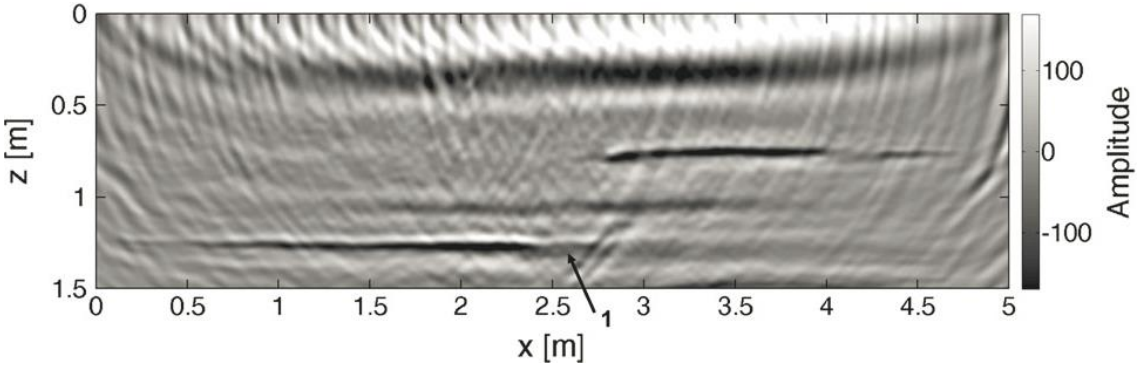

Figure 5-40: Result of Kirchhoff migration after applying AGC, trace normalization and 3D/2D-correction to the data (1: lower boundary of the slab imaged better in comparison to the result in Fig. 21).

5.4.5.4 Migration results: SAFT

Figure 5-41 shows the image obtained by the homogeneous 3D-SAFT reconstruction of the line profile. The InterSAFT software (Mayer & Cinta, 2012) was used in this example to reconstruct the multi-offset data. We chose a migration velocity of c = 2740 $m \cdot s^{-1}$ and the raw data processed with a band pass filter (cut-off frequencies: 8 kHz to 100 kHz). Moreover, we eliminated the direct waves and their reflections at the boundaries of the slab. As expected, the image obtained with SAFT is almost identical to the result of Kirchhoff migration (Figure 5-37) but with less artifacts close to the surface. Furthermore, the amplitude of the lower boundary of the slab is slightly weaker.

Again, we stacked the reconstruction results of shot points no. 27 to 32 and 7 to 15 only to make a comparison with the respective RTM and Kirchhoff migration results. The results are shown in Figure 5-42 and Figure 5-43. As in Kirchhoff migration no vertical reflector could be imaged and the reconstruction of the lower boundary of the slab close to the right model boundary was not successful.

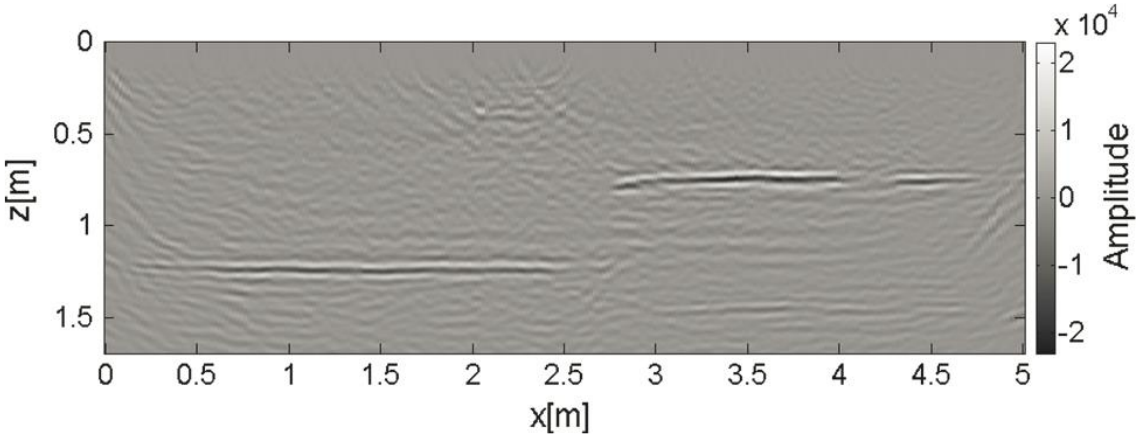

Figure 5-41: SAFT-reconstruction after applying a bandpass filter and eliminating the direct waves in the measurement data.

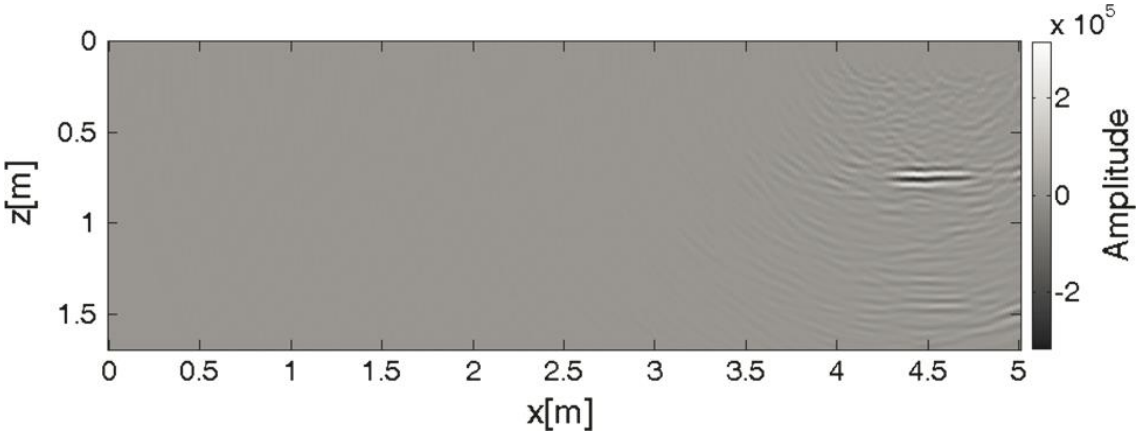

Figure 5-42: SAFT-reconstruction after stacking the images obtained from shots no. 27 to 32.

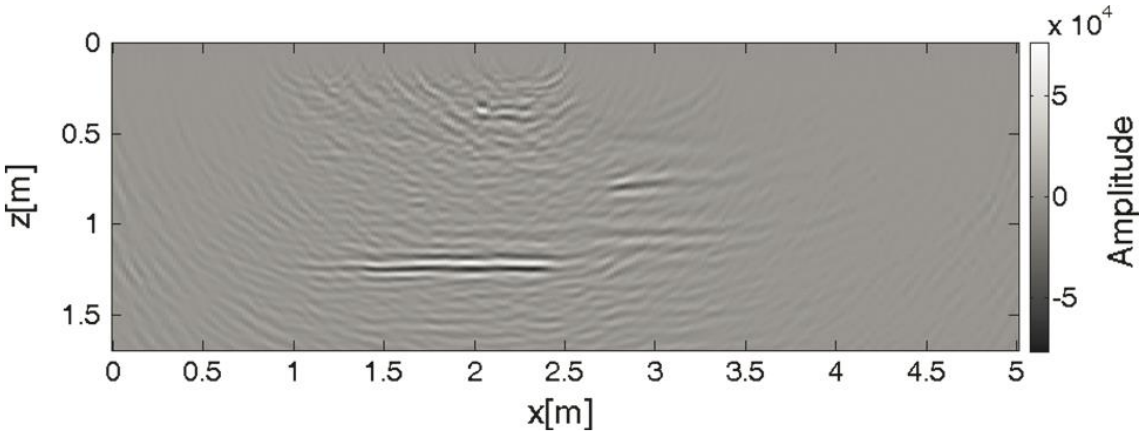

Figure 5-43: SAFT-reconstruction after stacking the images obtained from shots no. 7 to 15.

5.4.6 Discussion

The comparison between RTM, Kirchhoff migration and SAFT shows a significant improvement in imaging the geometry of the foundation slab by RTM. The reconstruction results of Kirchhoff migration and SAFT are similar because their algorithms are closely related to each other. By using Kirchhoff migration and SAFT no vertical features inside the slab could be reconstructed. The Kirchhoff migration algorithm we applied is based on the approximative integral solution of the wave equation (5-3) and normally only considers the shortest wave paths between sources and receivers. Thus, for a subsurface with strong velocity contrasts and the associated changes of the wave propagation paths (multi-pathing), no optimal migration result can be achieved (Geoltrain & Brac, 1993). The cause for the irreproducibility of the vertical interfaces might therefore be, that reflections with longer travel times than the calculated ones, are not imaged in the model domain. However, RTM is based on a simulation of the wavefield by directly solving the wave equation and is thus more accurate. It enables the imaging of steep reflectors with inclinations >70°, even in media with strong velocity variations, because all wave types and multi-pathing are considered.

All migration images show a horizontal displacement of the vertical step of about 0.1 m compared to the construction drawings. Since the pile head was reproduced at the expected position, the displacement of the step is rather an error in the construction drawings than an imaging artifact. The imaging of the pile geometry was not fully successful, because the measured data show noisy signals from the piles due to the reinforcement, edge effects, multiple reflections at the pile shaft, 3D effects, and the attenuation of the waves in concrete. The roughness in the structure of the lower boundary of the slab may be caused by the migration algorithm or has been formed during the construction of the slab. The latter might as well be the reason for the dip of the lower boundary of the slab close to the vertical step. Furthermore, material inhomogeneities might produce the roughness as well as the dip.

It must be noted that for the RTM algorithm the use of transducer arrays is not yet implemented. The 2D RTM code currently only allows point sources. The simulation of transducer arrays consisting of more than one-point source is not possible at that moment. Therefore, the migration algorithm does not calculate the shot and receiver wavefields fully correctly. Future work includes the implementation of the possibility to use arrays consisting of various point sources, as well as two dimensional arrays. The quality of the resolution of the lower boundary of the slab does not appear to depend on the amount of the lower reinforcement. Furthermore, the application of the 3D/2D correction did improve the image quality slightly in this case.

5.4.7 Conclusions and outlook

We used synthetic and measured data sets to evaluate the applicability of RTM and Kirchhoff migration to image ultrasonic echo data collected on a reinforced concrete foundation slab. The tests yielded promising results and showed that especially RTM is a step forward for the ultrasonic echo technique used in nondestructive testing.

The imaging of the location and structure of the lower boundary of the slab could be improved with RTM compared to conventional imaging techniques (SAFT). By using RTM vertical borders could be imaged clearly and more features could be found (Figure 5-33, Figure 5-34). By optimizing the measurement equipment, a higher amplitude resolution should be achievable to improve the reconstruction of the pile geometry. A different scanner allowing a larger aperture should be utilized for realizing a better resolution of the features inside the slab as well as reduction of artifacts and measurement uncertainties. RTM artifacts must be analyzed and eliminated. For this task alternatives to the cross-correlation imaging condition as well as pre-imaging- or post-imaging filtering techniques may be used. In addition, the algorithm should be expanded to three dimensions and the full elastic wave equation. Another topic to be addressed is to how to account for the size of the ultrasonic arrays. Finally, experiments such as the one detailed in this paper may be of interest to evaluate seismic migration methods on analogue models.

5.5 Further developments

One of the main drawbacks in the application of RTM are migration artifacts, some of them limited to area close to the sources, others causing offsets or ripples all over the area of interest. Two approaches are followed to avoid or at least to reduce these artifacts. First, alternatives to the currently used imaging condition (e. g. Chattopadhyay & McMechan, 2008 or Liu et al., 2011) might help. This approach is currently explored for concrete application by two students supervised by the author of this thesis. Second, the effect of the artifact might be diminished by filtering and image processing techniques. This was successfully tested in a master thesis by Sarah Sieber (then RWTH Aachen/BAM) in 2015 and reported by us recently (Grohmann et al., 2017). The latter shows also the current state of the art in RTM on concrete.

The potential for full scale application is currently investigated in several case studies at BAM. For example, Markus König (then BAM/RWTH Aachen) showed in his master thesis 2016, that hidden cracks can be detected and imaged by RTM.

Using RTM for ultrasonic echo imaging is not the end of the story of application of seismic migration tools in NDT-CE. For example, Full Waveform Inversion (FWI) has despite its even higher computational costs a huge potential to solve some complex testing problems. So far, it has been applied e g. to evaluate ultrasonic surface wave measurements (e. g. Koehn et al., 2016) or to determine material properties from radar data (e. g. Kalgeropulos, 2012).

6 Structural monitoring by ultrasound

6.1 General Remarks

Concrete is the material most produced by mankind. It is considered to be strong, resistive and durable. Some early concrete structures as the cupola of the Roman Pantheon have been standing up since almost 2000 years. However, under certain conditions (hostile environments, adverse load conditions) concrete constructions require attention. For example, the apparently ever-increasing traffic load (number and individual load of trucks) on bridges may lead to deterioration much earlier than expected at the time of design. Currently, inspections are still based on visual methods mainly, but sophisticated nondestructive methods are used more and more often. The use of bridge instrumentation increases rapidly (Karbhari et al. 2009). But so far monitoring is limited to local sensors (e. g. strain gauges), which are probing just their close vicinity, or global methods as modal analysis. There is a gap in between. A method which would look at a certain critical volume of concrete with a very limited number of sensors would be of great value.

Ultrasonic transducers with frequencies from 25 kHz to 400 kHz have been used for testing concrete since decades. They are used in the lab on samples (and sometimes on site) in transmission mode to measure elastic properties and to assess degradation (DGZfP, 2014). New point contact transducers have revolutionized the use of echo techniques for thickness measurements and structural imaging. Even the detection of voids in tendon ducts seems to be possible (Krause et al., 2011). All transducers used in practice so far are for surface mounting. For monitoring this approach shows three strong disadvantages. First, the need for constant coupling, which is hard to realize on the surface in practice. Second, the high influence of surface and external effects (temperature and others) leads to unwanted effects on the measurements. Third, in practical field applications the transducers are prone to accidents or vandalism. Therefore, we started to develop a novel transducer which can be permanently embedded in concrete (section 4.4, Niederleithinger et al., 2015a).

In combination with algorithms from seismology as Coda Wave Interferometry (CWI), which allow the detection of very subtle changes from repeated active or passive experiments (section 6.2), ultrasonic monitoring opens a new field for the supervision of concrete structures. Sensors don't have to be exactly at the point of change or damage. Sparse networks can monitor large volumes. Imaging extensions of CWI are on the verge of practical application (section 6.4).

In addition, experiments on well-defined concrete models can be used as a scale model to evaluate new geophysical (or other techniques). An example is shown in section 6.5, where a simple experiment using a concrete cube with three embedded sensors is used to check a novel approach for time reversal techniques. The results can be used to detect and characterize acoustic sources within the earth, the ocean or constructions (e.g. acoustic emission monitoring).

6.2 Coda Wave Interferometry

6.2.1 Definition and algorithm

Coda Wave Interferometry (CWI) was introduced more than two decades ago to detect small velocity changes in the earth crust due to stress, seismic effects, mining influence or seasonal variations (e.g. Snieder et al., 2002; Sens- Schönfelder & Wegler, 2006; Grêt et al., 2006a). Recently CWI was used by several researchers to detect small changes in concrete microstructure (Larose & Hall, 2009; Stähler et al., 2011; Niederleithinger et al., 2010; Zhang et al., 2011; Larose et al., 2006; Larose et al., 2010; Zhang et al., 2012; Larose et al., 2015). A review is given in Planès & Larose (2009).

In seismics, the coda is defined as the long-lasting wave train after a seismic event. The coda contains a notable amount of energy, but has lower amplitudes than the event itself (Figure 6-1). The waves included in the coda are (at least partially) caused by multiple scattering and have traveled much longer distances than direct waves. As a result, changes in the material causing small velocity changes, which may have no visible effect on the arrival times of the direct waves (first arrivals), result in much longer time shifts in the coda (Figure 6-2, Figure 6-3). The coda contains information from all spatial directions, components and wave types (Figure 4-13). However, it is normally considered, that the main information is related to shear waves.

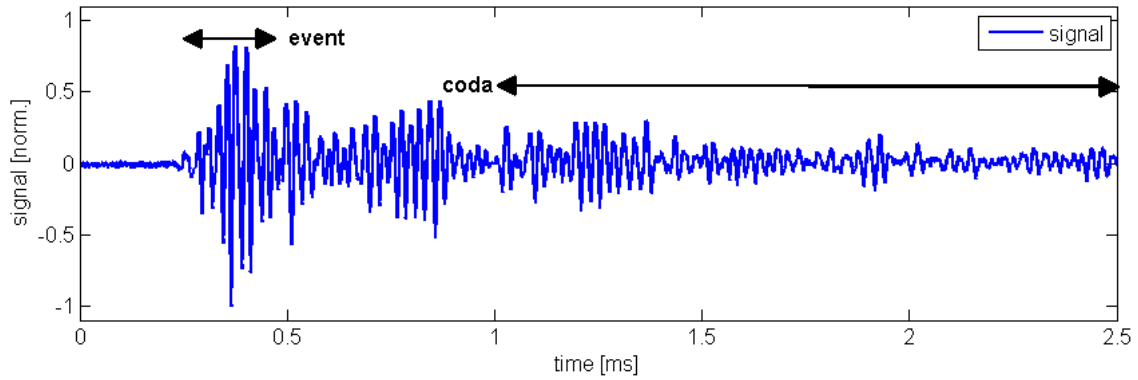

Figure 6-1: Ultrasonic time series from an experiment on a concrete prism, containing event and coda.

Several methods have been developed to evaluate the phase shift of coda waves between two time series (h_0, h_i) and the corresponding relative velocity changes. In this research the "stretching" technique (Grêt et al., 2006b; Larose & Hall, 2009) has been used. One of the time series (h_i) is stretched (or compressed) by an assumed small relative velocity change ν until an optimum correlation of both time series in a time interval [0, T] is reached:

$$CC(\nu) = \frac{\int_0^T h_i\big(t \cdot (1-\nu)\big) \cdot h_0(t)\, dt}{\sqrt{\int_0^T h_i^2\big(t \cdot (1-\nu)\big)\, dt \cdot \int_0^T h_0^2(t)\, dt}} \qquad (6\text{-}1)$$

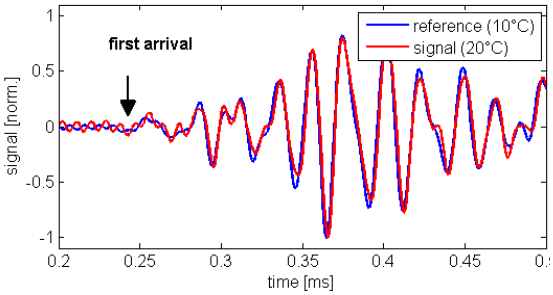

Figure 6-2: Early portion of time series. No significant time shift.

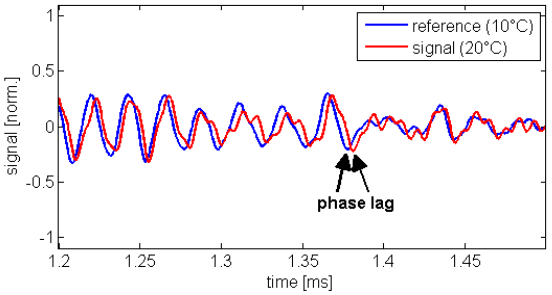

Figure 6-3: Late portion of time series. Significant time shift.

The relative velocity plotted in most of the following figures is calculated by $c/c_{ref} = (1+\nu)$. In the following sections, the data measured at the beginning of each experiment were used as reference. Most measurements have been repeated several times to get a measure on the standard deviation of the results. Figure 6-4 shows the correlation curves for six measurements at a specific temperature from the experiment described in section 6.2.2, evaluated by equation (6-1) using a relative velocity change interval of $1 \cdot 10^{-5}$. The graphs are hard to discriminate and have their respective maximum at the very same point. Thus, it is believed to have a resolution in the same order of magnitude as achieved by Larose & Hall (2009).

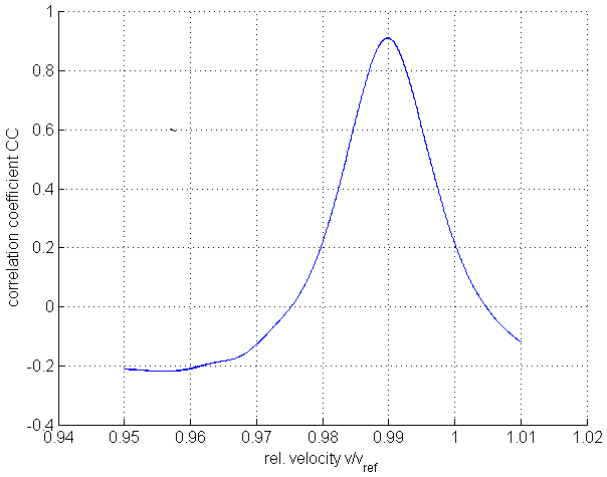

Figure 6-4: Correlation between six ultrasonic time series measured at 25 °C, referenced to 0 °C.

6.2.2 Example 1: Temperature influence on ultrasonic velocity in concrete[9]

The influence of temperature on the results of ultrasonic velocity in concrete is known, but so far ignored in standards for simple transmission time of flight measurements (BS EN 12504-4). The much more sensible CWI results on concrete structures have been shown to be significantly influenced by temperature (e.g. Larose et al, 2006; Zhang et al., 2012).

Several sets of laboratory experiments in a climate chamber at BAM. First, conventional surface mounted sensors were used, but slight inconsistencies in sensor placement led to significant errors (Niederleithinger & Wunderlich, 2012). A second set of experiments was carried out using three samples (ES1, ES2, ES3) made of the same concrete, with a size of 40 x 15 x 15 cm^3 (Figure 6-5, Figure 6-6). The samples have been equipped with two embedded ultrasonic transceivers (see section 4.4.2), here forced to work around 100 kHz.

[9] This section has been compiled from Niederleithinger & Wunderlich, 2012.

The samples were more than three months old at the beginning of the measurements. They were cooled to 0°C in the climate chamber at the beginning and then heated up to 50 °C in 5 K steps, following by cooling in the same manner. The temperature was kept at least 20 h to avoid gradients in the samples. After each temperature step, ultrasonic measurements were been performed for each sample in both configurations (MR11 and MR2, switching the sensors to work as transmitter/receiver) using standard US equipment (12-bit amplitude resolution, 1 MHz sample rate, 5000 samples, 144 stacks, 4 to 8 repetitions). The samples stayed in the climate chamber during the measurement.

Figure 6-5: Climate chamber with samples equipped with embedded ultrasonic sensors. Lower right: sensor before embedment.

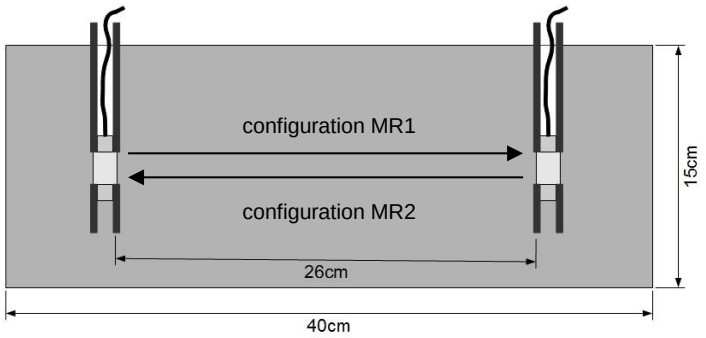

Figure 6-6; Cross-section of samples with embedded ultrasonic transceivers. The transceivers can be used as transmitter or receiver, resulting in two possible measurement configurations (MR1, MR2).

The acquired data were evaluated for all samples, configurations and repetitions using the procedure described above. The data for all temperature steps of each heating/cooling cycle are well correlated to the respective reference data (0 °C). The peak correlation values are shown in Figure 6-7. The number of temperature steps is different for both cycles as some measurements have been repeated. The decorrelation increases towards higher temperatures and recovers partially during cooling. Small anomalies are visible again around room temperature, still probably due to moisture issues of the climate chamber. Note that there is a significant remaining decorrelation after re-cooling in the first cycle, while the correlation almost recovers in the second one.

Figure 6-8 shows the evaluated velocity variation. In the first cycle, the velocity decreases during heating by almost 4 %. After cooling, there is a remaining velocity drop of about 1.3 %. Hysteresis was expected due to on-going hardening, but this would have resulted in a velocity increase. As we don't expect permanent damage due to the temperature variations imposed we think that the velocity drop is due to cracks generated by shrinking or similar effects. We must perform more experiments for verification. In the second cycle,

the heating curve almost matches the one of the first cycle (on a lower level), while during re-cooling we experience a smaller hysteresis (0.7 %) than in the first cycle. This correlates to the better "re-correlation" visible in Figure 6-7 and supports the idea of relating the hysteresis to early age change effect.

To demonstrate the independence of the results from a specific sensor or sample, the velocity variations in the first cycle are shown in Figure 6-9 for all three samples and both transceiver configurations. The results between configurations deviate max 0.1% for sample ES1 and ES3 and 0.25 % for ES2. This should be mainly due to incoherent noise events occurring in our measurement environment caused by other experiments and on-going repair works. The deviations between samples are in the same order of magnitude, which is satisfying taking the inhomogeneity of concrete into account.

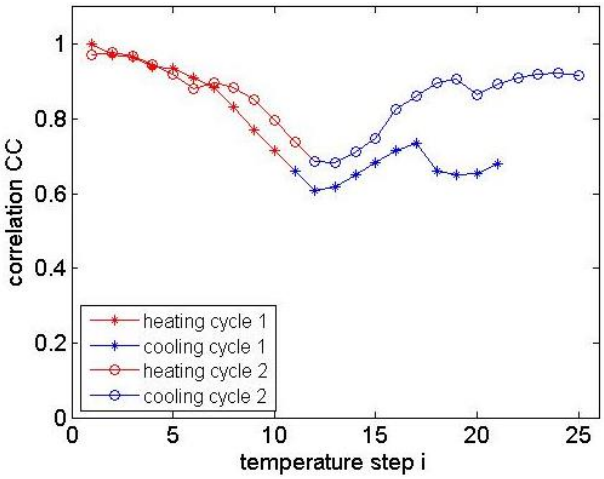

Figure 6-7: Correlation to reference trace (beginning of each cycle) for ultrasonic data acquired at each temperature step on sample ES1, configuration MR1. Some measurements have been repeated in second cycle (thus more steps).

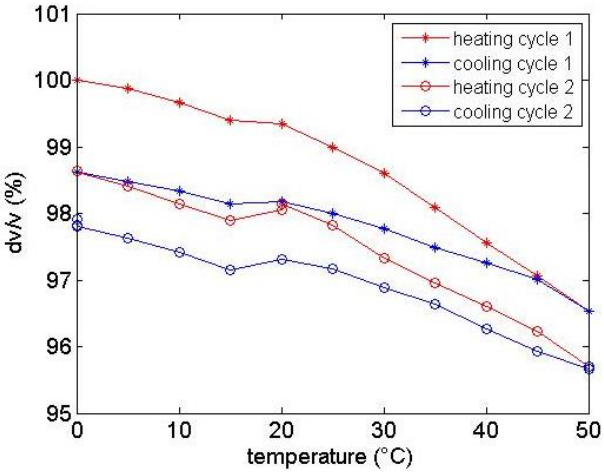

Figure 6-8: Velocity variation (percentage of reference value) for two temperature cycles on sample ES1, configuration MR1

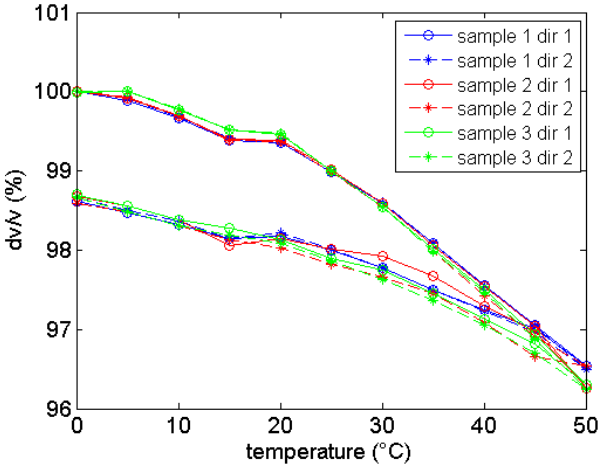

Figure 6-9: Velocity variation for first cycle for all samples and configurations

CWI proved a valuable and sensible tool to detect small velocity changes in concrete. It might serve in the future as a method to detect early signs of damage in monitoring applications. CWI requires an accurate repetition of the ultrasonic measurements. Sensor misplacement leads to errors, which might hide velocity changes below 0.5 % if the sensors are not mounted permanently. In practical application, the sensors should be embedded in the concrete as demonstrated in one of our experiments.

These results call for temperature and moisture monitoring in practical ultrasonic monitoring systems to avoid misinterpretation of velocity changes. Meanwhile, proposals for temperature compensation have been proposed by Zhang et al. (2013) for lab experiments and Salvermoser et al. (2015) for field data.

6.2.3 Example 2: Long-term dam monitoring[10]

The concrete dam at Eibenstock (Germany) serves as a reservoir for drinking water and is part of the local flood protection system. During construction in 1979, eight ultrasonic sources and four receivers (40 kHz center frequency) were been implemented to follow the hardening of the concrete. The system was operated using a simple oscilloscope until 1985. In 2011 the switch box was replaced. After this repair, it showed that all transducers were fully operational.

Figure 6-10: Concrete dam at Eibenstock, Saxony, Germany. Picture: Landestalsperrenverwaltung Sachsen.

[10] This section is compiled from Niederleithinger et al., 2015b

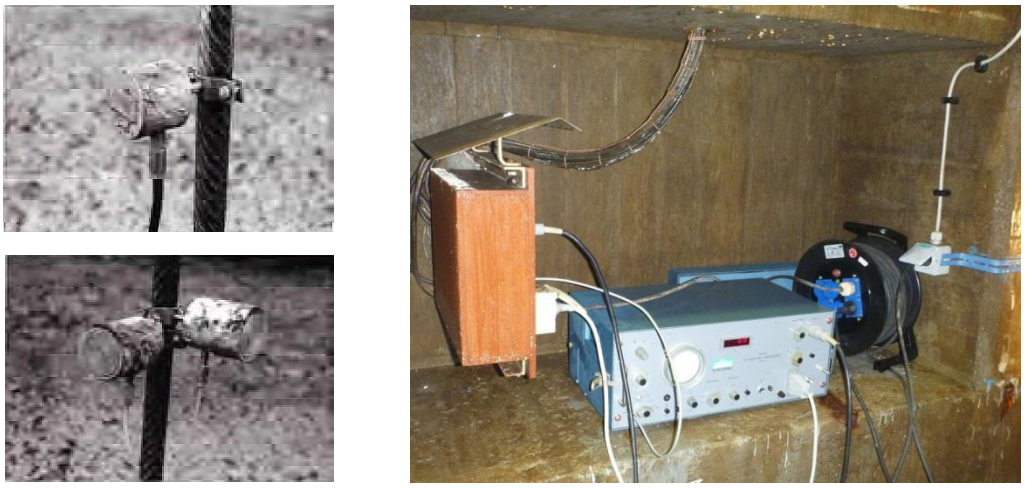

Figure 6-11: left top: Ultrasonic transmitter before concreting. Left bottom: dto., receivers (photos from installation report). Right: switch box and original oscilloscope from 1979. Picture: R. Krompholz, Geotron-Elektronik, Pirna.

In a first step, time of flight measurements were conducted with the original and state-of-the-art equipment supplied by Geotron-Elektronik (Rolf Krompholz, Pirna, Germany). The deviation was less than 1 %. As done for the original reports on concrete hardening, velocities for all transmitter-receiver combinations were measured and averaged. The result (p-waves only, as s-wave arrivals were seen just in a few transmitter-receiver combinations, and the old reports did not state which ones had been used for averaging) shows, that the wave speed has increased somewhat over almost 30 years, indicating an increase in compressive strength.

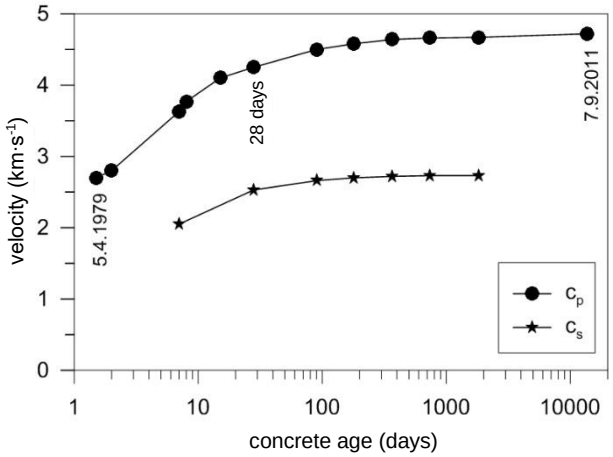

Figure 6-12: variation of velocity (time of flight) with concrete age at the Eibenstock dam. From Niederleithinger et al. (2015b).

For about two years (2011-2013) we have monitored the ultrasonic signals with an on average two-month intervals. The data were evaluated for time of flight velocity manually (for s-waves) or using the automated AIC-Picker (for p-waves) and for velocity changes by Coda Wave Interferometry. Temperature at the point of installation has remained almost constant as well as the water level in the reservoir. The results for s-waves (CWI contains mainly information on s-wave velocity) are shown in Figure 6-13. The measurements of September 2011 served as a reference. The velocity variation is generally very low. But the

conventional time of flight evaluation shows significantly more scatter and an offset against the reference measurement.

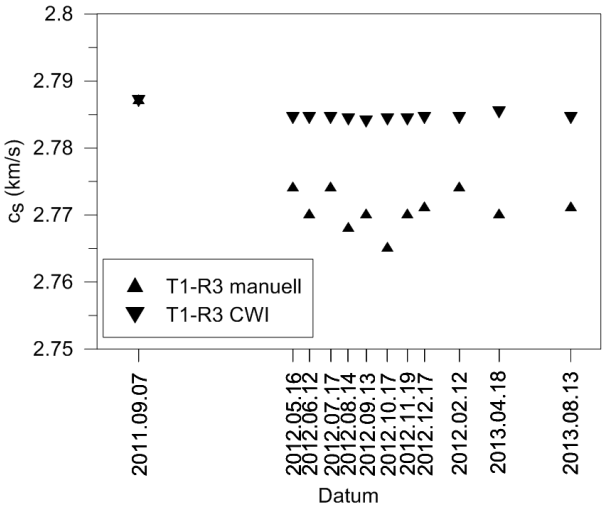

Figure 6-13: Velocity change (for s-waves) over time for a specific transmitter-receiver combination evaluated manually and by CWI. From Niederleithinger et al. (2015b).

These experiments showed, that embedded sensors can survive within concrete constructions for decades. Accurate and reproducible measurements have been made 34 years after construction. CWI has been used as a tool for evaluation velocity changes, which proved to be much more stable than conventional time of flight measurements.

6.2.4 Monitoring of a bridge load test.

To evaluate the feasibility of using embedded ultrasonic sensors for stress and degradation monitoring in real constructions, eight transducers (Niederleithinger et al., 2015a) were implemented in a bridge girder at a construction site in Poland (Figure 6-14, Figure 6-15). The project has been coordinated and supported by Polish monitoring specialists (Neostrain. S.A., Krakow).

Figure 6-14: Bridge construction site in Poland.

Figure 6-15: Ultrasonic transducer before concreting

Load tests were performed in 2014 and 2015 by positioning between two and six 30 t-trucks at various positions of the bridge (Figure 6-16). Even the highest load applied is far below the service load of the bridge. The main goal was to show that the actual bridge deformation is equal to or lower than the calculated values (which was accomplished).

Ultrasonic measurements were performed using several transmitter-receiver combinations during the load tests. The velocity changes were smaller than the resolution limit of CWI. But the correlation coefficient determined by CWI showed clear indications of changes. Figure 6-17 shows the results for a specific transmitter-receiver configuration at various

stages of the load test. As expected, the effect was most significant when the trucks have been placed directly above the instrumented girder (stage S4L in Figure 6-17), still clearly visible when on the same span, but opposite girder (S4P) or same girder, but next span (S3P), and still recognizable when on the opposite girder on the next span. When the trucks where above the abutment (P1), there was no measurable effect.

Figure 6-16: Load test.

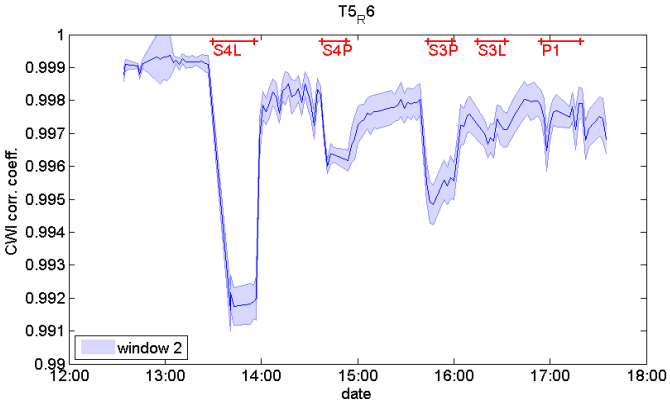

Figure 6-17:CWI correlation coefficient for transmitter 5/receiver 6 with trucks at various positions of the bridge. Shaded area: standard deviation from repeated measurements.

This experiment showed, that we can detect stress effects caused by load on real bridges by CWI. But with the current state of technology, the effects are close to the limit of detection.

6.3 Bridge monitoring[11]

6.3.1 Introduction

Among the various method of nondestructive evaluation and testing (NDT) of civil engineering structures wave methods play an extraordinary role. Electromagnetic as well as sonic wave methods are fast and usually provide good spatial resolution for the characterization of the structure (McCann & Forde, 2001). Seismic methods include the investigation of eigenmodes for damage characterization (Van Den Abeele & De Visscher, 2000), the use of ultrasonic reverberations (Impact-echo) to determine the width of a concrete layer (Sansalone & Carino, 1988), sonic/seismic tomography, and reflection methods. These methods are good candidates for further developments to fulfill the increasing demand for long term monitoring of civil engineering structures. The modified focus from the spatial distribution of material parameters towards temporal changes opens new possibilities for their application.

It has been demonstrated for sonic methods that it is possible to monitor temporal changes with a precision far superior to the accuracy of repeated structural investigations if spatial resolution is not of primary interest (Larose & Hall, 2009; Larose et al., 2006; Grêt et al., 2006a; Shokouhi et al., 2010). This is especially true for target media with strong internal

[11] This section is an edited version of Stähler et al., 2012. The authors of this study were supported by construction company Arlt and the civil engineering enterprise Stähler+Knoppik. Udo Müller, Stephan Pirskawetz and Thomas-Rudolf Nowak provided valuable assistance with the measurements. Michael Korn and Martin Käser provided insights into numerical aspects. The project was partially funded by the IHK Leipzig.

heterogeneity such as concrete, where the strong scattering at high frequencies would render transmission/reflection and tomographic methods based on ballistic (direct, non-scattered) waves impossible (Anugonda et al., 2001; Saint-Pierre et al., 2007). To turn this apparent limitation of strong scattering into an advantage Coda Wave Interferometry makes use of scattered waves with long traveltimes in later part of the seismic signal (coda). Since waves in this part of the signal propagate through a perturbed region several times, the effects of minute changes in the medium accumulate to notable alteration of the acoustic waveforms. Since waves with different paths are superposed in the coda, spatial information about the changes is reduced compared to ballistic waves. However, the sensitivity to detect these changes at all is greatly increased (Snieder, 2006).

So far, the monitoring applications were mostly restricted to laboratory environments. In one study, which was done at the slab of a parking deck, a diurnal velocity variation could be shown and qualitatively explained by temperature variations, without knowing the actual stresses (Larose et al., 2006). In this study, we present an experiment that takes the methodology to an engineering structure where a detailed stress model is available for comparison with wave field changes. We monitor stress variations in a concrete bridge with seismic waves of frequencies around 1 kHz.

We first introduce the acoustoelastic effect as the basis of the relation between stress changes and variation of the seismic velocity. Since the expected velocity variations are too weak to be measured by the time of flight of ballistic waves we explain our approach to use scattered waves in section 6.3.3. Before the experiment at the bridge is presented in section 6.3.5 we describe in section 6.3.4 the laboratory measurements that were conducted to obtain the relevant parameters for the bridge's concrete. Finally, we discuss the results and give a summary in sections 6.3.6 and 6.3.7.

6.3.2 Stress-velocity effects in concrete

Mechanical stress influences the velocity of elastic waves in a solid in several ways. It can permanently alter the physical or chemical parameters through damage, but the acoustoelastic effect can also lead to a perfectly reversible stress induced change of the seismic velocity.

6.3.2.1 Stress damage

Concrete is a conglomerate of a cement matrix with small aggregates. The hydration process of the concrete binds the aggregate's surfaces chemically to the cement matrix. When the concrete is exposed to physical or chemical stress, these boundaries are nuclei of crack formation. According to the literature, micro crack formation begins under minute stresses at the boundaries but can be healed chemically again. Whereas these effects are reversible, increasing stress leads to connection of these micro cracks, resulting in larger cracks which remain permanently and are not healed. These larger cracks are highly vulnerable to chemical weakening, like carbonation due to their large surface.

Since this corrosion affects physical parameters, like the elastic moduli, it can be measured as a change in sonic wave velocity. Furthermore, the crack opening can affect the quality factor Q.

Once large cracks have formed these effects are usually strong, i.e. greater than 1 % and measurement can be done well using the time-of-flight (TOF) of ballistic waves or the velocity of sonic surface waves (Shokouhi et al., 2010, Zoëga et al., 2009).

6.3.2.2 Acoustoelastic effect

General wave theory usually relies on Hooke's law, a linear first order expression of the stress-strain relation. When taking second order effects into consideration, an extended version of it applies, introducing the sixth-order tensor C_{abcdef}:

$$\sigma_{ab} = c_{abcd}\epsilon_{cd} + C_{abcdef}\epsilon_{cd}\epsilon_{ef} \tag{6-2}$$

Here σ and ϵ are the stress and strain tensors, respectively, and c_{abcd} is the fourth-order tensor of Hooke's law that can be expressed by the two Lamé parameters λ and μ in the case of an isotropic homogeneous medium. In an isotropic medium, the tensor C_{abcdef} has only 3 independent components, the so-called Murnaghan constants k,l,m, which describe the second-order behavior of the medium (Murnaghan, 1937; Hughes & Kelly, 1953).

While deriving velocities of seismic body waves from the classical Hooke's law is straightforward and a classical textbook issue, the derivation of wave speeds from equation (6-2) is complex and has been done yet only for special cases, like an infinitesimal hydrostatic pressures or uniaxial loads.

The results suggest that in the presence of an external pressure the isotropy of the material is lost and the wave speed depends on wave direction and polarization. For a small stress in x-direction ($\sigma_{xx} \gtrsim 0$) the velocities of waves propagating in x-direction with different polarization change as follows (Toupin & Bernstein, 1961):

$$\frac{1}{c_x^0}\frac{dv_x}{d\sigma_{xx}}\bigg|_{\sigma_{xx}=0} = \frac{1}{2E(\lambda+2\mu)} \cdot [-\nu(4\lambda+8\mu+2l+8m+8n)+(l+2m)] \tag{6-3}$$

$$\frac{1}{c_y^0}\frac{dv_y}{d\sigma_{xx}}\bigg|_{\sigma_{xx}=0} = \frac{1}{2E\mu}\cdot[-\nu(2\mu+2m+2n)+(2\mu+m+2n)] \tag{6-4}$$

$$\frac{1}{c_z^0}\frac{dv_z}{d\sigma_{xx}}\bigg|_{\sigma_{xx}=0} = \frac{1}{2E\mu}\cdot[-\nu(4\mu+2m+4n)+m] \tag{6-5}$$

where $E = \frac{(3\lambda+2\mu)\mu}{\lambda+\mu}$ is Young's modulus, and ν is Poisson's ratio.

This relation was used to determine the Murnaghan constants of various rocks, giving insight into the anisotropic velocity changes induced by external stresses. Typical values for l, m and n are negative and in the order of 1000 GPa, which leads to a relative variation of velocity with stress of about 10^{-3} MPa^{-1} (Johnson & Rasolofosaon, 1996).

These changes could be measured for geological stresses of some 100 MPa but were to minute to be detected in materials like concrete, which fail at a few 10 MPa. However, using ultrasonic waves combined with Coda Wave Interferometry (section III), the Murnaghan constants of a concrete sample could be determined recently (Pavan et al., 2009). Due to the strong heterogeneity of concrete, the mean free path of ultrasonic waves is like the wavelengths involved. This means that scattering and wave-type conversion are very strong, and it is difficult to distinguish experimentally between differently polarized wave-types.

6.3.3 Coda Wave Interferometry

6.3.3.1 Cross correlation for time delay estimation

The stretching method for Coda wave interferometry was already described in section 6.2.1. Here, a slightly different approach is presented as an alternative. The time series (reference signal and signal measured during the experiment) are cut into windows with a width of a few periods. For each window the two signals are compared by shifting one of the signals until a best fit is achieved. As in the stretching algorithm, cross-correlation is used as a measure for the goodness of the fit:

$$CC_{t_k}(t_s) = \frac{\int_{t-t_w}^{t+t_w} h(t'+t_s)\cdot h_0(t')\,dt'}{\sqrt{\int_{t-t_w}^{t+t_w} h^2(t')\,dt' \cdot \int_{t-t_w}^{t+t_w} h_0^2(t')\,dt'}} \qquad (6\text{-}6)$$

between time windows of length $2t_w$ centered around lapse time t of the original seismogram h_0 with the seismogram h from the disturbed state. The time lag t_s for which $CC_{t_k}(t_s)$ assumes its maximum is then a robust estimator of the time lag Δt(t) of the wave train. An example is shown in Figure 6-18. The left figure shows two identical synthetic signals with a small time lag, disturbed by strong noise. It is difficult to quantify the time lag between the two signals directly. However, if the cross-correlation between the two signals is regarded (right figure), the maximum of $CC_{t_k}(t_s)$ and thus the time lag $\Delta t = t_{s\,max}$ can be easily determined.

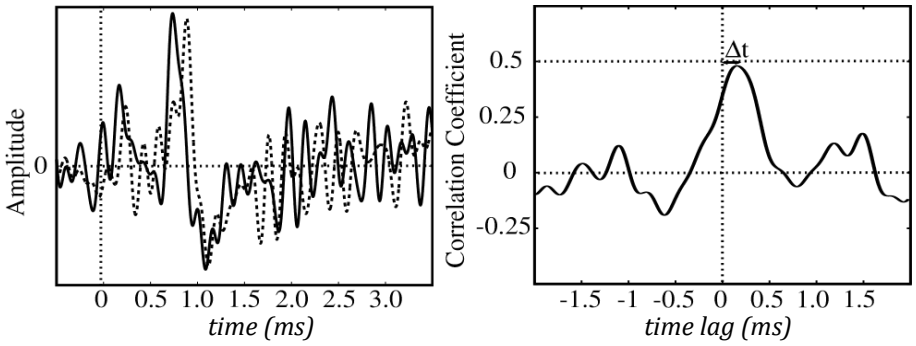

Figure 6-18: Example of time lag estimation using cross correlation coefficient

6.3.3.2 Coda Wave Interferometry

Coda Wave Interferometry uses the values of $CC_{t_k}(t_s)$ and Δt(t) calculated in time windows from the late part of the seismic signal that contains multiply scattered waves with large time of flight t. These waves have sampled the medium for a longer time so that even a small velocity change results in a notable absolute time lag. Furthermore, whereas the first arriving wave sampled only one path, i.e. one small region of the medium, the waves constituting the coda have sampled larger regions. This means that small changes anywhere in the specimen are visible in the coda, which makes this method ideal for nondestructive monitoring of engineering structures.

Different types of changes can be distinguished in the coda and related to different processes in the medium by interpreting the dependence of $CC_{t_k}(t_s)$ and Δt(t) on the time of flight of the scattered waves. A short overview of these types is given here, but the interested reader is referred to Snieder (2006).

- If the time lag Δt(t) changes proportionally with time t, but the value of $CC_{t_k}(t_s)$ remains constant, the wave velocity is modified homogeneously in a large region of the medium. This can be due to large scale stress changes.
- If $\Delta t(t) \approx 0$ irrespective of t but $CC_{t_k}(t_s)$ decreases, the number, kind, or location of any type of scatterers has changed. As typical scatterers are cracks or defects in the medium, this means that cracks have opened or widened, or their impedance contrast has changed.

By measuring Δt(t) and $CC_{t_k}(t_s)$ in different lapse time windows and for different source receiver combinations estimations about the location and the extent of the changes can be made (Sens-Schönfelder & Wegler, 2006; Pacheco & Snieder, 2005). In the present analysis, we focus on the first type of change, i.e. a large-scale change of seismic velocity. Such a change in the medium results in a phase delay that increases proportional to lapse time, thereby effectively stretching or compressing the time axis of the signal in the perturbed state.

In this case the stretching correlation technique can be applied to infer the underlying velocity change (Sens-Schönfelder & Wegler, 2006). This method relies on the correlation coefficient between the stretched or compressed trace and a reference[12]:

$$CC_{t_w}^{S}(v) = \frac{\int_{t-t_w}^{t+t_w} h_i\big(t\cdot(1-v)\big)\cdot h_0(t)\,dt}{\sqrt{\int_{t-t_w}^{t+t_w} h_i^2\big(t\cdot(1-v)\big)\,dt \cdot \int_{t-t_w}^{t+t_w} h_0^2(t)\,dt}} \qquad (6\text{-}7)$$

Compared to $CC_{t_k}(t_s)$, $CC_{t_w}^{S}(v)$ allows to use larger time windows t_w because the distortion of the trace is modeled better by stretching with a factor than by shifting a constant time t_s. This further enhances the precision of the measurement. The applicability of this technique has been shown in ultrasonic laboratory experiments (e. g. Hadziioannou et al., 2009) and various passive seismic examinations (e. g. Sens-Schönfelder & Larose, 2008).

6.3.4 Laboratory stress experiments

In a heterogeneous medium, such as concrete, the Murnaghan constants may vary strongly between different samples of the same material. Therefore, a laboratory experiment was conducted to determine the stress dependence of the wave velocities. Used was a specimen from the exact concrete of the bridge, provided by the construction enterprise. The concrete was 8 months old of strength class C40/50, according to DIN EN 206-1.

This specimen was loaded in a uniaxial press at the Federal Institute for Materials Testing and Research (Bundesanstalt für Materialforschung und Materialprüfung, BAM) in Berlin. On opposite sides of the sample ultrasonic P-wave transducers with central frequency of 250 kHz (source: UPG 250, receiver UPE 250, both from Geotron) were attached, which were excited with a 70 kHz central frequency pulse. The signal was generated and recorded by a Geotron UKS-D, normally used for direct time-of-flight and attenuation determination (see Figure 6-19).

[1212] This equation is like equation (6-1), but evaluation is limited to a certain part of the signals.

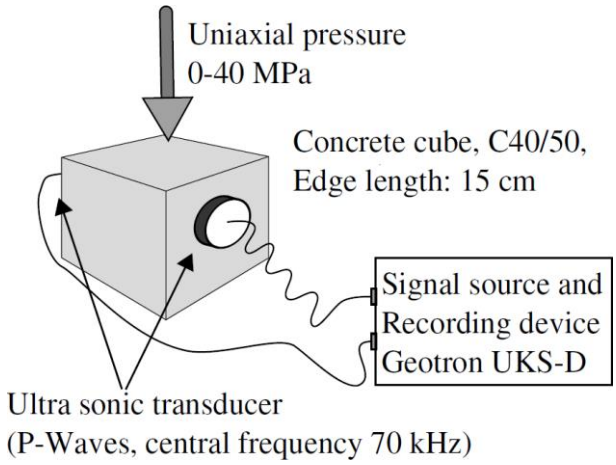

Figure 6-19: Sketch of laboratory experiment.

This experiment is similar to the measurements carried out by Larose & Hall (2009), who were able to determine stress-induced velocity variations in concrete with a relative resolution of $2 \cdot 10^{-5}$. Our experiments also aimed at estimating velocity effects due to stress damage in concrete. Therefore, we loaded the sample in small steps (ranging from 50 kPa to some MPa) with a stress of up to 45 MPa, which is 75 % of the break-down stress.

Figure 6-20 shows a comparison of two seismograms with minute stress difference. Whereas no difference is visible in the direct wave after 40 μs, the late time window around 1000 μs shows a clear advance of the phase in the stronger loaded state. Note that a travel time of 1000 μs corresponds to a P-wave path length of over 4 meters, which is 25 times the diameter of the specimen. Nevertheless, the signal shape remains very similar.

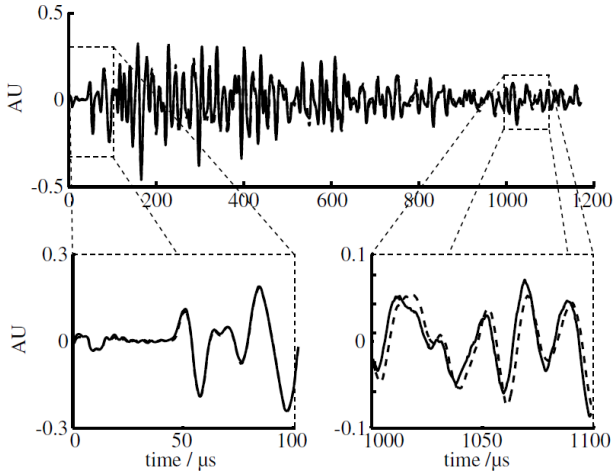

Figure 6-20: Comparison of Ultrasonic seismograms for 2 MPa (dashed line) and 2.4 MPa (bold line).

According to Sens-Schönfelder & Wegler (2006 the stretching correlation method (equation (6-7) is well suited to estimate the velocity change), since the signal shape is similar over a large time window.

The measured velocity variations as function of applied stress are shown in Figure 6-21. Stress states indicated by the characters are encountered in alphabetical order. During stressing from the initial state A to a stress of 20 MPa at state B an almost linear stress-velocity dependence of $\frac{\Delta c/c}{\sigma} = 0.5 \cdot 10^{-3}\ MPa^{-1}$ is observed. From the 20 MPa the stress was released again to reach state C corresponding to the initial stress. The velocity at state C is about 0.6 % than before loading. During the second loading to 20 MPa we notice an increase of $\frac{\Delta c/c}{\sigma}$ by a factor of 2 to $\frac{\Delta c/c}{\sigma} = 1 \cdot 10^{-3}\ MPa^{-1}$. Because of the increased slope the

velocity difference between A and C is compensated and the velocity at 20 MPa is the same after the first and second loading cycles. This can be explained by formation of cracks at the first loading. When releasing the stress, these cracks close again but are, due to the short time, not healed. This causes the remaining drop in the wave velocity between A and C. When loading the sample another time, almost no new cracks are formed, but instead the existing ones are activated, so that at 20 MPa the velocities reach the same level again.

When loading the sample over 20 MPa to state D, at 45 MPa (which corresponds to 75 % of the failure stress), the velocities dropped by almost 4 % from its highest level. At this stress, small cracks begin to connect to larger fissures which influence the elastic parameters strongly. This velocity drop was also detected by time of flight measurements. However, time of flight estimated the velocity change to be almost 12 %. This difference is due to the different wave types and directions that are mixed in the coda. Whereas the time of flight measurements are sensitive to variations of the compressional wave velocity in the direction between the receivers only, the CWI measurements average the sensitivities of the different wave types and directions according to their prevalence in the coda wave field. Sato & Fehler (1988), p. 223, state that the coda consists mainly of shear and surface waves. After releasing the stress again to reach state E, the velocities dropped permanently by 4.5 % compared to the initial velocity.

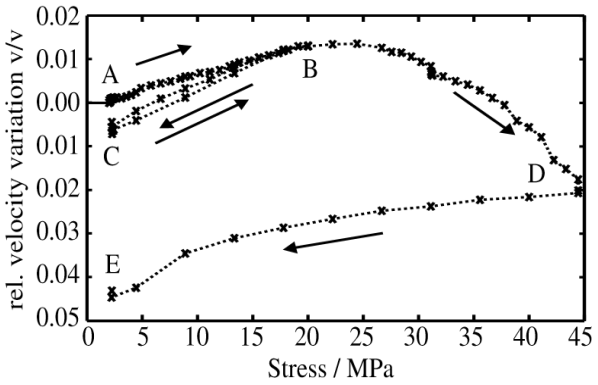

Figure 6-21: Velocities measured in ultrasonic experiment. Stress was increased from 0 MPa (A) to 20 MPa (B), then released back to 0 MPa (C). Afterwards the specimen was stressed with 40 MPa (D) and then decreased to zero again (E). One can notice a remanent velocity drop of 0.5 % after the first loading and of almost 5% after the strong stressing.

6.3.5 The bridge experiment

6.3.5.1 Experimental setup

While CWI measurements have been done in buildings allowing to monitor velocity changes in a ground floor concrete slab (Larose et al., 2006), no measurements were done in a structure with a known stress model yet, where a comparison between theoretical prediction and detected velocity changes is possible.

For such a comparison, an engineering structure with a changing stress state was needed, where at least some estimation of the tensions involved existed. A bridge in construction state, which was constructed using the Incremental Launch method (German: Taktschiebeverfahren, see Leonhardt & Baur, 1971), fulfilled this requirement. With this method, segments of the bridge girder are cast behind the abutment against the previously cast segments. The whole superstructure is then longitudinally pushed forward over the previously constructed substructure. The launching process is illustrated in Figure 6-22. Afterwards, a new segment is cast, connected and pushed, until the bridge has reached the opposite abutment. This method has been widely used in Europe for almost half a century (Zellner & Svensson, 1983) and is well suited for this experiment:

- During the launching, which takes place with about 10 m/h, the stress state changes almost continuously within the concrete of the structure, from stresses of up to 14 MPa to even a small tension of 0.5 MPa. This results in relative velocity variations of approximately 1.5 %.
- Since the launching is done within two or three hours, the measurement can be done quickly, which keeps environmental effects like varying sensor coupling or temperature changes small.
- Since the launching is carefully planned beforehand, an estimation of the involved stresses is already done by the involved engineers. This stress model can be used to estimate velocity variations that can be compared with the measured results.

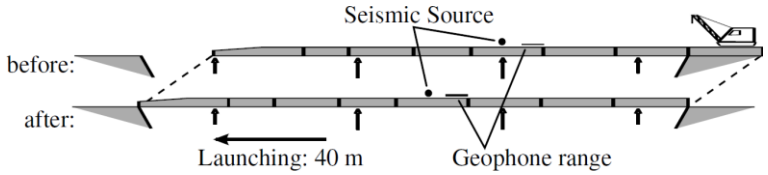

Figure 6-22: Sketch of the Launching. Included are the geophones used in the measurement.

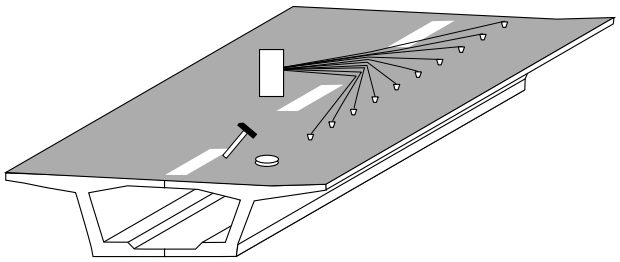

Figure 6-23: Sketch of the experimental setup with the hammer source and the geophones.

The experimental idea was then to measure seismograms of a point-like source in a distance of 6 to 10 meters with an array of geophones multiple times during the launching and compare the signal shapes (see Figure 6-23). A geophone is a vibration sensor used in Earth sciences consisting of a spring-mounted magnetic mass moving within a wire coil. The seismograms were high-pass filtered at 750 Hz, to exclude long period wave-types with wavelengths larger than the girder itself. With a compressional wave velocity of $c_p \approx 4000$ m·s^{-1} in concrete, the wavelengths involved are thus less than 5 meters. However, because the deck slab's thickness is small compared to its horizontal dimensions, virtually all wave energy was in Lamb modes, which are flexural waves with a significantly lower phase velocity c_φ (Royer & Dieulesaint, 2000):

$$c_\varphi = \sqrt{\frac{2\pi}{\sqrt{3}} f h c_s \sqrt{1 - \frac{c_s^2}{c_p^2}}} \tag{6-8}$$

Assuming $v_s = \sqrt{\frac{1}{3}} v_p$, h =0.5 m and f ≈ 1 kHz

$$c_\phi = \sqrt{\frac{2}{3}\pi f h c_p \sqrt{\frac{2}{3}}} \tag{6-9}$$

$$c_\phi \approx 1850\ m \cdot s^{-1}$$

$$\lambda \approx 1.85\ m$$

The distance of at least 6 meters was thus enough to be outside the source's near-field. 12 geophones were laid out in a line, with 50 cm distance in between (see Figure 6-23).

The experiment was conducted using standard geophones with an eigenfrequency of 10 Hz, far below the cutoff frequency of the low-pass filter. To excite the elastic waves, we used a hammer and plate source, which is simply a heavy hammer being dropped on an aluminum plate. While geophysicists generally consider the sledgehammer to produce mostly low frequency signals below 100 Hz (Keiswetter & Steeples, 1995), it was found in preliminary experiments, that this does not hold true for a plate directly connected to a concrete structure. Here the plate excites a broad frequency spectrum reaching beyond 4 kHz, which allows this simple method to be used here. Since the source time function depends on the actual way the strike is carried out, it can vary significantly between measurements. If waveforms are to be compared, a constant source time function must be assumed. To weaken the influence of a varying source 10 measurements at a time were stacked, which also helped to reduce noise.

6.3.5.2 Results

To understand the wave propagation in the bridge and to compare the experimentals with predictions from the stress model we performed a fully elastic 3D simulation[13]. Figure 6-25 shows a comparison between the modeled and measured seismogram sections. A clear wave train is visible in both seismograms with a velocity of about 1700 $m \cdot s^{-1}$, which contains most of the energy. It corresponds to the direct Lamb wave. Reflections from the sides of the bridge are visible mainly in the numerical simulations as waves with high apparent velocity. These phases are not as clear in the real data probably because of internal heterogeneity. Scattering on minor parts of the structure, like steel tendons within the girder leads to a loss of coherency. All in all, comparison with the numerical simulations shows that the exact wave field is more complex than expected from a homogeneous medium with the shape of the bridge.

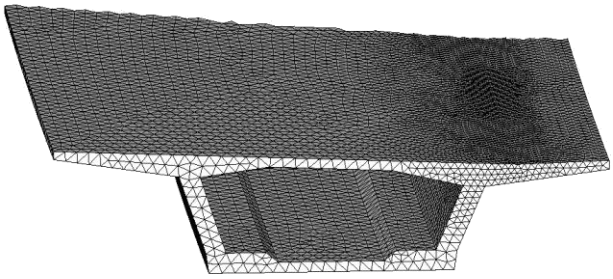

Figure 6-24: Part of the mesh of the bridge used for numerical simulation with Seissol.

[13] The simulation was done using Seissol, a Discontinuous Galerkin (DG) Finite Element (FE) method with third order derivatives for flux calculation (Shapiro & Kneib, 1993). The parameters of this simulation were: c_p =4100 $m \cdot s^{-1}$, c_s = 2367 $m \cdot s^{-1}$, mesh width = 0.5 m, while the geometry of the mesh was adapted closely to the exterior shape of the bridge (see Figure 6-24). The calculations were done on the TETHYS cluster of the Geophysics Institute at LMU München (Page et al., 1995).

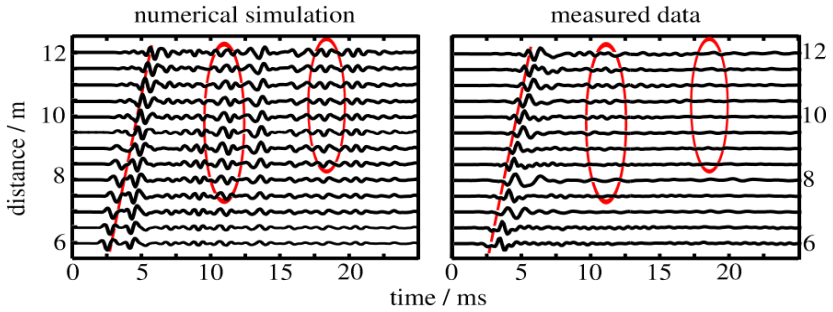

Figure 6-25: Seismogram sections of all geophones. Left: Results of numerical simulation using Seissol. Right: normalized by running average over a 2.5 ms time window.

However, seismograms recorded at different stages of launching are quite similar and we test the hypothesis that wave form changes are primarily due to variations of the velocities.

To quantify whether the changes in the seismogram can be attributed to velocity variations, we calculated the decorrelation of the signals (defined as $D_0 = 1 - CC_{t_w}^s(\nu = 0)$ between a reference measurement (measurement 5) and all others for each geophone. The decorrelation gives an estimation of signal dissimilarity, ranging from 0 (signals are identical) to 1 (signals are totally uncorrelated). Figure 6-26 shows D_0 for all measurements. It is zero for measurement five because it is used as reference and increases with temporal distance from this reference for all geophones indicating that the changing state of stress in the bridge changes the wave forms.

If the effect of a spatially homogeneous velocity change is corrected by stretching or compressing the time axis of the records, we obtain the minimum decorrelation $D_{min} = 1 - CC_{t_w}^s(\nu_{max})$ is also shown in Figure 6-26. The decorrelation of all wave forms can be reduced significantly by correcting for the velocity change, indicating that a homogeneous velocity change is an acceptable model for the medium changes that cause the alteration of the wave forms. The remaining decorrelation is a result of the non-homogeneous velocity changes that do not lead to a lapse time proportional phase shift.

To determine the velocity variation that underlies the wave form change, we examined the signal stretching factor ν_{max} (see equation (6-7)), which maximized CC^S. Since the extent of the geophone array is short compared to the spatial wavelength of the stress change (distance of pillars), the value of ν_{max} does not depend on the position of the geophone. We therefore show the mean of all measurements of ν_{max} converted to velocity change as $\frac{\Delta c}{c} \approx \nu$ in Figure 6-27. Error bars correspond to the limits of the second and third quartile of the 96 measurements at each state of the launching process (measurements from 12 geophones against 8 possible reference traces). A clear decrease of the velocity is observed from the beginning of the measurements until the fifth or sixth measurement where the velocity reaches a minimum. Later on, the velocity increases again to reach values similar to the beginning of the launching.

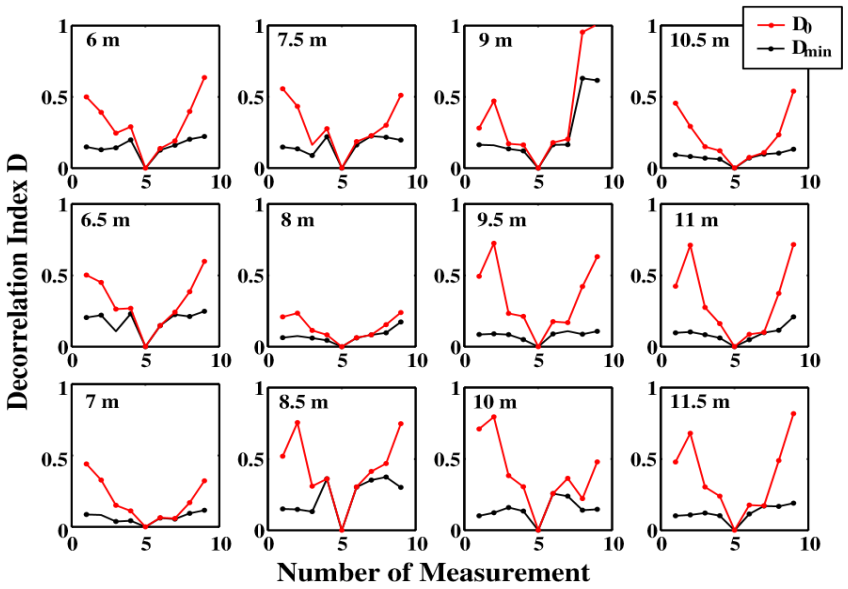

Figure 6-26: Decorrelation of seismograms, red line: decorrelation of raw seismograms D_0, black line decorrelation of seismograms after correction for spatially homogeneous velocity change D_{min}.

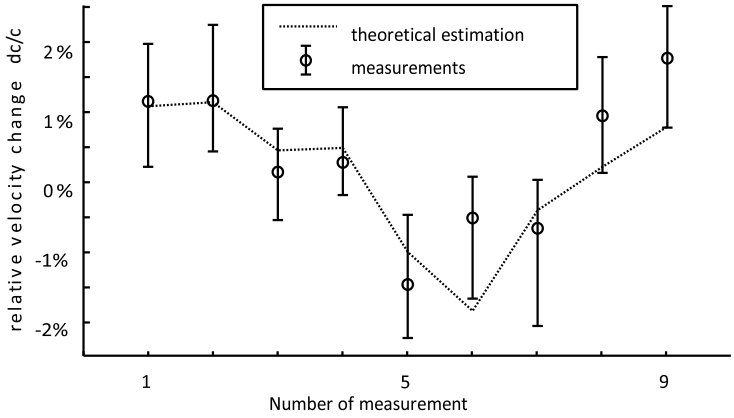

Figure 6-27: Measured velocity variations in bridge with quartile limits, compared with results from FD-Simulation.

6.3.5.3 Comparison with theoretical estimations

To investigate if the measured velocity variations can be attributed to the stress changes from the launching, an acoustic finite-difference (FD) simulation of the wavefield in the girder was performed for each launching state[14]. To relate the stress changes to variations of the seismic velocity, the parameters from the laboratory experiment (section 6.3.4) where used. On the retrieved synthetic seismograms, the same algorithm was applied as on the measured seismograms to infer ν_{max}. This is again converted to velocity change and plotted in Figure 6-27.

The results of the measurements are in good agreement with the estimations from the FD simulation identifying the stress changes as cause of the velocity variations. A clear

[14] For the sake of simplicity and speed, this was done using an 3D acoustic FD code with a mesh size of 0.01 m and a assumed wave velocity of 4100 m·s^{-1}. The calculations were done at the Institute for Geophysics and Geology of Leipzig University

minimum is observed at position of the sixth measurement with higher velocities at the beginning and the end of the launching.

6.3.6 Discussion of results

The laboratory experiments again proved the unprecedented accuracy of the Coda Wave Interferometry method in measuring the acoustoelastic effect. It also showed well were damage-induced effects on the slope of the stress-velocity curve, an effect previously not detected using body waves. The large drop in velocity after a near-breakdown-stressing was in good agreement with time of flight measurements. The inferred dependence of the wave velocity on the mechanical stress formed the basis for the interpretation of the field data.

The bridge experiment showed the difficulties of applying this laboratory concept to a large structure with complex wave propagation. To utilize the robust geophysical equipment, we used a frequency band at about 1 kHz. Scattering at internal heterogeneity of the concrete is weak at this frequency and the medium appears homogeneous. The generation of coda waves thus relies on scattering at minor parts of the structure and on multiple reflections from the boundaries. The numerical simulations showed that these processes are sufficiently effective to generate signals with the required lapse time. This allowed to measure velocity changes in a time window from 5 ms to 15 ms which can be mostly described by the theoretical concept. Potential error sources are the engineer's stress estimations itself, which did not aim to provide a completely realistic stress model for the whole bridge superstructure, but merely to ensure certain critical material thresholds were not reached. Furthermore, our model of assuming an isotropic wave velocity change in the material is just an approximation of the anisotropic acoustoelastic effect.

It should also be noted that there is uncertainty in the timing of the launching so that the stress states from the FD simulation do not perfectly agree with the states at the time of the measurements. This can be a partial explanation for the differences between predictions and measurements.

6.3.7 Summary and outlook

We have presented an experiment to monitor dynamic stress changes in a concrete bridge with seismic waves. The experiment used geophysical equipment to record vibrations excited by hammer strikes at different stress states. Stress changes in the structure were caused by movement of the bridge's superstructure over the pillars during construction with the incremental launching technique. To relate observed changes in the seismic velocity with the stress changes in the structure the stress velocity relationship was measured in laboratory experiments with samples of the bridge's concrete. Using this relationship our data fit the stress model that was calculated by the engineers beforehand. The experiment demonstrates that stress changes can be measured with seismic waves not only in the controlled environment of a laboratory but also in the field at engineering structures. The sensitivity of the measurements that took place at a construction site can be improved by a permanent installation of the sensors, the utilization of a source with higher repeatability and the use of higher frequencies that experience stronger scattering.

6.4 Laboratory experiments – imaging[15]

6.4.1 Introduction

Engineered structures, such as buildings, roads, and bridges, are known to undergo wear and tear over time which can compromise the durability of these structures. The resulting defects within the structures can be weak and hard to detect, so that their effect on the overall integrity of the structures are detected late. For an optimal management of these structures and the overall safety of their use, there is a need to monitor the structures continuously with a tool or method that has the sensitivity to identify the defects before they escalate to a destructive stage. Coda Wave Interferometry (CWI) provides a tool to identify weak changes or defects within a scattering medium, such as in monitoring of volcanoes (Matsumoto et al., 2001), subsurface velocity changes near faults (Schaff & Beroza, 2004) or in the near subsurface (Poupinet et al., 1984; Spane et al., 2002) or changes in concrete blocks induced by either stress changes or temperature changes (Planès et al., 2014; Grêt et al., 2006b; Larose & Hall, 2009; Kanu & Snieder, 2015). The higher sensitivity of the coda waves to weak changes compared to direct or singly scattered waves allows for the detection of weak changes within scattering media. However, the coda waves provide spatially averaged estimates of the weak changes especially in cases where the time-lapse changes are localized. This spatial averaging limits the ability to resolve the locations of the weak changes. We present two laboratory experiments with concrete blocks in which we monitor weak changes. In one of the experiments we monitor a weak change due to an induced compressive stress (force) at the opposite sides of the concrete block while in the second experiment we monitor changes due to temperature changes within a different concrete block. The temperature changes in the concrete block is due either to the ambient temperature fluctuations within the concrete or to a localized heating provided by a heat cartridge within the concrete block. In this study, we apply an imaging algorithm based on the scattered intensity of the time-lapse coda to localize the weak changes within the concrete blocks (Kanu & Snieder, 2015).

6.4.2 Theory

Velocity changes and changes in the scattering properties of a heterogeneous medium induce changes within time-lapse coda waves. Pacheco & Snieder (2005) and Rosetto et al. (2011) related the travel-time changes and decorrelation of the time-lapse coda waves to velocity changes and perturbations in the scattering cross-section of the medium, respectively. Using probability density functions, Pacheco & Snieder (2005) gave the relationship between a localized fractional velocity change $\frac{\delta c}{c}(\boldsymbol{x_0})$ at position $\boldsymbol{x}_0$ and the estimated travel-time changes $\langle \tau(t) \rangle$ induced by the velocity change:

$$\langle \tau(t) \rangle = -\int_V K(\boldsymbol{s}, \boldsymbol{x}_0, \boldsymbol{r}, t)\, \frac{\delta c}{c}(\boldsymbol{x}_0)\, dV(\boldsymbol{x}_0), \qquad (6\text{-}10)$$

where $K(\mathbf{s},\mathbf{x}_0,\mathbf{r},t)$ is the sensitivity of the travel-time change to the localized velocity change in the scattering medium. The sensitivity, which is computed using the intensity of the scattered wavefield (Kanu & Snieder, 2014), depends on the source and receiver locations ($\mathbf{s}$ and $\mathbf{r}$), the scattering property of the medium, and the travel time of the scattered waves.

[15] This section is edited from Kanu et al., 2017. This research was supported by sponsors of the Consortium Project on Seismic Inverse Methods for Complex Structures of Colorado School of Mines and the Bundesanstalt für Materialforschung und -prüfung. (BAM).

Similarly, Rosetto et al. (2011) relate the decorrelation D(**s**,**r**,t) between time-lapse multiply scattered waves to the time-lapse change in the total scattering cross-section $\delta\sigma(\boldsymbol{x}_0)$ of a medium:

$$D(\boldsymbol{s},\boldsymbol{r},t) = -\frac{v}{2}\int_V K(\boldsymbol{s},\boldsymbol{x}_0,\boldsymbol{r},t)\ \delta\sigma(\boldsymbol{x}_0)\ dV(\boldsymbol{x}_0). \tag{6-11}$$

The change in the total scattering cross-subsection describes a change in the scattering property the medium. The travel-time changes $\langle\tau(t)\rangle$ and the decorrelation D(**s**,**r**,t) can be estimated for a given source-receiver pair (S-R) by comparing the time-lapse coda waves. Practically, the time-windowed decorrelation is obtained by a modified version of (6-6)

$$\begin{aligned} D(\boldsymbol{s},\boldsymbol{r},t) &= 1 - CC(\boldsymbol{s},\boldsymbol{r},t) \\ &= 1 - \frac{\int_{t-t_w}^{t+t_w} h(\boldsymbol{s},\boldsymbol{r},t'+t_s)\cdot h_0(\boldsymbol{s},\boldsymbol{r},t')\,dt'}{\sqrt{\int_{t-t_w}^{t+t_w} h^2(\boldsymbol{s},\boldsymbol{r},t')\,dt' \cdot \int_{t-t_w}^{t+t_w} h_0^2(\boldsymbol{s},\boldsymbol{r},t')\,dt'}} \end{aligned} \tag{6-12}$$

where t is the travel-time and t_w is the half-length of the time-window use to compute the cross-correlation CC(**s**,**r**,t). We estimate the travel-time changes $\langle\tau(t)\rangle = -vt$ using the stretching method (Hadziioannou et al., 2009) for a given time window of the scattered waves, where v is the stretching factor. The stretching factor is equal to the estimated fractional velocity change within the time window. To obtain the optimal stretch factor, we minimize

$$\min \quad f(v) = \|h_0(t+vt) - h(t)\|_2^{t,t_w} \tag{6-13}$$

Where h(t) and h_0(t) are the original (reference) and the time-lapse coda signals, respectively.

The sensitivity kernel in equations (6-10) and (6-11) is given by

$$K(\boldsymbol{s},\boldsymbol{x}_0,\boldsymbol{r},t) = \frac{\int_0^t P(\boldsymbol{s},\boldsymbol{x}_0,t')P(\boldsymbol{x}_0,\boldsymbol{r},t-t')dt'}{P(\boldsymbol{s},\boldsymbol{r},t')} \tag{6-14}$$

Where P is the average intensity of the multiple scattered waves (Pacheco & Snieder, 2005). The sensitivity kernel K(**s**,$\mathbf{x}_0$,**r**,t) can be estimated either by using analytical (Pacheco & Snieder, 2005; Rosetto et al., 2011) or numerical methods (Kanu & Snieder, 2014). The analytical method for computing K(**s**,$\mathbf{x}_0$,**r**,t) uses either the diffusion (Wesley, 1965; Shapiro & Kneib, 1993; Page et al., 1995) or the radiative transfer formulation of the scattered intensity (Paasschens, 1997). However, the analytical methods typically assume that the scattering medium is homogeneous in a statistical sense. In a medium where the scattering properties are spatially varying, the numerical method of computing the sensitivity kernel is preferred, because the sensitivity is computed numerically with an a priori estimate of the scattering model by numerically computing the normalized intensity of the multiply scattered waves generated within the medium. The concrete blocks we use for the time-lapse monitoring are casted with homogenous size of gravel and cement materials. The analytical models can give an approximate estimate of the scattered intensity within the concrete blocks. Here, the radiative transfer formulation defined by the mean free path length l is used to characterize the scattered intensities.

6.4.3 Estimation of mean free path length

The mean free path length for the concrete blocks is calculated by simultaneously fitting the recorded scattered intensities recorded by all the source-receiver pairs (separately for each experiment) with an analytical intensity model. Assuming uniform scattering properties for the concrete blocks, the scattered intensities are modeled with a 3D radiative transfer intensity model (Paasschens, 1997) given by

$$P(\boldsymbol{r},t)=\frac{e^{-\frac{vt}{l}}}{4\pi vr^2}\delta\left(t-\frac{r}{v}\right)+\frac{\left(1-\frac{r^2}{(vt)^2}\right)^{\frac{1}{8}}}{\left(\frac{4\pi lvt}{3}\right)^{\frac{3}{2}}}e^{-\frac{vt}{l}}M\left(\frac{vt}{l}\left(1-\frac{r^2}{(vt)^2}\right)^{\frac{3}{4}}\right)H(-\frac{r}{v}) \tag{6-15}$$

Where $M(x)\approx e^x\sqrt{1+2.026/x}$, r is the source-receiver distance, t is the travel-time of the scattered intensity, v is the mean velocity of the scattering medium, l is the mean free path length, δ is the delta function, and H is the Heaviside step function. Assuming acoustic scattering, we use the P-wave velocity of 2700 m·s^{-1} as the mean velocity of the scattering medium.

We estimate the mean free path length l using a grid search of the mean free path length within a pre-defined range of values. We pick an optimal mean free path length that gives the minimum normalized root mean square error NMRS given as

$$NRMS=\frac{\left(\frac{\left[\left(d-g(l,V_0)\right)^T(d-g(l,V_0))\right]}{N}\right)^2}{d_1-d_2} \tag{6-16}$$

where d is the data vector containing the recorded scattered intensity vector for each source-receiver pair, g is the predicted scattered intensity vector, T is a transpose operator, N is the number of source-receiver pairs, d_1 and d_2 are maximum and minimum values in the data vector. To compute the radiative transfer scattered intensity within the 3D concrete blocks used for the time-lapse experiments, we impose full reflection boundary conditions at the 6 faces of the concrete blocks. Using the mirror approach, the total radiative transfer scattering intensities P^{RF} within the 3D concrete blocks is given as:

$$\begin{aligned}P^{RF}(\boldsymbol{r},t)=\;&P(\boldsymbol{x},\boldsymbol{x}_0,t)+P(\boldsymbol{x},\boldsymbol{x}_x^1,t)+P(\boldsymbol{x},\boldsymbol{x}_x^2,t)\\&+P(\boldsymbol{x},\boldsymbol{x}_y^1,t)+P(\boldsymbol{x},\boldsymbol{x}_y^2,t)+P(\boldsymbol{x},\boldsymbol{x}_z^1,t)+P(\boldsymbol{x},\boldsymbol{x}_z^2,t)\end{aligned} \tag{6-17}$$

where locations $x_0, x_x^1, \dots, x_z^2$ are supports for the mirroring of the radiative transfer solution due to the fully reflecting boundaries and their coordinates are given as:

$$\begin{aligned}\boldsymbol{x}_0&=[x_0\;\;y_0\;\;z_0]\\\boldsymbol{x}_x^1&=[(2h_x-x_0)\;\;y_0\;\;z_0]\\\boldsymbol{x}_x^2&=[-x_0\;\;y_0\;\;z_0]\\\boldsymbol{x}_y^1&=[x_0\;\;(2h_y-y_{0)}\;\;z_0]\\\boldsymbol{x}_y^2&=[x_0\;\;-y_0\;\;z_0]\\\boldsymbol{x}_y^1&=[x_0\;\;y_0\;\;(2h_z-z_{0)}]\\\boldsymbol{x}_y^2&=[x_0\;\;y_0\;\;-z_0]\end{aligned} \tag{6-18}$$

and h_x, h_y, and h_z are the dimensions of the concrete block along the x-, y-, and z- axis, respectively.

6.4.4 Concrete block with stress changes

To demonstrate the capability of resolving weak changes within a scattering medium, we invert for a change induced by a localized stress loading on the surface of a concrete block with dimensions 1.5 x 1.5 x 0.5 m^3. The concrete block (PK32), with an average P-wave velocity of 2700 $m \cdot s^{-1}$, consists of aggregate (which act as scatterers) of size of maximum 32 mm and reinforcements in half of the block (Figure 6-28). The reinforcement consists of a steel rebar mesh of 8 mm rods spaced at 150 mm intervals. Within the block, we embedded 18 transducers that serve both as sources and receivers. For specification of the sensors, see Niederleithinger et al. (2015b). Figure 6-29 gives the locations of the used transducers. The coordinates are given in Table 6-1. Because of coupling issues, we use only 10 of the transducers. These 10 transducers are connected to ultrasound transmitting and receiving equipment via a multiplexer. The multiplexer connects an amplified signal generated by a function generator to a given transducer selected at a given time (Figure 6-30). This selected transducer acts as the source while the rest of the transducers serve as receivers. The recorded signals are sent to an Analog-to-Digital (A/D) device and then to data storage. A given load experiment results to a total of 90 traces. The source signal has a dominant frequency of 60 kHz.

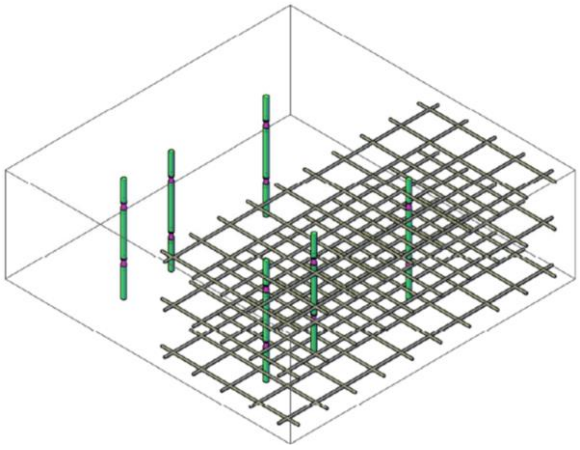

Figure 6-28: Schematic of the 3D concrete block for time-lapse monitoring.

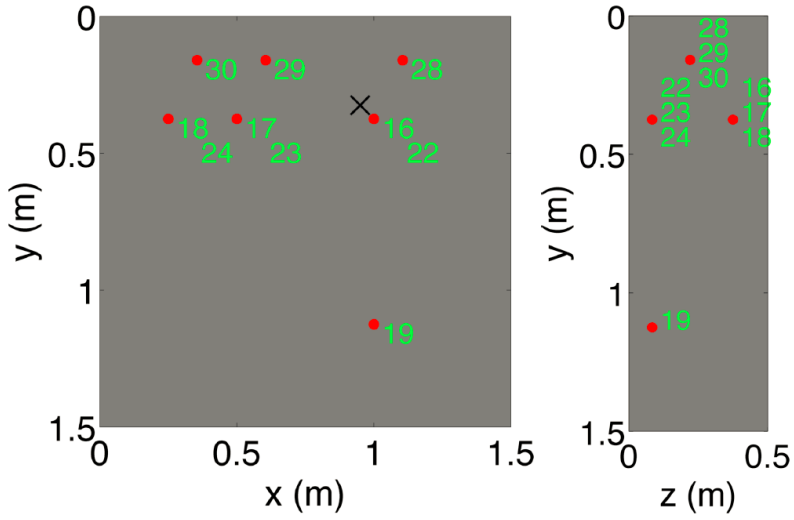

Figure 6-29: Outline of the 3D concrete block with the locations of the transducers. The transducers are embedded within the concrete block. The transducer locations are the projection along the z-axis (left) and along the x-axis (right).

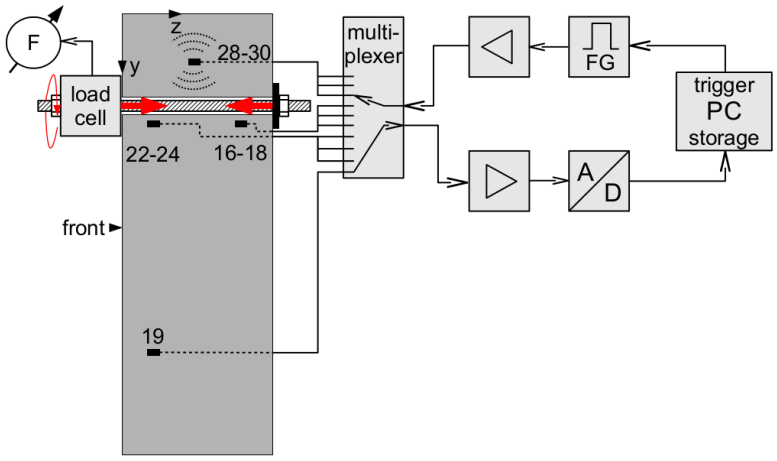

Figure 6-30: The electrical and mechanical setup of the stress loading experiment.

To induce a local change on the concrete block, we apply a stress loading on a 30-mm borehole drilled through the block along the z-axis. The borehole is located at (x = 0.95 m, y = 0.325 m). A 20-mm bolt is put through the borehole and fastened on both sides with load distribution steel plates and nuts. The load steel plates are 0.1 x 0.1 m^2 wide and 10 mm thick. On one side of the block, a calibrated load cell (a piezoelectric sensor) is placed between the load steel plate and an additional disc. The load cell is used for current supply and voltage measurement. This experiment which was designed and setup at the Federal Institute for Materials Research and Testing, Berlin, Germany (BAM) involves monitoring series of stress loading ranging from 0 kN to 100 kN and back to 0 kN. The block (PK32) has been used for earlier coda wave experiments as well (Niederleithinger et al., 2014).

Figure 6-31 shows typical signals recorded at transducer 17 when transducer 16 acts as a source. At t = 0 each receiver records an event from the source induced electrical response. We use this electrical event (Figure 6-31, black ellipse) to book-keep the onset time of the source signals. This event is removed prior to time-lapse analysis of the signals. The rest of the recorded scattered waves in the signals consists of ballistic and coda waves resulting from wave scattering within the concrete block. The two signals in Figure 6-31 are from repeated experiments on a given stress load displaying the strong repeatability of the signals.

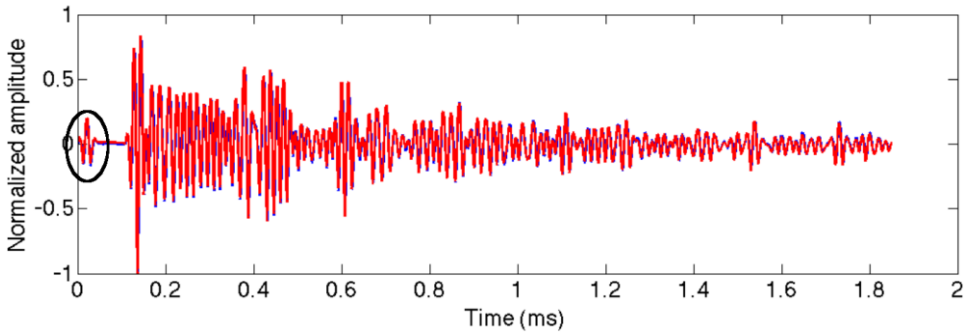

Figure 6-31: Typical time-lapse coda signals recorded at transducer 17 due to a source at transducer 16 from the stress loading experiment. The black ellipse indicates the electrical signal used to book-keep the source onset time.

6.4.4.1 Data analysis

Using Coda Wave Interferometry analysis (CWI), we can estimate the fractional velocity change δc/c and the decorrelation D of the time-lapse coda signals for a specific time window using either the stretching method (Hadziioannou et al., 2009), or by computing $D = 1\text{-}CC_{max}$ (6-12), respectively.

Table 6-1: Transducer coordinates.

Transducer No.	x(mm)	y(mm)	z(mm)
16	1000	375	374.5
17	500	375	374.5
18	250	375	374.5
19	1000	1125	83.5
22	1000	375	83.5
23	500	375	83.5
24	250	375	83.5
28	1105	160	220
29	605	160	220
30	355	160	220
Load	950	325	0-500

Figure 6-32 and Figure 6-33 show the estimated decorrelation D and the estimated fractional velocity change δc/c from the 90 time-lapse coda signals in the stress experiment, respectively. The estimates of the decorrelation or the fractional velocity change before the first arrival is zeroed out because of zero signal-to-noise ratio. The figures compare changes due to load jumps from 5 kN to 10 kN and from 5 kN to 15 kN. The changes are greater for the 5 kN-15 kN load jump than for the 5 kN-10 kN load jump (Figure 6-32 and Figure 6-33). The estimated changes are as expected more pronounced for later coda lapse times. Traces 28-35 (source transducer no. 19, far away from the load)) show less change than most other traces. These and other differences in the time-lapse changes across the traces are due to the arrangements of the sensors relative to the location of the time-lapse change.

Figure 6-34 provides a raw picture of the recorded time-lapse change for individual transducer pairs. The figure shows an indication of a localized change. It shows the average decorrelations estimated from the time-lapse scattered waves arriving between 0.28 ms and 0.58 ms after the first arrival time. The decorrelations are estimated using the time-window marked in Figure 6-35 (top). Larger decorrelation results from the load jump of 5 kN to 15 kN compared to the load jump of 5 kN to 10 kN and from the sensor pairs close to the location of the compressive loads. However, the sources of decorrelations for each sensor pairs are not restricted to these lines.

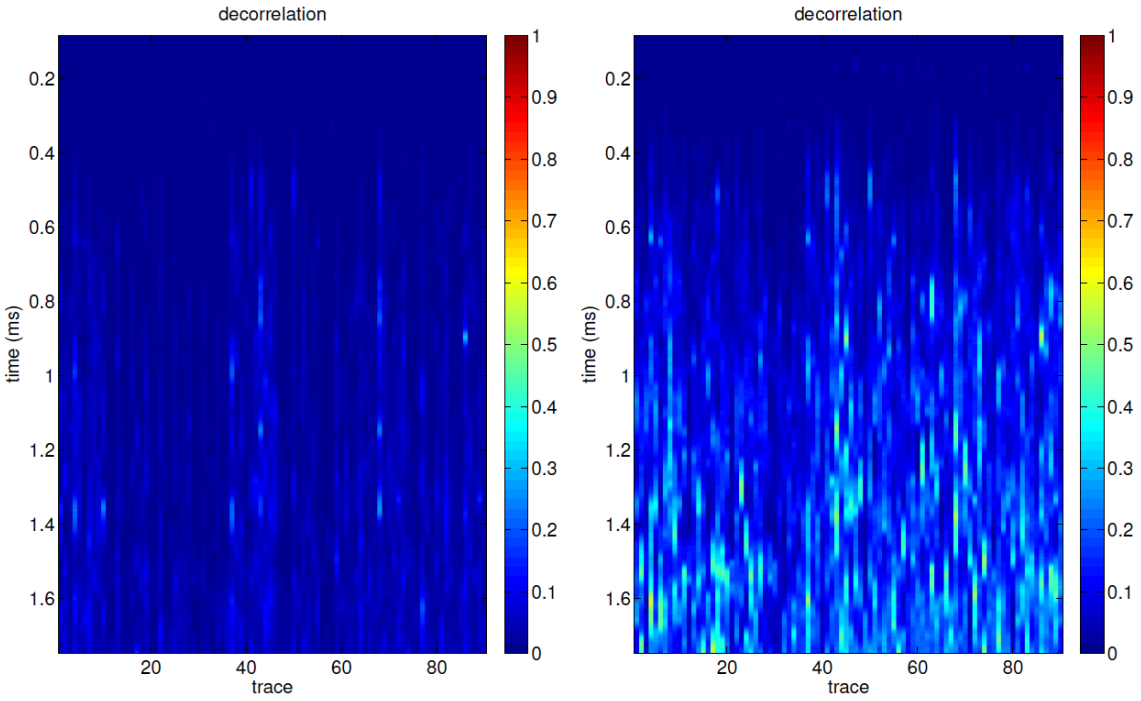

Figure 6-32: Record of the estimated time-lapse decorrelation due to a load jump from 5 kN to 10 kN (left) and a load jump from 5 kN to 15 kN (right). The record contains 90 traces. The records are arranged per the source sensor records.

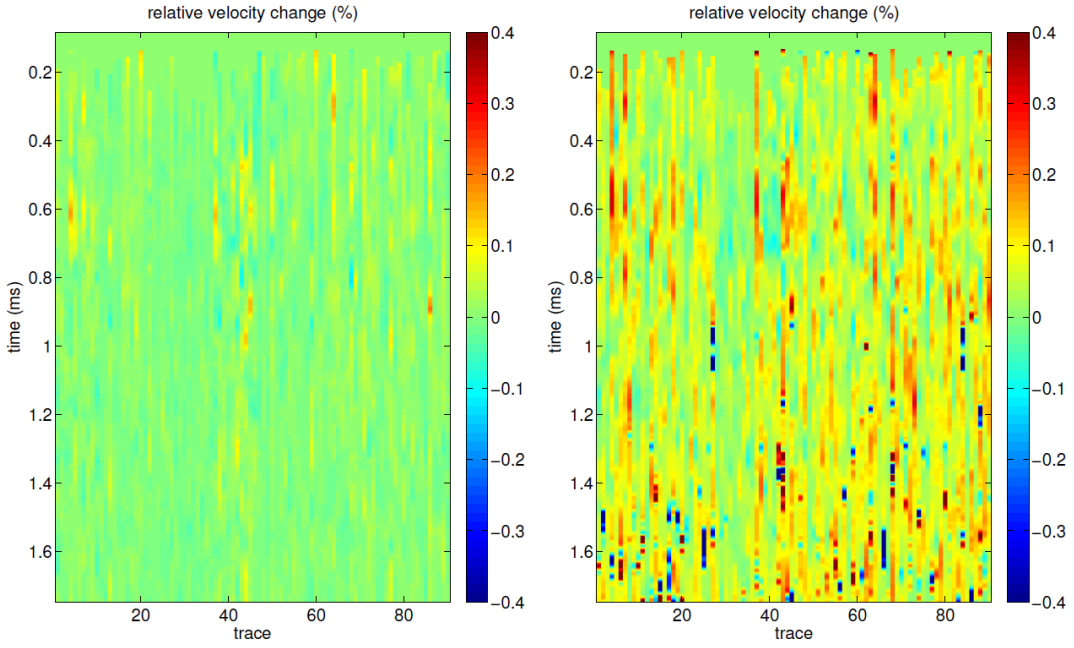

Figure 6-33: Record of the estimated time-lapse relative velocity change in % due to a load jump from 5 kN to 10 kN (left) and a load jump from 5 kN to 15 kN (right). The record contains 90 traces. The records are arranged per the source sensor records.

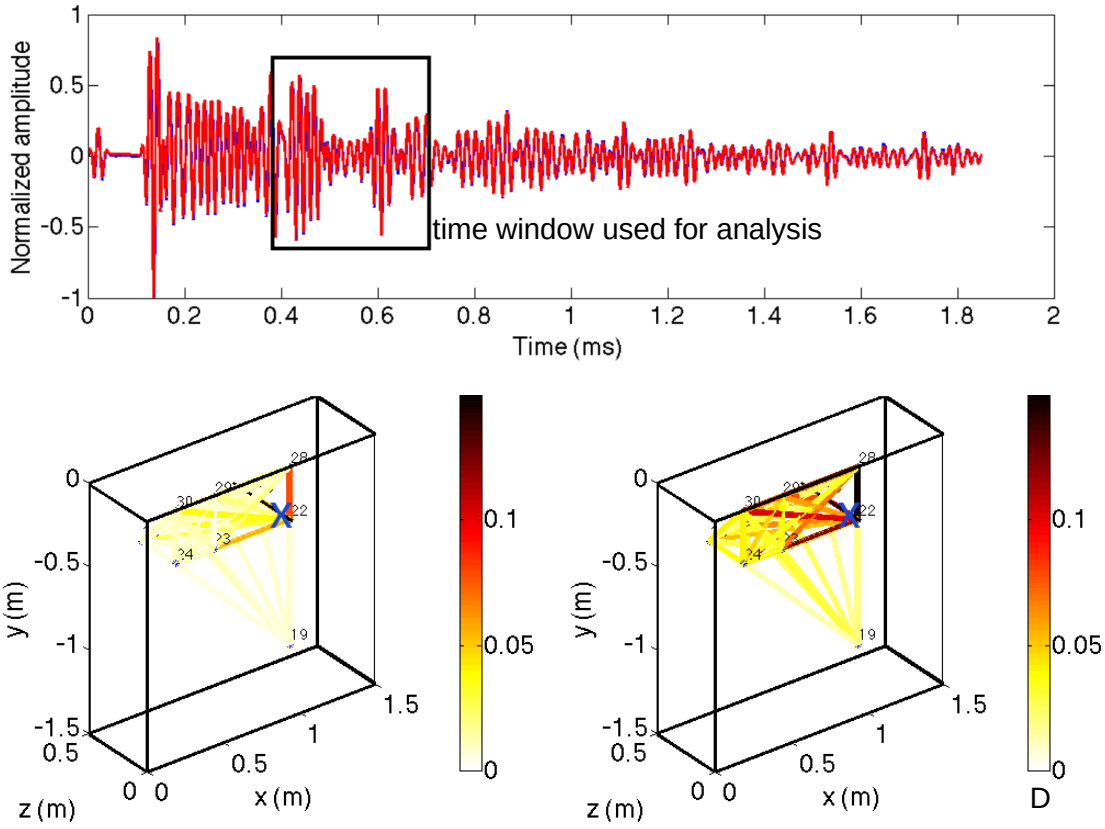

Figure 6-34: Time-lapse decorrelation due to stress loading from 5 kN to 10 kN (lower left) and from 5 kN to 15 kN (lower right). Blue cross: loading point. The color of the lines between two sensors correspond to the estimated average decorrelation between the time lapse signals for the time window marked in the top figure. The later shows two (hardly discernible) signals from different loading states.

6.4.4.2 Inversion results

To invert for the changes induced by the stress loadings, we solve

$$\boldsymbol{K}^T \boldsymbol{W}_d^T d = \left[\boldsymbol{K}^T \boldsymbol{W}_d^T \boldsymbol{W}_d K + \beta \boldsymbol{I}\right] \boldsymbol{m} \qquad (6\text{-}19)$$

where K^T is a discretized version of the sensitivity kernel (6-14) of the travel-time change or the decorrelation to the localized change in the scattering model using multiply scattered waves, W_d is the data weighting matrix, β is a regularization parameter, and m defines the inverted change in the scattering medium which is either the change in velocity or the change in the scattering cross-section. The data is either the decorrelation of the time-lapse coda or the travel-time change from the time-lapse coda. To solve equation (6-19), we use a linear conjugate-gradient method.

The sensitivity kernels were computed using radiative transfer model of the scattered intensity in the block with fully reflecting boundary conditions (Rosetto et al., 2011) on the planar boundaries of the concrete block. We currently assume acoustic wave scattering. To estimate the sensitivity kernel, we estimate the average mean free path by selecting the mean free path that minimizes equation (6-16) by fitting the intensities of the coda waves using 3D radiative transfer intensity (equation (6-15)). The mean free path was estimated to be approximately 0.055 m (Figure 6-35) which corresponds to a mean free time of 0.014 ms using p-wave velocity for the stress experiment. The time window used for the inversion extends beyond the mean free time and was identical to the one shown in

Figure 6-35. Figure 6-36 shows the inverted solution of the weak changes within the concrete block in the stress experiment at z = 0 m for stress loading of 5 kN - 10 kN and 5 kN - 15 kN using the time window in Figure 6-36 (top). We use the decorrelation of the time-lapse coda for the inversion. These stress loadings induce a relatively more significant and consistent perturbation on the amplitude of the coda signals than on the phase of the coda (which is consistent with the findings of Zhang et al., 2016). Figure 6-36 shows the resolved change which is at proximity to the point of the stress loading for both stress experiments. The resolution of the weak change depends on the source-receiver coverage and the time windows we use for the inversion due to the spatial broadening of the sensitivity kernel with travel-time (Kanu & Snieder, 2014).

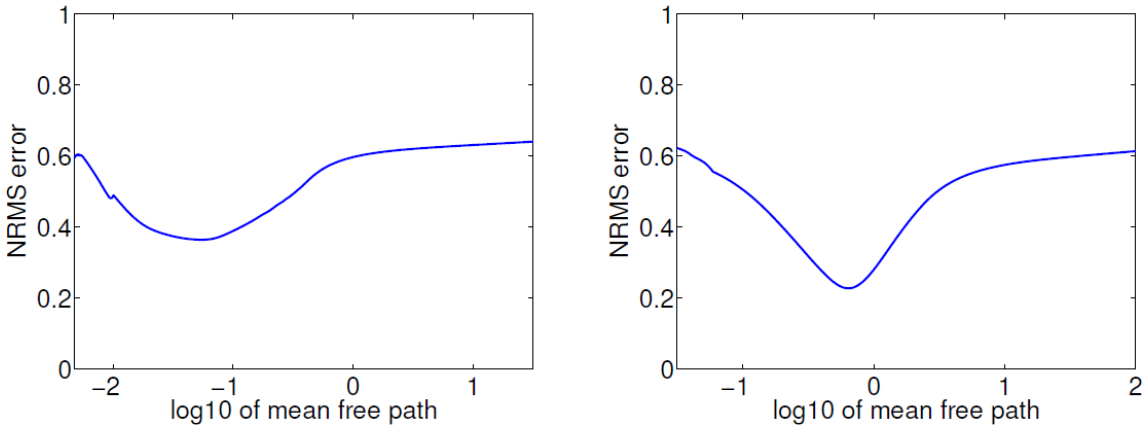

Figure 6-35: NRMS error of analytical fit of the scattered wave intensities from the stress change (left) and temperature change (right) experiments.

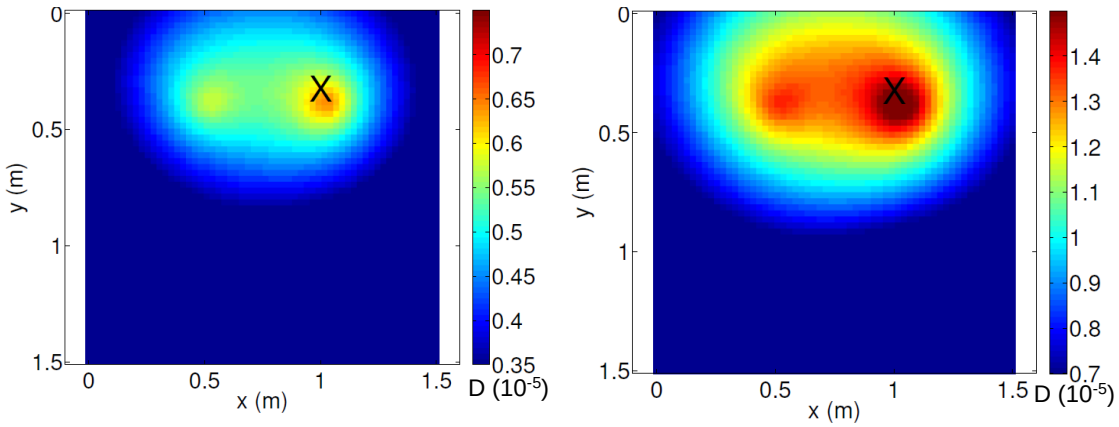

Figure 6-36: Inverted change (10^{-5} m^{-1}) due to stress loading from 5 kN to 10 kN (left) and from 5 kN to 15 kN (right). X: Loading position. Note: the color bar limits are doubled from left to right figure.

Note: The following section contains an issue concerning the temperature development in the specimen under test, which is not properly discussed here. While this does not affect the demonstration of the coda wave imaging presented there, one of the reviewers and the author agreed, that a more detailed discussion and further calculations would be of benefit. During this work, additional doubts have come up about some sensor readings. Again, this does not affect the main purpose of research presented in this section on this thesis. However, it must be addressed. For this reason, an addendum/erratum was added to the thesis before submitting the printed version in 2019 (chapter 11).

6.4.5 Concrete block for temperature changes

Figure 6-37 shows both the pictorial and schematic views of the concrete block we use for monitoring changes due to temperature changes. The experiment was conducted in an outdoor field south of Berlin that is owned by BAM. The concrete block ("all inclusive") has a dimension of $5 \cdot 4 \cdot 0.8$ m^3 consisting of a concrete mix C30/37 according to the European and German standards (DIN-EN 1992, DIN-EN 206). There is a heat cartridge H connected via a heating pipe from outside into the concrete block to induce local temperature changes within the block (Figure 10 bottom, cyan line).

We monitor the effect of the time-lapse local temperature changes using a total of 40 ultrasonic sensors that are attached at the side faces of the concrete block. We have ten sensors at each of the four sides of the concrete block. The sources for the monitoring ultrasonic waves are given as sensors S1-S20 while sensors R1-R20 are the recording sensors of the scattered (ultrasonic) waves (Figure 10 Bottom). The electrical setup of the temperature experiment is like the setup in the stress experiment (Figure 6-38). One multiplexer connects the transmitting sensors (S1-S20) to a rectangular transmitter, while a second multiplexer connects the receiving sensors to the Analog-to-Digital (A/D) converter prior to recording the scattered signals.

We pre-amplified the recorded signals by a factor of 60 to increase the signal-to-noise ratio especially for long receiver distances. In the temperature experiment, we use an ultrasonic source signal of a dominant frequency of 25 kHz. Figure 6-39 shows an example of the time-lapse signals (a baseline signal and a monitor signal after a temperature change) recorded by sensor R5 due to source signal from sensor S5.

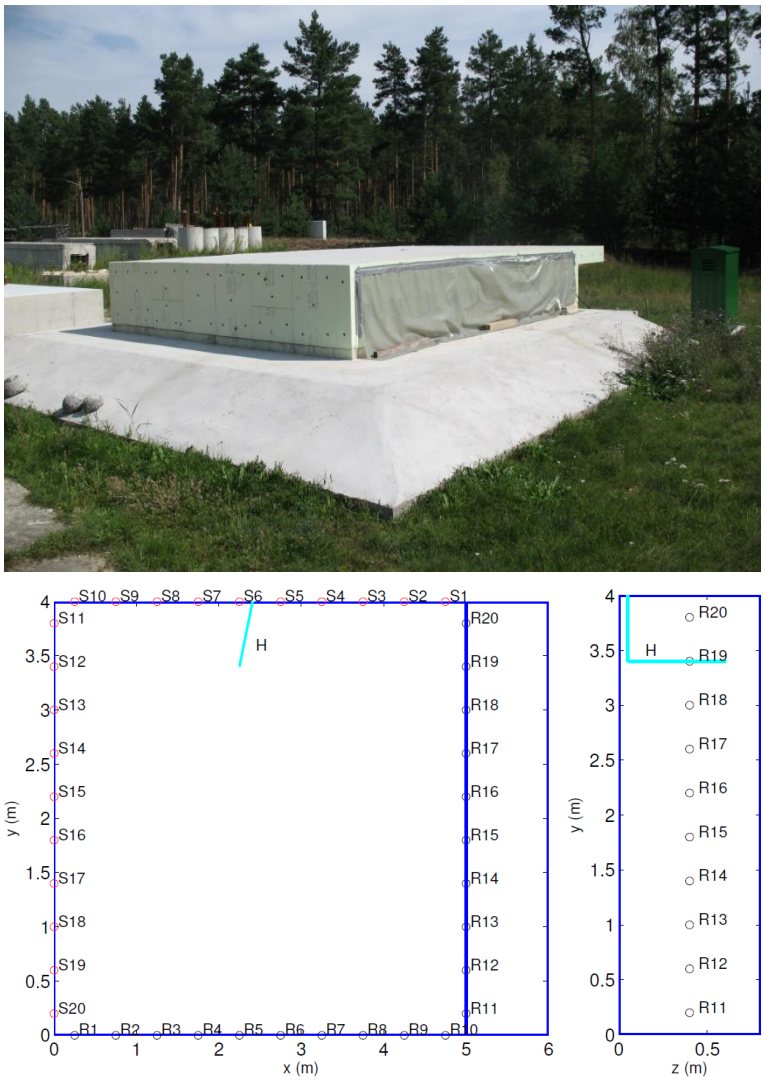

Figure 6-37: The pictorial (top) and the schematics (bottom) of the concrete block used for the time-lapse temperature monitoring experiment. The cyan line (H) indicates the heating cartridge probe.

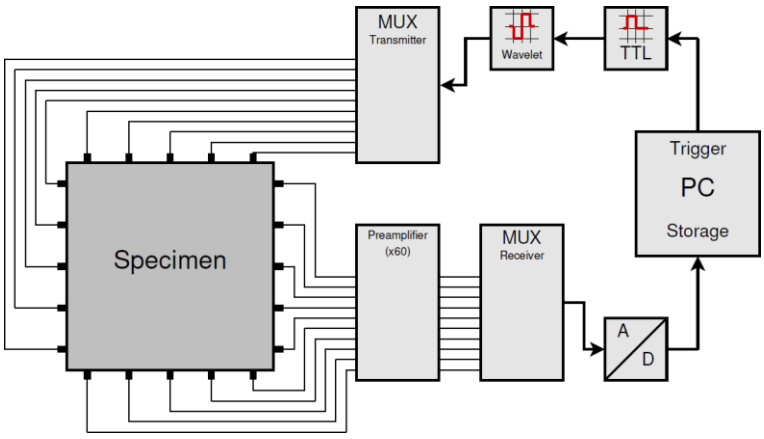

Figure 6-38: The electrical and mechanical setup of the stress loading experiment. Only half of the sensors are shown for clarity.

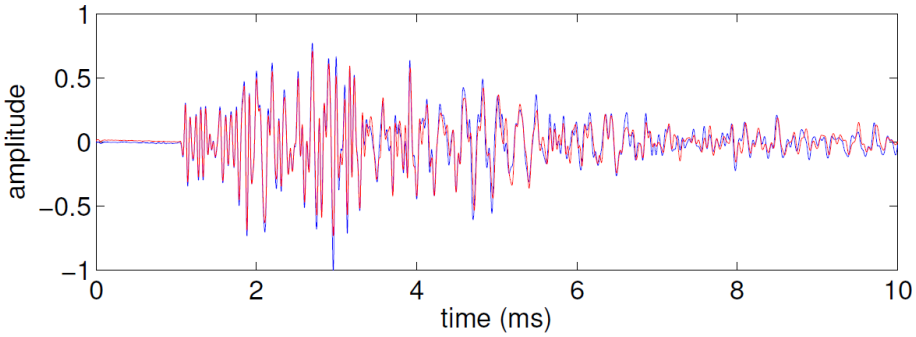

Figure 6-39: Typical coda signal recorded by sensor R5 due to a source at sensor S1 from the temperature experiment.

The fundamental solution of the heat transfer equation for an infinite 2D homogeneous medium[16] with a thermal conductivity k using a delta temperature forcing of maximum 1 °C is

$$T(\boldsymbol{x}, t) = \frac{1}{(4\pi\alpha t)^{3/2}} e^{-\|\boldsymbol{x}-\boldsymbol{x}_0\|^2/4\alpha t} \tag{6-20}$$

where α is the thermal diffusivity of the heated medium. The thermal diffusivity is given as $\alpha = k/(\rho\, C)$, where ρ is the density of the medium and C is the specific heat capacity of the medium. Figure 6-40 shows the temperature history of the time-lapse temperature experiment at the location of the heat cartridge. The temperature changes have been induced between 8:00 am on April 4th and 8:00 am on April 5th, 2014. The ambient mean temperatures measured were 11.37 °C on the 4th and 10.41 °C on the 5th of April. During the baseline measurement on 4th of April, the temperature of the heating cartridge was set at 100°C. However, at 11:11 am on 4th of April, the heating temperature was increased to 510 °C for a period of 2 hours before the cartridge was turned off. The measured temperatures after 1:11 pm on the 4th of April indicate that the temperature increased continuously. To estimate the temperature distribution across the heated concrete block at the time-lapse time (8:00 am on the 5th of April), we need the initial condition of the temperature distribution across the concrete, i.e., the temperature distribution across the concrete at 1:11 pm on the 4th of April. We do have point temperature measurements at the location of the heat cartridge and 0.2 m away from the heat cartridge within the concrete. The temperature measurements at the location of the heat cartridge and 0.2 m away from the heat cartridge are 510 °C and 470 °C, respectively, at 11:11 am on 4th of April. Let's assume that the temperature distribution at 1:11 pm on the 4th of April (the initial temperature condition $T_{IC}(\mathbf{x}, t)$ has a Gaussian characteristic defined as:

$$T_{IC}(\boldsymbol{x}, t) = 510\, e^{-\|\boldsymbol{x}-\boldsymbol{x}_0\|^2/2\sigma^2} \tag{6-21}$$

where σ is the width of the temperature anomaly during the initial temperature condition time. This assumed Gaussian characteristics ignores the effect of the reflecting boundaries. This is because we do not have the exact location of the temperature sensor 0.2 m away from the heat cartridge. Using the temperature measurement 0.2 m away from the heat cartridge, the estimated width of the temperature anomaly during the initial temperature condition time σ is 0.092 m.

Therefore,

$$T_{IC}(\boldsymbol{x}, t) = 510\, e^{-\|\boldsymbol{x}-\boldsymbol{x}_0\|^2/0.0168\ m^2} \tag{6-22}$$

[16] Corrected. 3D homogeneous medium in the original manuscript.

Assuming $T_{IC}(x, t)$ as the initial condition for the heat conduction, the solution of the heat conduction within the concrete at the time-lapse time $T_T(x, t)$ is

$$T_T(\boldsymbol{x}, t) = \int_V T_T(\boldsymbol{x} - \boldsymbol{x}', t) T_{IC}(\boldsymbol{x}', t) d\boldsymbol{x}' \tag{6-23}$$

$$T_T(\boldsymbol{x}, t) = \frac{510}{(4\pi\alpha t)^{3/2}} e^{-\|x - x_0\|^2/(4\alpha t + 0.0168)m^2} \tag{6-24}$$

The typical thermal diffusivity of concrete medium ranges from $5.5 \cdot 10^{-7}$ $m^2 \cdot s^{-1}$ to $1.9 \cdot 10^{-6}$ $m^2 \cdot s^{-1}$ (Mindess et al., 2003). Using equation (6-24) and assuming a thermal diffusivity α of 0.005 m^2/h for a concrete material, the approximate distribution of the temperature within the concrete material is shown in Figure 6-41. The temperature at the location of the heat cartridge is 463.84 °C during 8:00 am of the 5th of April, 2014. Therefore, the temperature curve in Figure 6-40 is expected to decrease to approximately 463.84 °C on 8:00 am of the 5th of April.

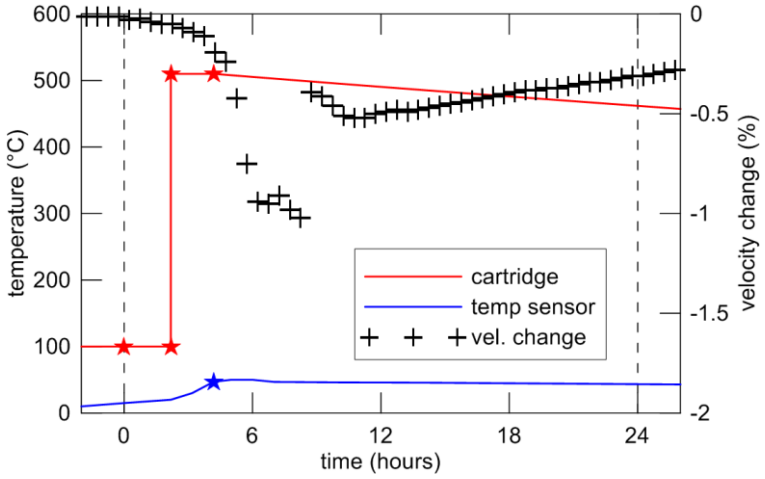

Figure 6-40: Measured temperature history curve (red and blue lines) of the time-lapse heating experiment with the estimated fractional velocity change from the sensor pair S6-R5 (black plus signs). The red and the blue lines correspond to the temperatures at the locations of the heating cartridge and 0.2 m away from the heating cartridge. Time zero corresponds to 8:00 am, April 4th.

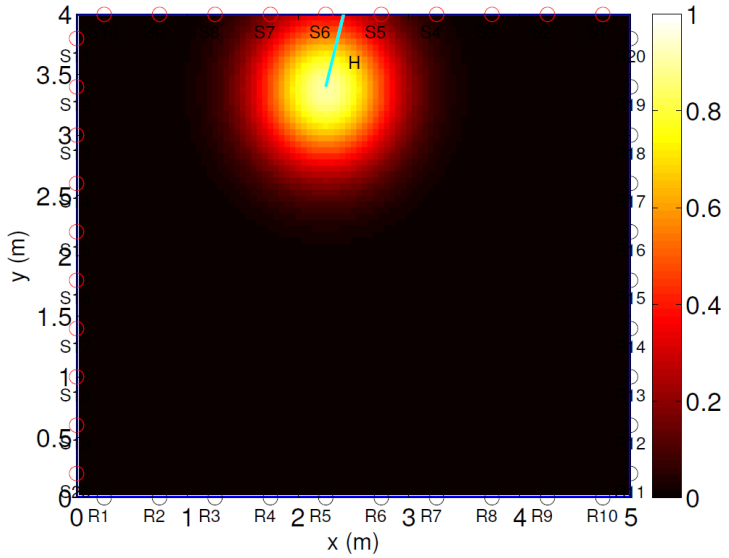

Figure 6-41: Normalized (by the maximum temperature) temperature distribution across the heated concrete medium at 5th of April (Figure 6-40) using equation (6-24). The cyan line is the heating cartridge probe.

6.4.5.1 Data analysis

Figure 6-42 shows the estimated decorrelation and velocity changes for the time-lapse heating experiment for the source-receiver pairs using the time-window shown with the black rectangle in the top panel of Figure 6-42. Here, the decorrelation and the velocity change were estimated for a specific time window using $D = 1\text{-}CC_{max}$ (equation (6-12)) and the stretching method (Hadziioannou et al., 2009), respectively. For each source-receiver pair, the time-window is centered at a delay time of 2.5 ms from the first arrival times. The decorrelation and velocity (negative) changes are spread out across the source-receiver pairs but there are larger decorrelation and velocity (negative) changes for the source-receiver pairs across the heat cartridge (lying between S5 and S6). The sources of changes for each sensor pairs are not restricted to the lines. The mean free path was estimated to be approximately 0.65 m and a mean free time of 0.163 ms using P-wave velocity for the temperature experiment. The time window used for the inversion extends beyond the mean free time.

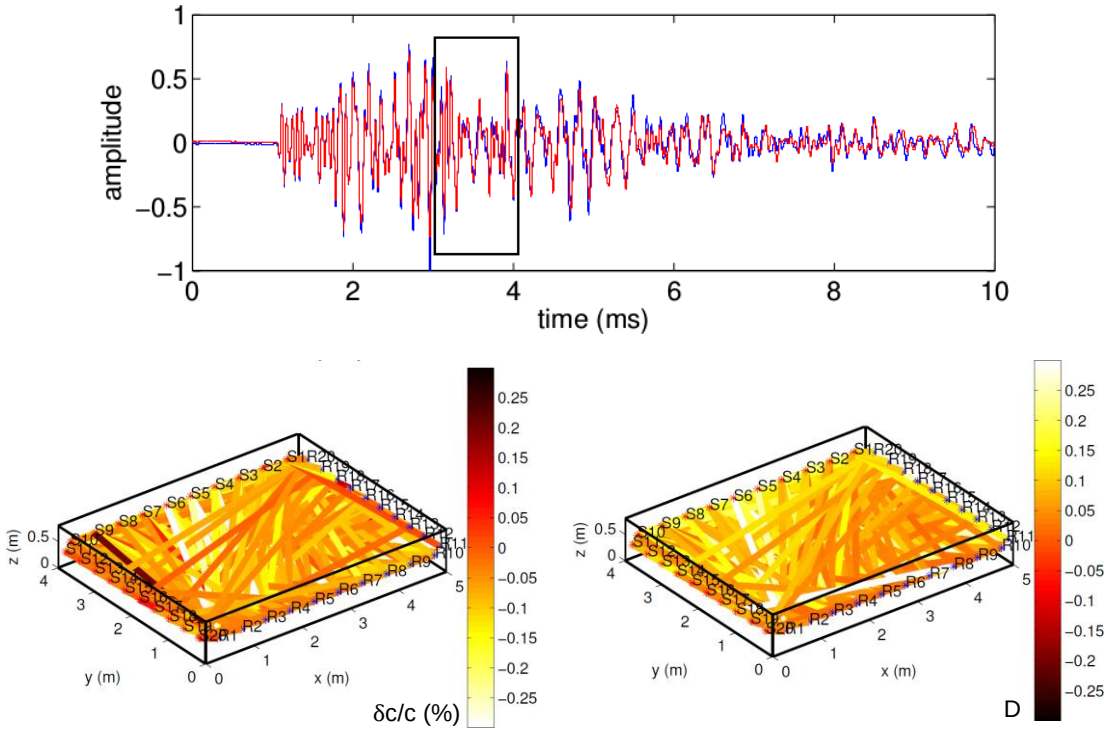

Figure 6-42: Top: Two signals (red, blue) measured for the same transducer pair at different temperatures. The black rectangle marks the time window used for further evaluation. Bottom: Time-lapse fractional velocity change and decorrelation due to temperature change within the concrete block. The colors of the lines between two sensors represent the estimated changes (fractional velocity change (left) and decorrelation (right).

6.4.5.2 Inversion results

Using the same algorithm as in the stress experiment, inversion was performed for the time-lapse change within the concrete block due to a localized temperature change.

Recordings from the same hour of the day (8:00 am of 4th and 5th of April for the baseline and time-lapse signals respectively) were used to reduce the effect of ambient temperature change. Figure 6-43 shows the imaged velocity change and the imaged change in the scattered cross-section in relation to the location of the heating cartridge (H). We use estimated fractional velocity change and decorrelation extracted from time-windows centered at around 2.5 ms after the first arrival (Figure 6-43 top). The figures show that using the estimated change from the coda time-window beyond the mean free time, we can

effectively localize the location of the temperature change induced by the heating within the concrete. The inverted change is slightly biased toward the edge of the concrete block due to the receivers located close to the edge. It is known that increasing temperatures induce negative velocity changes (Niederleithinger & Wunderlich, 2012; Naus, 2005). The negative velocity change in our experiment implies that at 8:00 am of 5th of April, 2014, the temperature within the concrete surrounding the heating cartridge has not dropped down to 100 °C or beyond. The hypothesis of an elevated temperature at 8:00 am of 5th of April, 2014 is supported by the modeled time-lapse temperature distribution within the medium in Figure 14 and the measured temperature history curve in Figure 6-40.

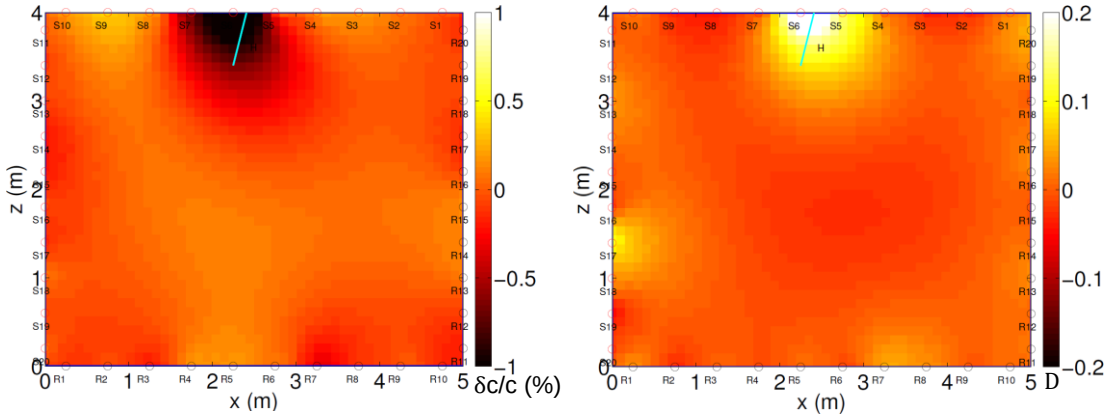

Figure 6-43: Inverted change due to localized temperature change due to a heating cartridge (cyan line) at H using the travel-time changes and decorrelation Left: inverted relative velocity change. Right: inverted change in the scattering cross-section (in m^2) using estimated decorrelation.

6.4.6 Conclusion

This study demonstrates the use of time-lapse ultrasound waves to monitor and locate changes induced within heterogeneous concrete blocks. To image the changes within the concrete blocks, we have used imaging algorithms based on the work of Pacheco & Snieder (2005) and Rossetto et al. (2011). The imaging algorithms allow for the use of either time-lapse fractional velocity changes or the decorrelation of the time-lapse ultrasound signals to image the change present within a scattering medium. To invert for the localized change within the concrete blocks, we solve a regularized least squares problem using linear conjugate gradient. We accurately localized the change within the concrete blocks using decorrelation and/or the fractional velocity changes estimated with coda lapse times beyond the mean free time of the concrete blocks. We have successfully monitored time-lapse localized changes within a concrete block due to an induced compressive load applied on opposite sides of the concrete block. It was shown, that just a small number of sensors is sufficient to localize the approximate volume affected by the stress change. It has been shown in accordance with other authors (e. g. Zhang et al., 2016) that using the decorrelation of coda waves in a tomographic approach yields better results than using velocity changes. In another concrete block, we monitored changes induced by elevated localized heat within the block induced by an embedded heating cartridge. We have seen that even using sensors not directly close to the cartridge temperature changes can be detected. The imaging method proposed here could localize the heat source almost correctly. The deviation is probably due to the sensor arrangement and the proximity to the edges.

It must be stated that the calculations of the sensitivity kernels that we need for imaging the time-lapse changes are still computationally expensive and several parameters have to be

set properly. The analytical computation of the sensitivity kernel (as presented here) so far is limited to rectangular, prismatic bodies and fails where monitoring complex concrete structures. Thus, further development is required to include the methodology into real time monitoring systems for complex concrete structures. An aspect of the further development might involve numerical computation of the sensitivity kernels with a prior model that satisfies the characteristics of the complex structure as shown by Kanu & Snieder (2015) and Kanu & Snieder (2014). However, there is no other method which can monitor subtle changes in concrete with just a few distributed sensors.

6.5 Laboratory experiments – time reversal[17]

6.5.1 Introduction

Several methods are used to evaluate acoustic signals generated by events in media such as water, rocks, metals or concrete. Most of them are summarized as acoustic emission methods (AE), which are used to localize and characterize the point of origin of the events. Sophisticated methods have been developed in seismology to localize and characterize earthquakes. Time reversal has been a topic of much research in acoustics due to its robust nature and ability to compress the measured scattered waveforms back at the source point in both space and time (Parvulescu & Clay, 1965; Fink, 1997; Anderson et al., 2008; Larmat et al., 2010). This has led to time reversal being applied in a wide variety of fields such as medicine, communication, ocean acoustics, seismology or nondestructive evaluation. However, continued work is being done to improve time reversal's ability to focus energy. Some newly developed techniques use an array of input transducers, measure the wavefield with an array near the desired focal spot, and then optimize the spatial and temporal focusing (Tanter et al., 2000; Tanter et al.; 2001, Montaldo et al., 2004; Vignon et al., 2006; Gallot et al., 2012; Bertaix et al., 2004; Roux & Fink 2000; Aubry et al., 2001; Jonsson et al., 2004). Other methods use an array of input transducers and optimize the temporal focusing at an output transducer (Daniels & Heath, 2005; Qui et al., 2006; Blomgren et al., 2008; Zhou et al., 2006; Zhou & Qui, 2006). The capability to locate acoustic emissions in concrete was show by Sänger et al. (2011) using simulated data.

Here, evaluation experiments are presented to compare conventional time reversal to an improved variant which uses deconvolution. We explore the application of deconvolution, which is a primitive though robust version of the inverse filter (Tanter et al., 2000; Gallot et al., 2012), to calculate the optimal signal for backpropagation. The ultrasound experiments are performed on a concrete block which has sources embedded within. Instead of using a large array of receivers, the experiments use only a single receiver to record the scattered waveforms. time reversal and deconvolution is then applied to the measured scattered waveforms. The calculated signals are then propagated from a transducer on the surface of the block back into the medium and recorded at the original source location transducer. By this experiment, the capabilities of time reversal and deconvolution to focus the measured waveforms at a point in both space and time have been explored and compared. It is shown that deconvolution improves significantly the temporal focus compared with time reversal. Two different experiments to study the robust nature of deconvolution by investigating the effect of changing the stabilization constant used in the deconvolution and the impact multiple sources have upon deconvolutions' focusing abilities are presented as well.

It was shown previously that deconvolution improves temporal focusing (Ulrich et al., 2012). It was then demonstrated by Douma et al. (2013) and Douma & Snieder (2014) that

[17] This section was edited from Douma et al., 2015.

improved temporal focusing leads to improved spatial focusing as well for both the acoustic and elastic case. Douma et al. (2013), Douma & Snieder (2014) and Ulrich et al. (2012) only used a single source within their experiments and numerical studies. However, within the earth or concrete, multiple fractures may be generated within the time window being recorded. Therefore, the goal of this paper is to evaluate the robust nature and focusing capabilities of deconvolution when multiplied source wavefields are generated within a concrete block. Due to deconvolution allowing one to focus an arbitrary source function a source location (Ulrich et al., 2012), one could potentially use deconvolution to improve the characterization of the earth or concrete through virtual sources (Snieder et al., 2006; Mehta et al., 2008a; Mehta et al., 2008b; Wapenaar et al., 2012; Behura & Snieder, 2013).

6.5.2 Deconvolution theory

Time reversal is a process used to compress the measured scattered waveforms at a point in both space and time to ideally a Dirac delta function $\delta(t)$. It uses the recorded impulse response which can be represented by a Green's function G_{AB} that accounts for the wave propagation between two points A and B. Time reversal then simply reverses the signal in time and propagates it back from the receiver location into the same medium. By doing so, one expects the energy to focus at the source location. The time reversal process can be represented by the following equation,

$$\int_{-\infty}^{\infty} G_{AB}(\tau) G_{AB}(\tau - t) d\tau = \delta(t) \tag{6-25}$$

where reciprocity was used to replace the Green's function G_{BA} with G_{AB}. Per equation (6-25), the time reversal process, which is equivalent to the autocorrelation of $G_{AB}(t)$, should ideally yield a delta function. In practice, however, one cannot truly recreate a Dirac delta function focus due to one or more conditions, necessary to satisfy equation (6-25), not upholding. For it to work perfectly, one must record for infinite time, Green's functions are assumed to have a flat, infinite bandwidth, the medium is not attenuative, and one must have full coverage of the wavefield at a surface surrounding the points A & B. These requirements are not satisfied during an experiment. This led us to explore the application of deconvolution.

We can rewrite equation (6-25) in a more generalized form (using a convolution notation, rather than the integral form) as

$$F(t) = g(t) * R(t) \approx \delta(t) \tag{6-26}$$

where * denotes convolution, F(t) is the focal signal or source reconstruction, $R(t) = G_{AB}(t)*S(t)$ is the recorded signal measured at the receiver location B from the initial source propagation where S(t) represents the source as a function of time, and g(t) is the signal to be backpropagated for focusing. We can go from equation (6-25) to (6-26) because we only investigate signals between the two points A and B, and remove the Green's function notation to indicate we do not have infinite bandwidth. Thus, we remove some of the unrealistic conditions that are required for Eq. (6-25) to hold. For a time reversal process, the signal for backpropagation is purely the time reversed recorded signal: $g(t) = R(-t)$. Our goal is to calculate the optimal signal g(t) such that the focal signal F(t) approximately equals a Dirac delta function $\delta(t)$.

Deconvolution equates to inverse filtering by transforming to the frequency domain, thus Eq. (6-25) becomes

$$F(\omega) = g(\omega) G(\omega) S(\omega) \approx 1 \tag{6-27}$$

Equation (6-27) is used to solve for g(ω),

$$g(\omega) = \frac{1}{G(\omega)S(\omega)} = \frac{G(\omega)^* S(\omega)^*}{|G(\omega)S(\omega)|^2} \tag{6-28}$$

where * denotes complex conjugation. Equation (6-28) is, however, unrealistic for experimental use if there is a limited bandwidth, significant background noise, or more specifically, if $R(\omega) = 0$ at any frequency. To avoid the associated singularity, we add a parameter to the denominator of the last term of equation (6-28) to ensure that we never divide by zero. Hence equation (6-27) becomes,

$$g(\omega) = \frac{G(\omega)^* S(\omega)^*}{(1 + \gamma)|G(\omega)S(\omega)|^2} \tag{6-29}$$

The quantity γ, which is sometimes referred to as the water level parameter (Clayton & Wiggins, 1976), is a constant chosen to optimally reduce the effect of noise introduced through the deconvolution procedure. This quantity may equal any positive number where deconvolution could fail due to noise. Here, γ = 0.9 was used for all experiments. This value was chosen based on optimizing the focus energy in a process like that developed by Clayton and Wiggins (1976). Equation (6-29) gives the solution for g(ω). By inverse Fourier transform of this result on obtains the "optimal" deconvolution signal in the time domain to be backpropagated such that one gets an approximate Dirac delta function focus.

6.5.3 Experimental setup

A laboratory experiment was created and run in the Civil Engineering lab of Colorado School of Mines. A 30 × 30 × 37 cm^3 concrete block was cast from 72 kg Quickcrete mix (No. 1101, max aggregate grain size < 4 mm), with about 60 l of water and 5 kg of additional gravel (5 mm – 15 mm grain size). The concrete used has a nominal compressive strength of 27.9 MPa after curing for 28 days in accordance to ASTM C39/ASTM 387. The block contains only minimal reinforcement as shown in Figure 6-44a. Three ultrasonic piezo transducers (type Acsys SO807, center frequency 60 kHz, labeled 'ES' in Figure 6-44) were attached to the reinforcement to cast them within the concrete block. These sources (transducers) are visible in Figure 6-44a. These sources were oriented differently to generate more complex waveforms and to study the effect of varying source orientation. Source 3 was oriented perpendicular to the other two sources. Broadband Acsys sensors type 1803 (center frequency about 100 kHz, labeled 'PT' in Figure 6-44) were used as external transducers. They are piezo-based and feature a spring-loaded 2 mm diameter ceramic tip for contact to the concrete. These transducers are most sensitive in the direction perpendicular to the surface they are attached to. The transmitted signal is generated by a custom-made rectangular signal generator/amplifier (BAM US in Figure 6-44). It is triggered by an impulse which is issued by our data acquisition device (National Instruments model 6366). The recorded signals at the external sensor are first high pass filtered at a frequency of 1 kHz and amplified by a Stanford Research low noise preamplifier (SR 566) before being digitized and recorded. This was necessary to remove low frequency noise present in our data. The work flow and set up used for acquiring the data is shown in Figure 6-44b. Additionally, to reduce noise, time averaging by stacking over 144 runs was used.

For backpropagation, the setup is reversed. The BAM US device is removed. The transmitter signal generator is replaced by the digital/analog converter integrated in the data acquisition device, sending the computed, time reversed/deconvolved waveforms to the

external sensor. The embedded sensor is used as receiver, again using the preamplifier before AD conversion and recording. This reversed set up is shown in Figure 6-44c. A sampling frequency of 2 MHz and 20,000 samples per trace (10 ms recording time) were used. A 4,000 sample (2 ms) pre-trigger interval was set. The reason a longer pre-trigger time was used is because it was shown by Ulrich et al. (2012) that with a longer pre-trigger time, we could improve the focus for deconvolution. Amplitude resolution is 16 bit. True zero time of the transmitter could be identified by electromagnetic crosstalk between transmitter and receiver cables, generating a small but easy to recognize impulse in the receiver data. The laboratory contained other noise due to multiple experiments being run simultaneously. Due to a high noise lab environment and a lack of a power amplifier for the backpropagated transmitter signal, we apply an additional 2 kHz high-pass Butterworth filter on all data.

To test the stability of deconvolution for different values of the regularization parameter γ, we run the exact same experiment as for a single source described above and shown in Figure 6-44b. Once the signal was recorded, we applied deconvolution multiple times with different gamma values to generate the different signals to be backpropagated. We then ran the same workflow as shown in Figure 6-44c for each deconvolution signal separate, recording the focused wavefield at the source location each time.

For multiple sources, we executed the workflow described above and shown in Figure 6-44b three times (once for every source). This was necessary because we did not have the equipment capabilities in this laboratory to generate a source function at all three source locations at different onset times. We recorded these three generated wavefields separately and then superimposed them. Due to the experiment being run separately three times, each recorded signal was normalized independently. This caused our recorded signals for all three sources to vary between amplitudes of −1 and 1. Thus, it destroyed the relative amplitude variation one would expect for three different sources at different locations and orientations. Once superimposed, time reversal or deconvolution was applied, and we carried out the same back propagation workflow as shown in Figure 6-44c. During the backpropagation, one restores the relative amplitudes in the focus achieved because of reciprocity.

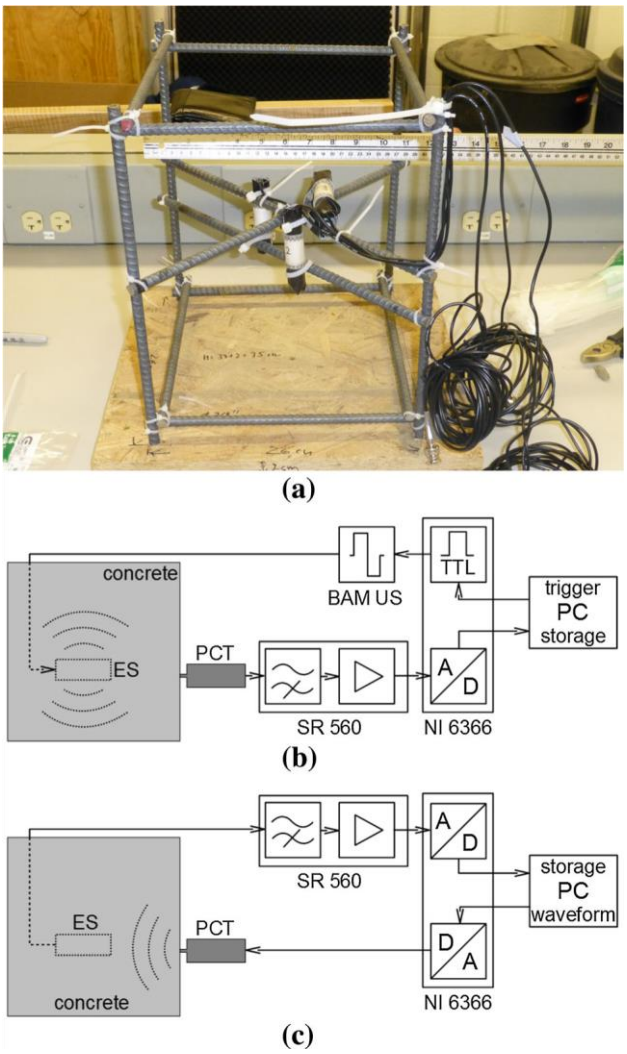

Figure 6-44: Figures and diagrams indicating experimental set up and workflows used during acquisition and backpropagation. Note, the diagrams indicating the workflows are meant to show the tools used during acquisition and backpropagation and do not accurately describe the interior of the concrete for every experiment in this paper. (a) Source set up and reinforcement to be placed within the concrete block, (b) acquisition workflow, (c) backpropagation workflow.

6.5.4 Data analysis

6.5.4.1 Single source experiment

The purpose of this experiment is to study the capabilities of time reversal and deconvolution to focus the measured waveforms at a point in time. The experiment began with propagating a defined 60 kHz source function from the embedded source towards the external receiver. The receiver's direction of measurement was perpendicular to the direction of source emission. Once our wave field was recorded at the single receiver, time reversal or deconvolution was applied to calculate the back-propagating signals.

For a single source, deconvolution ideally achieves an improved temporal focus. This is due to there being a single term in the denominator as shown in Equation (6-29), which leads to the following

$$g(\omega)G(\omega) = \frac{G(\omega)G(\omega)^* S(\omega)^*}{(1+\gamma)|G(\omega)S(\omega)|^2} \approx \frac{1}{S(\omega)} \qquad (6\text{-}30)$$

where G(ω) represents the Green's function describing the propagation between source and receiver, $S(\omega)$ represent the source function in the frequency domain, and g(ω) the signal we are trying to solve for with deconvolution. Equation (6-30) should approach 1/S(ω) as γ approaches zero. Therefore, the focus achieved using deconvolution approaches an optimal reconstruction of the inverse of the source function and not necessarily a Dirac delta function. When the source function is a delta function, S(ω) is constant, this leads to a delta function at the focal point.

The deconvolution and time reversal signals were then backpropagated from the transducer on the surface of the block into the same medium and recorded at the original source location transducer. Figure 6-45 shows the refocused waves recorded at the source location where Figure 6-45a is the temporal focus achieved using time reversal while Figure 6-45b represents the temporal focus achieved using the deconvolution calculated signal. The temporal focus achieved using time reversal has significant side-lobes away from the time of focus; the temporal focus achieved using deconvolution has suppressed most of these side-lobes and has produced a better focus. To quantify this improvement, we calculate the amount of energy in a 0.02 ms window around the time of focus compared to the total energy of the signal. The temporal focus achieved using time reversal only had 41 % of the total energy within this window while deconvolution's temporal focus had 80 % of the total energy within this window. Thus, deconvolution can generate a significantly better temporal focus than time reversal. Our source function used wasn't a Dirac delta function, but deconvolution still improved the focus significantly as it improved the reconstruction of our source function. Once we had shown that deconvolution could improve the focus at a point in time, we continued our experimental studies to investigate the robust nature of deconvolution.

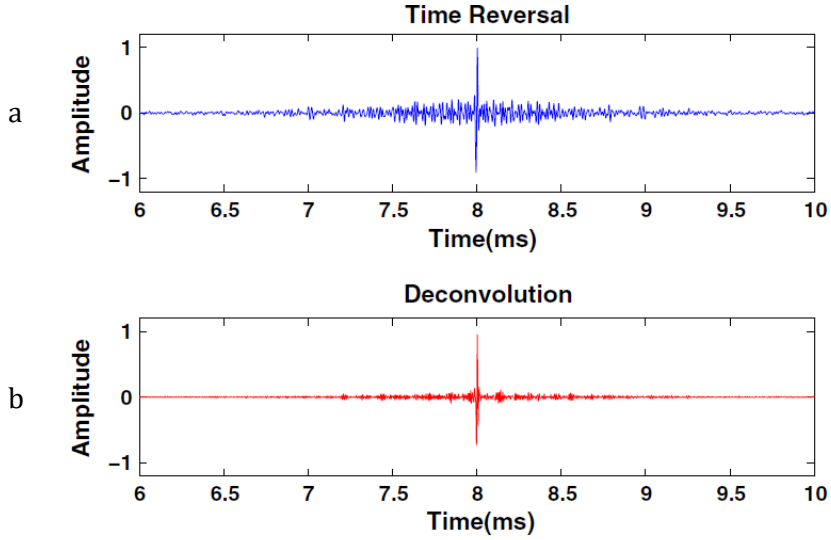

Figure 6-45: Normalized temporal focus measured at the embedded source location using (top panel) time reversal, and (bottom panel) deconvolution for a single source and single receiver set up.

6.5.4.2 Regularizing the deconvolution

The purpose of this experiment was to study the robust nature of deconvolution by changing the location of the receiver and investigating the effect of regularizing the deconvolution through the parameter used in Equation (6-29). This experiment started the same way as our previous single source experiment. We first propagated a defined 60 kHz source function from the embedded source towards the external receiver. For this experiment, the receiver's direction of measurement was parallel to the direction of source emission. The recorded signal was then deconvolved using various values of γ which was the constant scalar number used to characterize the regularization term defined in

Equation (6-29). These calculated deconvolved signals were propagated back into the medium from the receiver location and recorded at the source transducer.

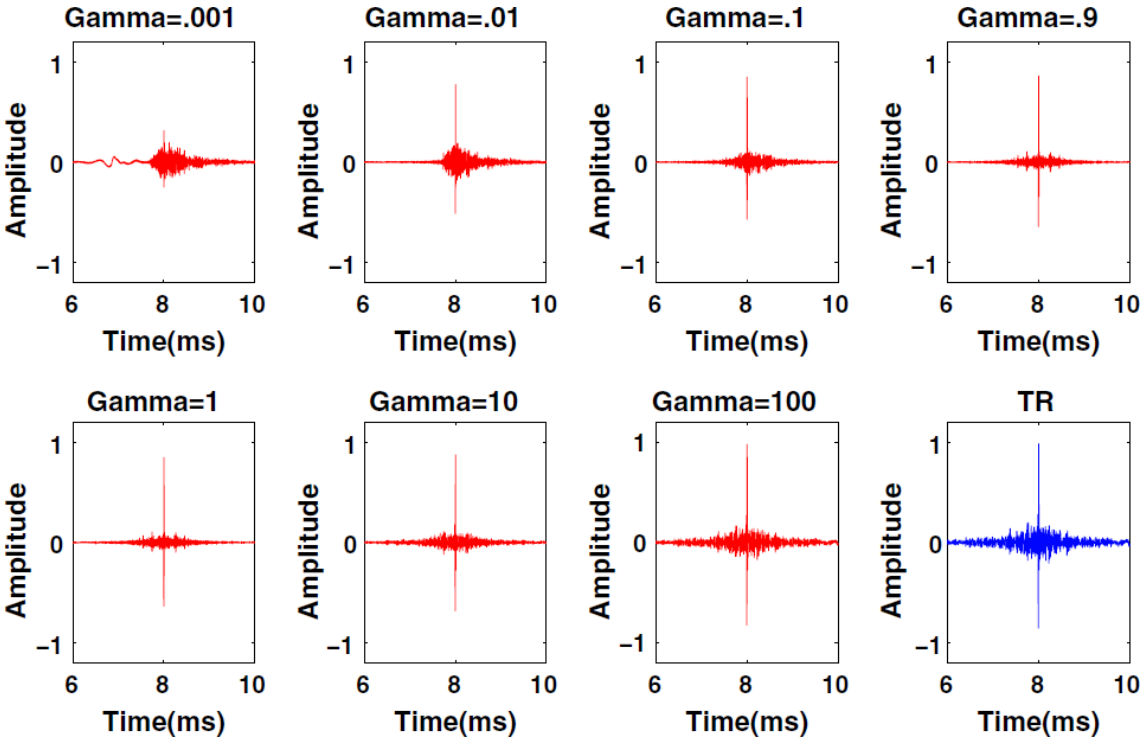

Figure 6-46: Normalized temporal focus measured at the embedded source location using different values for γ in the deconvolution (shown in red) and time reversal (shown in blue).

Theoretically, we would expect the focused wavefield to contain significant amount of noise at low γ values. As γ increases, the temporal focus is expected to improve because we reduce the effect of noise and force our signal to generate a better approximate Dirac delta function focus. However, if γ becomes too large, one approaches the temporal focus achieved using time reversal. This is as follows: For time reversal, g(t) = R(−t), therefore, g(ω) = R(ω)*. If γ ≫ 1, Equation (6-29) reduces to

$$g(\omega) = \frac{1}{\gamma |G(\omega)S(\omega)|^2} G(\omega)^* S(\omega)^* = \frac{1}{\gamma |G(\omega)S(\omega)|^2} R(\omega)^* \qquad (6\text{-}31)$$

which implies that our deconvolved signal is just a scaled version of the time reversed signal.

Figure 6-46 shows the normalized focused wavefield at the source location for time reversal and deconvolution for different values of γ. For this experiment, we quantified the temporal focus the same way as the previous experiment with the identical window size of 0.02 ms used. The optimal deconvolution's temporal focus was 79 % (for a γ value of 0.9) while time reversal had a temporal focus of 47 %. We would not expect to see the exact same temporal focusing numbers as in our single source experiment because we changed the direction of displacement we record and the distance between the source and receiver.

Figure 6-47 highlights the effect of gamma by showing the temporal focus as a function of γ. If γ becomes small, the temporal focus achieved decreases. However, as γ becomes large, the temporal focus approaches time reversal's temporal focus of 47%. The experiment showed that the optimal value to be γ = 0.9. However, even for different γ values, one still achieves some form of a temporal focus as shown in Figure 6-46.

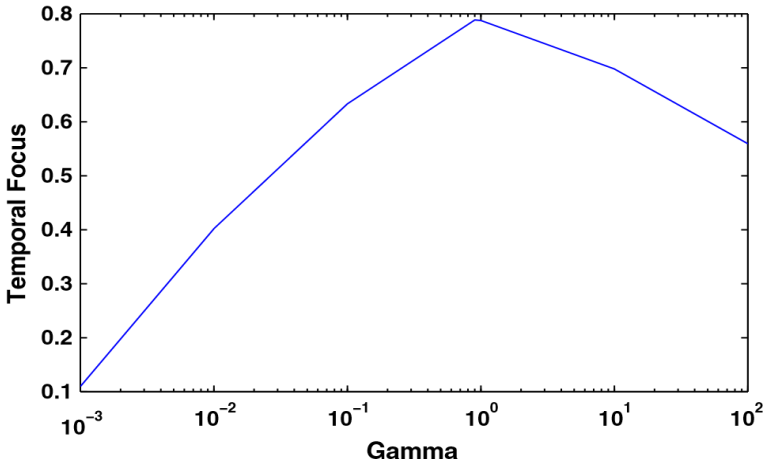

Figure 6-47: The temporal focus, defined as the amount of energy in a 0.02 ms window around the time of focus, compared to the total energy of the signal, as function of γ. High temporal focus indicates most of the energy is compressed at the time of focus.

6.5.4.3 Multi source experiment

The purpose of this experiment was to study the effect of multiple sources when using deconvolution. We began by emitting the same 60 kHz source function from different source transducers within the concrete block at different onset times. The experiment was repeated three times to record each source wavefield separately which normalized the recorded signals independently. The employed normalization caused our signals for all three sources to vary between amplitudes of −1 and 1. The three recorded wavefields due to the three sources were then superimposed before time reversal or deconvolution was applied. Figure 6-48 shows the superimposed wavefield. Note the complexity of the wavefield due to scattering within the concrete sample.

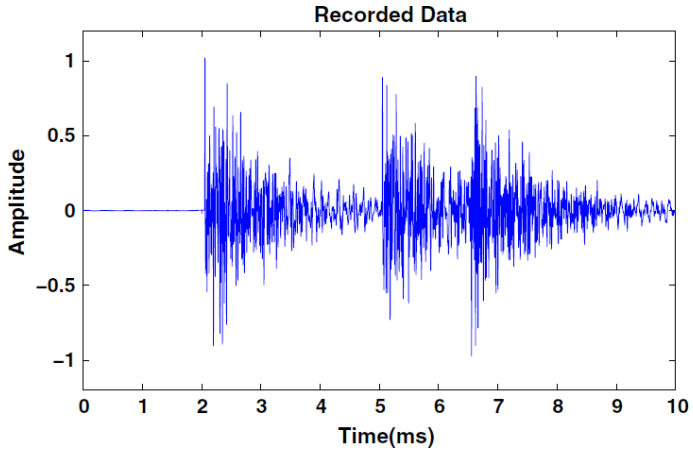

Figure 6-48: Recorded scattered waveforms at the receiver location due to three source wavefields being emitted at different times.

Due to the complicated nature of the recorded signal, one can assume that the cross-correlation of each source wave field is negligible:

$$G_i G_j^* \approx 0 \; for \; i \neq j \tag{6-32}$$

where G_i for i = 1,2,3 is the Green's function characterizing the source wavefield for sources 1, 2, or 3. Equation (6-32) is crucial in explaining why deconvolution is stable for multiple sources.

Time reversal and deconvolution are applied to the superimposed signal consisting of the three source wavefields to generate our time reversal and deconvolution signals shown in Figure 6-49. The deconvolved signal differs from the time reversal signal in its acausal nature, due to our pre-trigger time, where deconvolution adds information past 8 ms while time reversal has zero amplitude after 8ms. Additionally, the three different source wavefields are still clearly visible in the deconvolution signal. Below, we demonstrate why deconvolution can focus the wavefield due to multiple source at each source location.

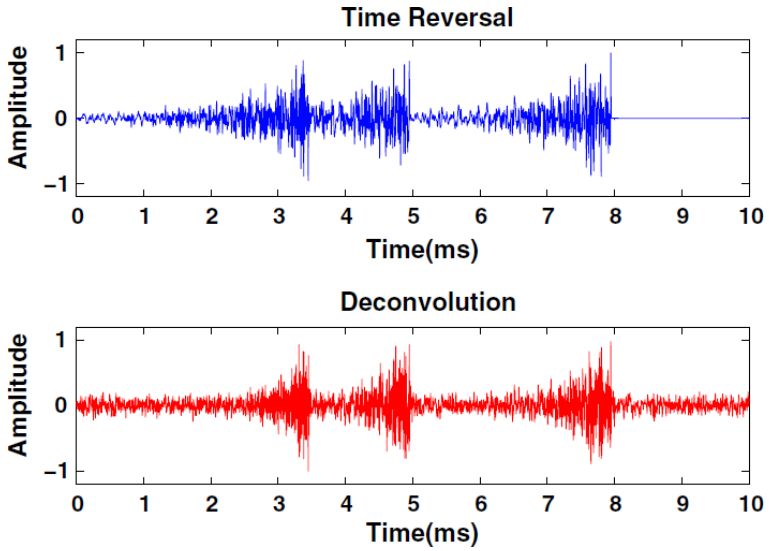

Figure 6-49: Back propagation signals calculated using Time reversal (top panel) and deconvolution (bottom panel). These signals are backpropagated into the medium for the multi-source experiment.

If there are three sources, the recorded signal in the frequency domain is given by

$$R(\omega) = G_1S_1 + G_2S_2 + G_3S_3 \tag{6-33}$$

where $R(\omega)$ is the recorded signal in the frequency domain, and the subscripts indicate the source transducer used. The inverse signal obtained by deconvolution is given by

$$\begin{aligned} D_t(\omega) &= \frac{1}{G_1S_1 + G_2S_2 + G_3S_3} \\ &= \frac{1}{G_1S_1 + G_2S_2 + G_3S_3}\frac{(G_1S_1 + G_2S_2 + G_3S_3)^*}{(G_1S_1 + G_2S_2 + G_3S_3)^*} \end{aligned} \tag{6-34}$$

We simplify the above solution and add the regulation term $\epsilon = \gamma_{mean}|G(\omega)S(\omega)|^2$ to get

$$D_t(\omega) = \frac{(G_1S_1 + G_2S_2 + G_3S_3)^*}{|G_1S_1|^2 + |G_2S_2|^2 + |G_3S_3|^2 + Crosstalk + \epsilon} \tag{6-35}$$

Where Crosstalk = $G_1S_1G_2^*S_2^* + G_1S_1G_3^*S_3^* + G_2S_2G_1^*S_1^* + G_2S_2G_3^*S_3^* + G_3S_3G_1^*S_1^* + G_3S_3G_2^*S_2^*$ and $D_t(\omega)$ represents the deconvolved signal when the recorded signal contains three source wavefields.

If we recorded each sources' wavefield separately and applied deconvolution first before the superposition of the wavefields, we would get:

$$D_s(\omega) = \frac{(G_1S_1)^*}{|G_1S_1|^2 + \epsilon_1} + \frac{(G_2S_2)^*}{|G_2S_2|^2 + \epsilon_2} + \frac{(G_3S_3)^*}{|G_3S_3|^2 + \epsilon_3} \tag{6-36}$$

where $D_s(\omega)$ represents the deconvolved signal when deconvolution is applied before superposition. One might expect that for a real scenario, where multiple sources are

present, deconvolution would break down due to the influence of crosstalk. Because the recorded wavefields generated by each source are extremely complex, as shown in Figure 6-48, terms such as $G_1G_2^*$ are small (Equation (6-32)). Therefore, the influence of the crosstalk terms is minimal, and we can assume it vanishes. This provides us with the following solution that relates $D_s(\omega)$ to $D_t(\omega)$:

$$\begin{aligned} D_s(\omega) = & \frac{(G_1S_1)^*}{|G_1S_1|^2+\epsilon_1} + \frac{(G_2S_2)^*}{|G_2S_2|^2+\epsilon_2} + \frac{(G_3S_3)^*}{|G_3S_3|^2+\epsilon_3} \\ \approx & \; 3\frac{(G_1S_1+G_2S_2+G_3S_3)^*}{|G_1S_1|^2+|G_2S_2|^2+|G_3S_3|^2+\epsilon} = 3\,D_t(\omega) \end{aligned} \tag{6-37}$$

where we assume $|G_1S_1| \approx |G_2S_2| \approx |G_3S_3|$.

Figure 6-50 shows that the approximation (6-37) holds. Figure 6-50 demonstrates that after normalizing $D_s(t)$ and $D_t(t)$, one can note that there does not seem to be an obvious difference between $D_s(t)$ and $D_t(t)$. Therefore, one may conclude Thus, the crosstalk term may be ignored, and deconvolution is stable and able to focus the wavefield due to multiple sources at each source location. We could do this calculation because we recorded each source wavefield separately.

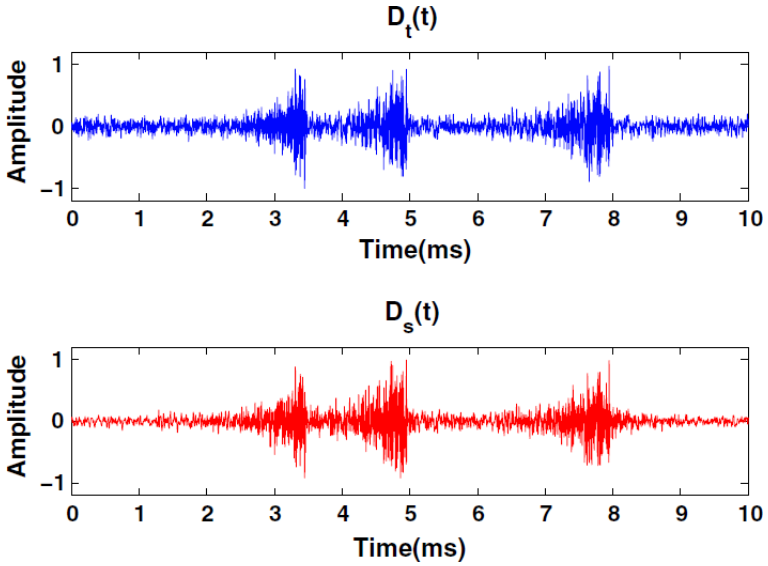

Figure 6-50: Comparison of deconvolution signal calculation. Top panel shows the deconvolved signal after applying deconvolution to the superposition of the three recorded wavefields $D_t(t)$. Bottom panel shows the deconvolved signal after applying deconvolution to the three recorded signals before adding them to each other $D_s(t)$. All signals are normalized

One does not need to have priori knowledge of the source signal to apply deconvolution and detect the sources. One can essentially modify the focus to be any arbitrary source function as shown in Ulrich et al. (2012). We have just assumed the source function to be a Dirac delta function for these experiments.

To keep the experiment realistic, we back propagated the deconvolved signal which was calculated after the superposition of the three separate wavefields. Figure 6-49 shows the signals calculated using time reversal and deconvolution which are propagated back into the medium from the receiver location. We then used the transducers within the concrete block as our receivers. Figure 6-51 shows the focused wavefields at each of the three sources for time reversal, shown in the top panels, versus deconvolution, shown in the bottom panels. For sources 1 and 2, deconvolution compresses the side lobes substantially better

than time reversal. However, for source 3, deconvolution does not significantly improve the focus compared to time reversal.

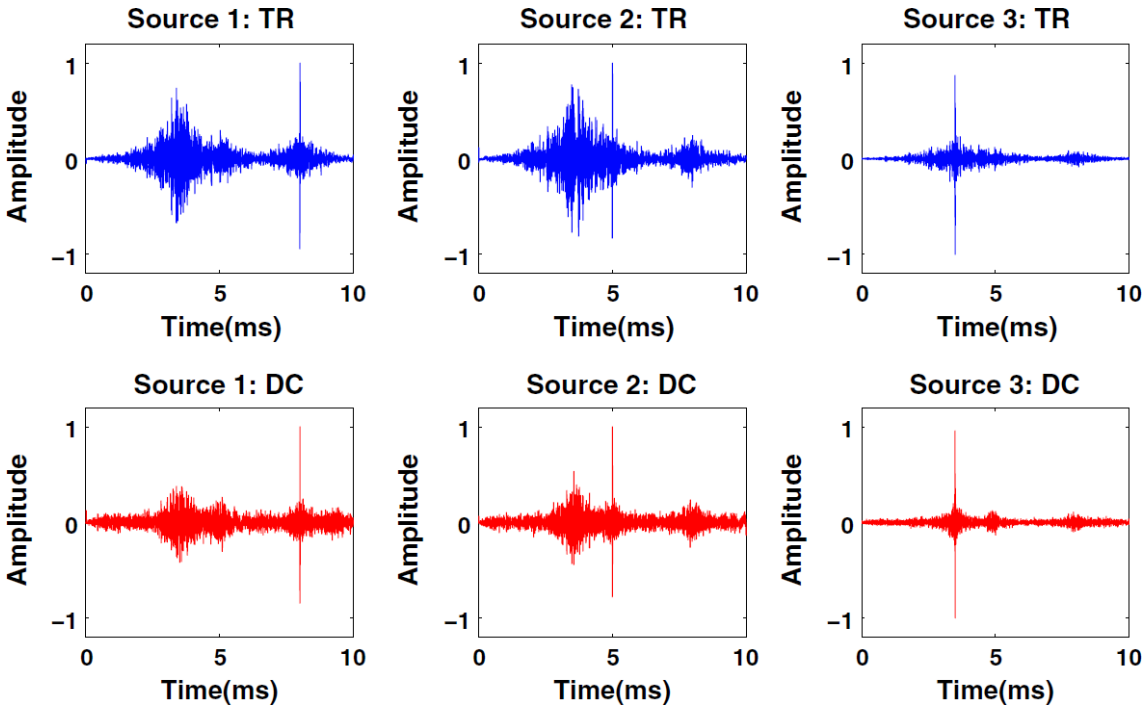

Figure 6-51: Temporal focus measured at the three embedded source location using (top panels) time Reversal's signal, and (bottom panels) deconvolution's D_t (t) signal and back propagating it from the transducer on the surface of the concrete sample.

The orientation of our sources is an important factor. Sources 1 and 2 were oriented perpendicular to source 3, and as a result the recorded waves excited by source 3 are stronger than those excited by sources 1 and 2. However, as previously stated, we ran each source wavefield propagation separately which normalized the recorded signals independently causing the amplitudes of each recorded source wavefield to vary between amplitudes of −1 and 1. Thus, our superimposed signal shown in Figure 6-48 does not show a higher amplitude for the source 3 wavefield. However, when we back propagate our time reversal and deconvolution wavefield, due to reciprocity, the source 3 wavefield focus will have a higher amplitude. This causes the crosstalk terms to be negligible for the source 3 focus because

$$|G_3(\omega)| \gg |G_1(\omega)| \text{ and } |G_3(\omega)| \gg |G_2(\omega)| \tag{6-38}$$

Under these conditions, Equation (6-35) reduces to

$$D_t(\omega) = \frac{(G_3 S_3)^*}{|G_3 S_3|^2 + \epsilon_3} \tag{6-39}$$

which is what we had before. Figure 6-52 shows that Equation (6-39) holds because, for source 3, the focus has significantly higher relative amplitude than the crosstalk terms. For sources1and2, the maximum amplitude of the crosstalk is closer to the maximum amplitude of its focus.

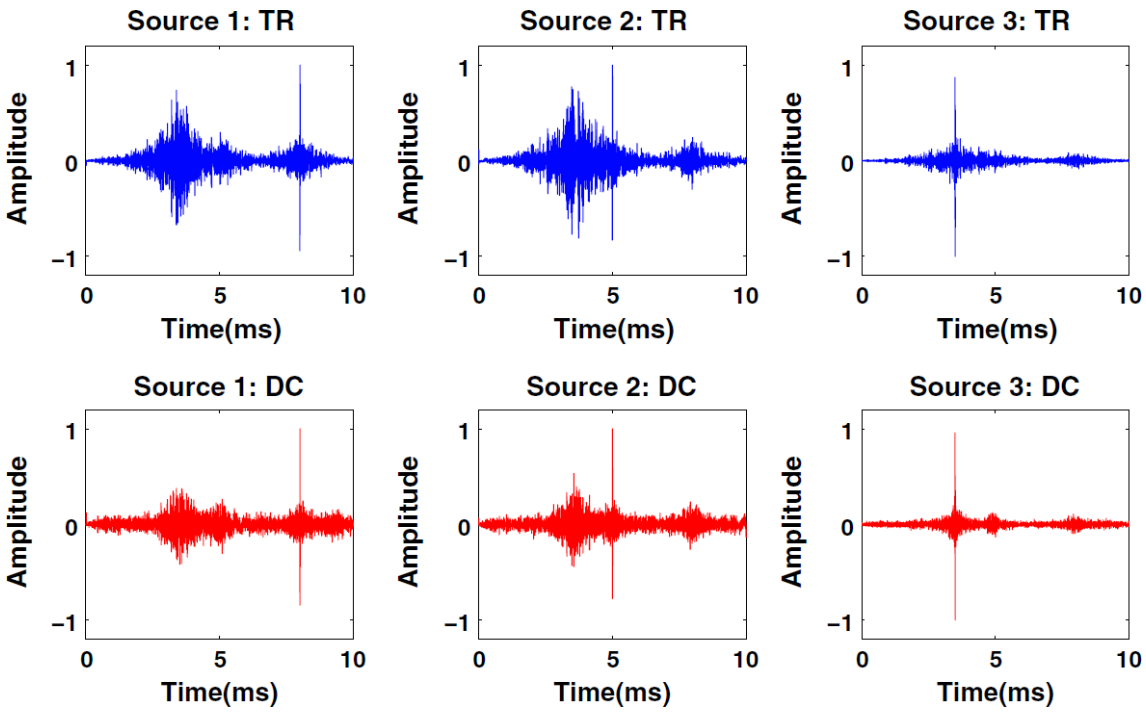

Figure 6-52: Temporal focus measured at the three embedded source locations using (top panels) time reversal's signal, and (bottom panels) deconvolution's signal and back-propagating it from the transducer on the surface of the concrete sample.

In conclusion, for multiple sources, deconvolution can focus the energy at the source location at the correct time. It is arguable whether time reversal or deconvolution is better in generating a focus. However, the experiment does prove the robust nature of deconvolution in that it does not fail under the condition of multiple sources.

The purpose of using time reversal and deconvolution processes is to generate a signal such that it will focus at the source location. One can use this feature of the methods for a range of applications to characterize the medium. For example, after the time of focus, the wave field will propagate away from the source location with the characteristic as if it were generated by a source mechanism at the focused event location. This is defined as a "virtual" source. This "virtual" source can then be used to for a wide variety of applications from multiple suppression, to medium characterization (Snieder et al., 2006; Mehta et al., 2008a; Mehta et al., 2008b; Wapenaar et al., 2012; Behura & Snieder, 2013). Additionally, one can continuously monitor and backpropagate signals to investigate the changes occurring within the medium. Using deconvolution, one can also define the type of source function focus that will occur at the event location. This was shown to work by Ulrich et al. (2012). Therefore, one could determine the frequency of the focused wave field and allow different frequency focuses to occur. One then records the scattered wave field generated by the virtual sources consisting of different frequencies to characterize the medium. Therefore, by using deconvolution, we could potentially improve the characterization of the medium compared with time reversal. In addition, the amplitude can be varied to study nonlinear effects. Finally, another application is the locating of microseismic events and fractures within a medium by using reverse-time imaging (Douma & Snieder, 2014).

6.5.5 Conclusion

In an experimental study a simple though robust method for determining the optimal signal for backpropagation such that one gets an improved temporal focus at the source location was introduced. Deconvolution was shown to have an optimal regularization parameter, γ, for improved temporal focusing. If one increases γ, the temporal focus approaches that of

time reversal; if one decreases γ, one increases the effect of noise and the temporal focus decreases dramatically. However, Figure 6-47 shows that one still attains a temporal focus even for different values of γ. Additionally, deconvolution does not break down when there are multiple source wavefields being propagated. This is due to the influence of the crosstalk terms being minimal for the complicated waveforms generated by scattering in the concrete. Thus, deconvolution has a robust nature comparable to that of time reversal while having the potential to dramatically improve the focus. In conclusion, the simple and robust nature of deconvolution allows it to be implemented as a preprocessing step to improve focusing at the source location.

6.6 Further developments

Coda Wave Interferometry is meanwhile used by several researchers for sonic or ultrasonic monitoring of concrete. In the view of the author, the following developments are of special interest:

- Using passive instead of active data, e.g. ambient vibrations (Salvermoser et al., 2015)
- Reducing the often-dominating temperature effects (e. g. Zhang et al., 2013a; Salvermoser et al., 2015)
- Combining coda wave and nonlinear techniques for lab scale experiments (Zhang at al., 2013b).

The use and significance of the methodology of "nonlinear ultrasound" is not yet fully explored, but might open completely new opportunities especially in monitoring lab experiments for material degradation and behavior under high loads (Payan et al., 2010; Kim et al., 2016; Shokouhi et al., 2017, to cite just a few).

In the author's research group at BAM on focal point is on the development of low-cost, reliable monitoring hardware for implementation at real constructions. Some large-scale objects and real constructions have been instrumented and monitored, as a tunnel in Munich, test bridge girders at RWTH Aachen (with the German Road Research Institute BASt) and an asphalt wear test site (at BASt). This is current work and will be reported soon.

The BAM internal theme project BLEIB on bridge infrastructure monitoring maintains a reference structure at our open-air test site BAM-TTS in Horstwalde. It is instrumented with embedded ultrasonic transducers and many other sensor types. One purpose is to compare the response of various monitoring concepts to certain load changes and damage scenarios.

In the frame of the EC funded Marie Curie ITN project INFRASTRAR (coordination O. Abraham, IFSTTAR, France) we are working on monitoring of concrete fatigue.

The time reversal technique (without deconvolution) was meanwhile shown to work for concrete structures in a large lab experiment and accompanying simulations by Kocur et al., (2016).

7 Conclusion and outlook

The material provided in this thesis as well as the work of other authors shows, that the use of geophysical methods and algorithms is of benefit to the nondestructive testing in civil engineering community, far beyond the straightforward use of some methods as GPR (radar). Geophysics deals with similar materials (composite, inhomogeneous, porous), but driven by the billion-dollar budgets of the oil industry connected with intense competition and the developments in computing capabilities it has reached a state which is far beyond that in ultrasonic or impulse radar echo testing in civil engineering. Some of those methods can be easily adapted and used for tasks, for which traditional testing has currently no solution.

It has been shown that methods adapted from seismic migration as Reverse Time Migration can help to overcome significant limitations of imaging methods currently used in ultrasonic echo investigations, especially in complex structures. Emerging techniques as ultrasonic monitoring of concrete infrastructure make use of geophysical techniques as well, e.g. using Coda Wave Interferometry to extract subtle information about changes in material properties and structure out of repeated ultrasonic transmission data.

This is not the end of the story. There is still some way to go before the techniques described here can be used extensively in practice due to their current limitations, e. g. cost of computation or lack of reliable, automated way to distinguish between different influence factors. In addition, there are many other geophysical techniques to be explored, as full waveform inversion for imaging or nonlinear techniques for monitoring.

It is the authors opinion that there is still much headroom to improve the interdisciplinary cooperation between geophysics and nondestructive testing in civil engineering. The application of novel methods from geophysics would help to overcome current limitations e.g., in imaging small structures or subtle changes. On the other hand, measurements on concrete structures might serve as scale-experiments to validate geophysical algorithms or simulation methods. This will not only encourage scientists and engineers to cross the boundary of their respective disciplines, but also generate business opportunities for small and medium enterprises. There is a strong need for new, easy-to-use and reasonably priced instrumentation as well as services. In various countries, geophysical service providers started to earn a significant and increasing part of their revenue by applying their skills in structural civil engineering projects, in addition to the geotechnical projects where they have been involved for a long time. This sector provides a most welcome additional revenue, especially in times of a struggling hydrocarbon industry. The demand is triggered by an ageing infrastructure in the so-called first world, but also by more and more complex and demanding constructions all over our planet.

8 Acknowledgements

Thanks to all who have contributed one way or the other, knowingly or unknowingly, named here or not, to the work compiled in this thesis.

First, there are all the colleagues and students who have been a part of the work on the scientific papers which are the background of this compilation:

Odile Abraham, Thomas Bohlen, Stefan Buske, Johannes Douma, Maria Grohmann, Sven Grothe, Chinaemerem Kanu, Jan Kittler, Markus König, Rolf Krompholz, Rainer Lautenschläger, Frank Mielentz, Mike Mooney, Sabine Müller, Stefan Pirskawetz, Christoph Sens-Schönfelder, Roel Snieder, Sarah Sieber, Simon Stähler, Herbert Wiggenhauser, Julia Wolf, Carolin Wunderlich.

It has been a pleasure. Really. Any mistakes created while editing the papers for this thesis are entirely my fault.

Second, I am most thankful to my "home base", BAM's division 8.2. Many of them have contributed to my research, from the workshop guys and engineers (Marco, Matthias, Sean), producing tools and concreting specimen, the secretariat (over the time: Dana, Sarah, Nicole) making my daily life easier, all colleagues contributing to my research or just directing me by their comments and feedback (too many to name), up to the head of division, Herbert Wiggenhauser, who gave me the necessary degree of freedom.

Two other persons must be mentioned here as well. Christoph Clauser (RWTH Aachen) motivated me to take this step and not to stop. Teaching at his institute has become an important part of my professional life – and I like it! Roel Snieder (Colorado School of Mines) is a friend and a role model in many aspects. The sabbatical in Golden in 2013 has changed my career and professional mindset, It has influenced me far beyond geophysics. Roel and his colleagues also gave the inspiration for several papers included in this thesis.

After writing my Ph.D. thesis in 2010, I asked my parents to review the "generally understandable summary". I got it back with some suggestions and the comment:" Finally, after 25 years, we understood what you are doing". No parental guidance this time. At the age of 53 I am finally on my own feet. Speaking of family: Thank you, Lennart and David, for helping me a lot in the editorial process.

And: Thank you, Antje. You gave me time, space and encouragement. And much more.

Addendum (October 2019): I am grateful to the "Referenten", who reviewed and evaluated this thesis: Professores Christoph Clauser, John Popovic and Christian Große. Christian, this was the second time you did this. And the last time, I promise. Christoph: thank you for the discussion around the "Addendum/Erratum" (see section 11). Many thanks also to Felix Clauss (Ph.D. student at Ruhr-Universität Bochum) who performed the 3D thermal simulations in section 11.

9 References

ACS Ltd., Moscow. "Low-frequency flaw detector A1220 MONOLITH", (retrieved August 1, 2014) http://www.acsys.ru/eng/production/detail/a1220-monolith/.

Aki, K., & Richards, P.-G. (2009): "Quantitative Seismology". 2. ed., Print. Sausalito, Calif: Univ. Science Books.

Anderson, B. E., Douma, J., Ulrich, T.J., Snieder, R. (2015): "Improving Spatio-Temporal Focusing and Source Reconstruction through Deconvolution". *Wave Motion*, 2015, Volume 52, pp. 151–159. doi:10.1016/j.wavemoti.2014.10.001

Anderson, B. E., Griffa, M., Larmat, C., Ulrich, T.J., & Johnson, P.A. (2008): "Time reversal". *Acoust. Today* 4, 5–16.

Anugonda, P., Wiehn, J.S., & Turner, J.A. (2001): "Diffusion of Ultrasound in Concrete". *Ultrasonics* 39, 6: 429–35. doi:10.1016/S0041-624X(01)00077-4.

ASTM Standard C39M-17 b: Standard Test Method for Compressive Strength of Cylindrical Concrete Specimens. 2017.

ASTM Standard C597-09: "Standard Test Method for Pulse Velocity Through Concrete". 2009.

Aubry, J.-F., Tanter, M., Gerber, J., Thomas, J.-L., & Fink, M. (2001): "Optimal Focusing by Spatio-Temporal Inverse Filter. II. Experiments. Application to Focusing through Absorbing and Reverberating Media". *The Journal of the Acoustical Society of America* 110, 1: 48. doi:10.1121/1.1377052.

Ballier, G., Mayer, K., Langenberg, K.-J., Schulze, S., & Krause, M. (2012): "Improvements on Tendon Duct Examination by Modelling and Imaging with Synthetic Aperture and One-Way Inverse Methods". 18th WCNDT, Durban, South Africa.

Baysal, E., Kosloff, D.D., & Sherwood, J.W.C. (1983): "Reverse Time Migration". GEOPHYSICS 48, 11: 1514–24. doi:10.1190/1.1441434.

Behura, J., & Snieder, R. (2013): "Virtual Real Source: Source Signature Estimation Using Seismic Interferometry". *Geophysics* 78, 5: Q57–68. doi:10.1190/geo2013-0069.1.

Bendetto, A., & Pajewski, L., Ed. (2015): "Civil Engineering Applications of Ground Penetrating Radar". Cham: Springer International Publishing.

Beniwal, S., Ghosh, D., & Ganguli, A. (2016): „Ultrasonic Imaging of Concrete Using Scattered Elastic Wave Modes". *NDT & E International* 82: 26–35. doi:10.1016/j.ndteint.2016.04.003.

Beniwal, S., & Ganguli, A. (2015): "Defect Detection around Rebars in Concrete Using Focused Ultrasound and Reverse Time Migration". *Ultrasonics* 62: 112–25. doi:10.1016/j.ultras.2015.05.008.

Bertaix, V., Garson, J., Quieffin, N., Catheline, S., Derosny, J., & Fink, M. (2004): "Time-Reversal Breaking of Acoustic Waves in a Cavity". *American Journal of Physics* 72, 10: 1308. doi:10.1119/1.1773577.

Bleistein, N., & Gray, S.H. (2001): "From the Hagedoorn Imaging Technique to Kirchhoff Migration and Inversion". *Geophysical Prospecting* 49, 6: 629–43. doi:10.1046/j.1365-2478.2001.00290.x.

Blomgren, P., Kyritsi, P., Kim, A.D, & Papanicolaou, G. (2008): "Spatial Focusing and Intersymbol Interference in Multiple-Input-Single-Output Time Reversal Communication Systems". *IEEE Journal of Oceanic Engineering* 33, 3: 341–55. doi:10.1109/JOE.2008.925083.

Bohlen, T. (2002): "Parallel 3-D Viscoelastic Finite Difference Seismic Modelling". *Computers & Geosciences* 28, 8: 887–99. doi:10.1016/S0098-3004(02)00006-7.

BS EN Standard 12504-4:2004: "Testing concrete. Determination of ultrasonic pulse velocity" (equivalent German version: DIN EN 12504-4:2004).

Buske, S. (1999); "Three-Dimensional Pre-Stack Kirchhoff Migration of Deep Seismic Reflection Data". *Geophysical Journal International* 137, 1: 243–60. doi:10.1046/j.1365-246x.1999.00789.x.

Buske, S. (1994): "Kirchhoffmigration von Einzelschussdaten (Kirchhoff migration of single shot data)". Diploma thesis, FU Berlin.

Chattopadhyay, S., & McMechan, G.A. (2008):. „Imaging conditions for prestack reverse-time migration". *GEOPHYSICS* 73, 3: S81–89. doi:10.1190/1.2903822.

Clayton, R.W., & Wiggins, R.A. (1976): "Source Shape Estimation and Deconvolution of Teleseismic Bodywaves". *Geophysical Journal International* 47, 1: 151–77. doi:10.1111/j.1365-246X.1976.tb01267.x.

Crase, E., Pica, A., Noble, M., McDonald, J., & Tarantola, A. (1990): "Robust Elastic Nonlinear Waveform Inversion: Application to Real Data". *GEOPHYSICS* 55, 5: 527–38. doi:10.1190/1.1442864.

Crawford, G.I. (1997): "Guide to Nondestructive Testing of Concrete, FHWA-SA-97-105". Federal Highway Administration, USA. http://www.fhwa.dot.gov/pavement/pubs/006641.pdf.

Daniels, R.C., & Heath, R.W.jr. (2005): "Improving on time reversal with MISO precoding". In *Proceedings of the Eighth International Symposium on Wireless Personal Multimedia Communications Conference*. Aalborg, Denmark.

Díaz, E., & Sava, P. (2016): "Understanding the Reverse Time Migration Backscattering: Noise or Signal? ". *Geophysical Prospecting* 64, 3: 581–94. doi:10.1111/1365-2478.12232.

DIN EN Standard 1992-1-1:2011-01: Eurocode 2: Bemessung und Konstruktion von Stahlbeton- und Spannbetontragwerken - Teil 1-1: Allgemeine Bemessungsregeln und Regeln für den Hochbau (Eurocode 2: Design of concrete structures - Part 1-1: General rules and rules for buildings).

DIN EN Standard 206:2017-01: Beton - Festlegung, Eigenschaften, Herstellung und Konformität (Concrete - Specification, performance, production and conformity).

DGZfP Guideline B4: "Merkblatt für Ultraschall-Impuls-Verfahren zur zerstörungsfreien Prüfung mineralischer Baustoffe und Bauteile (Guideline for ultrasonic impulse examination of mineralic construction materials)". DGZfP Merkblatt B4, 2019.

Douma, J., Niederleithinger, E., & Snieder, R. (2015): "Locating Events Using Time Reversal and Deconvolution: Experimental Application and Analysis". *Journal of Nondestructive Evaluation* 34, 1. doi:10.1007/s10921-015-0276-x.

Douma, J., & Snieder, R. (2014): "Focusing of Elastic Waves for Microseismic Imaging". *Geophysical Journal International* 200, 1: 390–401. doi:10.1093/gji/ggu398.

Douma, J., Snieder, R., Fish, A., & Sava, P. (2013): "Locating a Microseismic Event Using Deconvolution", 2206–11. Society of Exploration Geophysicists. doi:10.1190/segam2013-0446.1.

Dumbser, M., & Käser, M. (2006): "An Arbitrary High-Order Discontinuous Galerkin Method for Elastic Waves on Unstructured Meshes - II. The Three-Dimensional Isotropic Case". *Geophysical Journal International* 167, Nr. 1: 319–36. doi:10.1111/j.1365-246X.2006.03120.x.

Ertel, J.-P., Niederleithinger, E-. & Grohmann, M. (2016) „Advances in pile integrity testing". *Near Surface Geophysics* 14, Nr. 6: 503–12. doi:10.3997/1873-0604.2016030.

Farmer, P.A., Jones, I.F., Zhou, H., Bloor, R.I., & Goodwin, M.C. (2009); "Application of reverse time migration to complex imaging problems". *First Break* 24, Nr. 9.

Fink, M. (1997): "Time Reversed Acoustics". *Physics Today* 50, Nr. 3: 34. doi:10.1063/1.881692.

Fomel, S., Sava, P., Vlad, I., Liu, Y., & Bashkardin, V. (2013): "Madagascar: Open-Source Software Project for Multidimensional Data Analysis and Reproducible Computational Experiments". *Journal of Open Research Software* 1, 1: e8. doi:10.5334/jors.ag.

Friese, M., & Wiggenhauser, H. (2008): "New NDT technique for concrete structures: ultrasonic linear array and advanced imaging techniques". In: *Proceedings of NDE/NDT for Highways and Bridges, Structural Materials Technology (SMT)*.

Gallot, T., Catheline, S., Roux, P., & Campillo, M. (2012): "A Passive Inverse Filter for Green's Function Retrieval". *The Journal of the Acoustical Society of America* 131, 1: EL21. doi:10.1121/1.3665397.

Geoltrain, S., & Brac, J. (1993): "Can We Image Complex Structures with First-arrival Traveltime?" *Geophysics* 58, 4: 564–75. doi:10.1190/1.1443439.

Grêt, A., Snieder, R., & Özbay, U. (2006a): "Monitoring *in Situ* Stress Changes in a Mining Environment with Coda Wave Interferometry". *Geophysical Journal International* 167, 2: 504–8. doi:10.1111/j.1365-246X.2006.03097.x.

Grêt, A., Snieder, R., & Scales, J. (2006b): "Time-Lapse Monitoring of Rock Properties with Coda Wave Interferometry". *Journal of Geophysical Research: Solid Earth* 111, B3. doi:10.1029/2004JB003354.

Grohmann, M., Müller, S., Niederleithinger, E., & Sarah, S. (2017): "Reverse Time Migration: Introduction of a New Imaging Technique for Ultrasonic Measurements in Civil Engineering". *Near Surface Geophysics*, accepted for publication.

Grohmann, M., Niederleithinger, E., & Buske, S. (2016): "Geometry Determination of a Foundation Slab Using the Ultrasonic Echo Technique and Geophysical Migration Methods". *Journal of Nondestructive Evaluation* 35, 1. doi:10.1007/s10921-016-0334-z.

Große, C., & Schumacher, T. (2013): "Anwendungen der Schallemissionsanalyse an Betonbauwerken (Application of the Acoustic Emission Technology at Concrete Constructions)". *Bautechnik* 90, 11: 721–31. doi:10.1002/bate.201300074.

Hadziioannou, C., Larose, E., Coutant, O., Roux, P., & Campillo, M. (2009): "Stability of monitoring weak changes in multiply scattering media with ambient noise correlation: Laboratory experiments". *The Journal of the Acoustical Society of America* 125, 6: 3688. doi:10.1121/1.3125345.

Hedenblad, G. (1993): "Moisture permeability of some porous materials (Report TVBM (Intern 7000-rapport); Vol. 7068)". Division of Building Materials, LTH, Lund University. https://lup.lub.lu.se/record/1653173/file/1653174.pdf.

Hu, M., Chen, S.-E., & Pan, D. (2014): "Reverse Time Migration Based Ultrasonic Wave Detection for Concrete Structures", in: Skorpen, S., & Chen, A. Y., (Ed.): Design, Construction, and Maintenance of Bridges, p. 53–60. American Society of Civil Engineers. doi:10.1061/9780784478516.007.

Hughes, D. S., & Kelly, J.L. (1953): "Second-Order Elastic Deformation of Solids". *Physical Review* 92, 5: 1145–49. doi:10.1103/PhysRev.92.1145.

Jonsson, B.L.G., de Hoop, M.V., Gustafsson, M., & Weston, V.H. (2004): "Retrofocusing of Acoustic Wavefields by Iterated Time Reversal". *SIAM Journal on Applied Mathematics* 64, 6: 1954–86. doi:10.1137/S0036139903426964.

Johnson, P.A., & Rasolofosaon, P.N.J. (1996): "Nonlinear Elasticity and Stress-Induced Anisotropy in Rock". *Journal of Geophysical Research: Solid Earth* 101, B2: 3113–24. doi:10.1029/95JB02880.

Jones, R., & Fącąoaru, I. (1969): "Recommendations for Testing Concrete by the Ultrasonic Pulse Method". *Matériaux et Constructions* 2, 4: 275–84. doi:10.1007/BF02475162.

Kaelin, B., & Guitton, A. (2006): "Imaging condition for reverse time migration," *SEG Technical Program Expanded Abstracts*, vol. 25, no. 1, pp. 2594–2598.

Kalogeropoulos, A., van der Kruk, J., Bikowski, J. ,Hugenschmidt, J., & Bruehwiler, E. (2012): „GPR full-waveform inversion of chloride gradients in concrete“, 320–23. IEEE, 2012. doi:10.1109/ICGPR.2012.6254882.

Köhn, D., Meier, T., Fehr, M., De Nil, D., &Auras, M. (2016): „Application of 2D Elastic Rayleigh Waveform Inversion to Ultrasonic Laboratory and Field Data“. *Near Surface Geophysics* 14, Nr. 2139. doi:10.3997/1873-0604.2016027.

Kanu, C. (2014): "Time-lapse monitoring of localized changes within heterogeneous media with scattered waves". PhD thesis, Colorado School of Mines.

Kanu, C., & Snieder, R. (2015): "Numerical computation of the sensitivity kernel for monitoring weak changes with multiply scattered acoustic waves." *Geophysical Journal International* 203.3: 1923-1936.

Kanu, C., & Snieder, R. (2015): "Time-Lapse Imaging of a Localized Weak Change with Multiply Scattered Waves Using Numerical-Based Sensitivity Kernel: IMAGING OF LOCALIZED CHANGES". *Journal of Geophysical Research: Solid Earth* 120, 8: 5595–5605. doi:10.1002/2015JB011871.

Kanu, C., Snieder, R., Niederleithinger, E., & Grothe, S. (2017): "Time-lapse imaging of localized weak changes with multiply scattered waves: Laboratory experiment." *To be re-submitted to JONE*.

Karbhari, V.M., & Ansari, F., Ed. (2009): "Structural Health Monitoring of Civil Infrastructure Systems”. Woodhead Publishing in Materials. Boca Raton, Fla.: CRC Press.

Kee, S.-H., & Zhu, J. (2013): "Using piezoelectric sensors for ultrasonic pulse velocity measurements in concrete". *Smart Materials and Structures* 22, 11: 115016. doi:10.1088/0964-1726/22/11/115016.

Keiswetter, D.A., & Steeples, D.W. (1995): "A Field Investigation of Source Parameters for the Sledgehammer". *GEOPHYSICS* 60, 4: 1051–57. doi:10.1190/1.1443833.

Kim, G., Kim, J.-Y., Kurtis K. E., Jacobs, L. J., Le Pape, Y., & Guimaraes, M. (2016): „Quantitative Evaluation of Carbonation in Concrete Using Nonlinear Ultrasound“. *Materials and Structures* 49, Nr. 1–2 (Januar 2016): 399–409. doi:10.1617/s11527-014-0506-1.

Kocur, G. K., Saenger E. H., Grosse, C. U., & Vogel, T. (2016): „Time Reverse Modeling of Acoustic Emissions in a Reinforced Concrete Beam“. *Ultrasonics* 65: 96–104. doi:10.1016/j.ultras.2015.10.014.

Köhn, D., Meier, T., Fehr, M., De Nil, D., &Auras, M. (2016): „Application of 2D Elastic Rayleigh Waveform Inversion to Ultrasonic Laboratory and Field Data“. *Near Surface Geophysics* 14, Nr. 2139. doi:10.3997/1873-0604.2016027.

König, Markus (2016): "Detection of Hidden Cracks in Concrete Strctures Using Reverse Time Migration of Ultrasonic Echo Data". Master thesis BAM/RWTH Aachen.

Krause, M., Mayer, K., Friese, M., Milmann, B., Mielentz, F., & Ballier, G. (2011): "Progress in Ultrasonic Tendon Duct Imaging". *European Journal of Environmental and Civil Engineering* 15, 4: 461–85. doi:10.1080/19648189.2011.9693341.

Krause, M., Milmann, B., Mielentz, F., Streicher, D., Redmer, B., Mayer, K., Langenberg, K.-J., & Schickert, M. (2008): "Ultrasonic Imaging Methods for Investigation of Post-Tensioned Concrete Structures: A Study of Interfaces at Artificial Grouting Faults and Its Verification". *Journal of Nondestructive Evaluation* 27, 1–3: 67–82. doi:10.1007/s10921-008-0033-5.

Kurzmann, A., Koehn, D., Przebindowska, A., Nguyen, N., & Bohlen, T. (2009): "Acoustic full waveform tomography: performance and optimization," in: Proceedings of the 70th EAGE Conference and Technical Exhibition, Amsterdam, The Netherlands.

Langenberg, K.J., Bärmann, R., Marklein, R., Irmer. S., Müller, H., Brandfaß, M., & Potzkai, B. (1997): "Electromagnetic and Elastic Wave Scattering and Inverse Scattering Applied to Concrete". *NDT & E International* 30, 4: 205–10. doi:10.1016/S0963-8695(96)00057-6.

Langenberg, K.-J., Marklein R., & Mayer, K. (2009): Theoretische Grundlagen der zerstörungsfreien Materialprüfung mit Ultraschall (Theory of no-destructive material testing using ultrasound). München: Oldenbourg.

Larmat, C.S., Guyer, R.A., & Johnson, P.A. (2010): "Time-Reversal Methods in Geophysics". *Physics Today* 63, 8: 31–35. doi:10.1063/1.3480073.

Larose, E., de Rosny, J., Margerin, L., Anache, D., Gouedard, P., Campillo, M., & van Tiggelen, B. (2006): "Observation of multiple scattering of kHz vibrations in a concrete structure and application to monitoring weak changes". *Physical Review E* 73, 1. doi:10.1103/PhysRevE.73.016609.

Larose, E., & Hall, S. (2009): "Monitoring stress related velocity variation in concrete with a 2.10^-5 relative resolution using diffuse ultrasound". *J. Acoust. Soc. Am.* 125: 1853–57. doi: 10.1121/1.3079771.

Larose, E., Obermann, A., Digulescu, A., Planès, T., Chaix, J.-F., Mazerolle, F., & Moreau, G. (2015): "Locating and Characterizing a Crack in Concrete with Diffuse Ultrasound: A Four-Point Bending Test". *The Journal of the Acoustical Society of America* 138, 1: 232–41. doi:10.1121/1.4922330.

Larose, E., Planes, T., Rossetto, V., & Margerin, L. (2010): "Locating a small change in a multiple scattering environment". *Applied Physics Letters* 96, 20: 204101. doi:10.1063/1.3431269.

Lencis, U., Udris, A., & Korjakins, A. (2013): "Moisture Effect on the Ultrasonic Pulse Velocity in Concrete Cured under Normal Conditions and at Elevated Temperature". *Construction Science* 14. doi:10.2478/cons-2013-0011.

Leonhardt, F., & Baur, W. (1971): "Erfahrungen mit dem Taktschiebeverfahren im Brücken- und Hochbau". *Beton- und Stahlbetonbau* 66, 7: 161–67.

Liu, F., Zhang, G., Morton, S. A., & Leveille, J.P (2011): „An effective imaging condition for reverse-time migration using wavefield decomposition“. *GEOPHYSICS* 76, 1: S29–39. doi:10.1190/1.3533914.

Loewenthal, D., & Mufti, I.R. (1983): "Reversed Time Migration in Spatial Frequency Domain". *GEOPHYSICS* 48, 5: 627–35. doi:10.1190/1.1441493.

Maack, S. (2012): "Untersuchungen zum Schallfeld niederfrequenter Ultraschallprüfköpfe für die Anwendung im Bauwesen (Studies on the beam field of low frequency ultrasonic transducers for application in civil engineering)". PhD thesis, Technische Universität Berlin.

Matsumoto, S., Obara, K., Yoshimoto, K., Saito, T., Ito, A., & Hasegawa, A. (2001): "Temporal Change in P -Wave Scatterer Distribution Associated with the *M* 6.1 Earthquake near Iwate Volcano, Northeastern Japan". *Geophysical Journal International* 145, 1: 48–58. doi:10.1111/j.1365-246X.2001.00339.x.

Mayer, K., Krause, M., Wiggenhauser, H., & Milmann, B. (2015): „Investigations for the Improvement of the SAFT Imaging Quality of a Large Aperture Ultrasonic System“. In *International Symposium Nondestructive Testing in Civil Engineering (NDT-CE)*. Berlin, Germany, 2015. http://www.ndt.net/article/ndtce2015/papers/159_mayer_klaus.pdf.

Mayer, K., & Cinta, P.M. (2012): "Mayer, K., Chinta, P.M.: User Guide of Graphical User Interface inter_saft". University of Kassel, Department of Computational Electronics and Photonics.

Mayer, K., Langenberg, K.-J., Krausem, M., Milmann, B., & Mielentz, F. (2008): "Characterization of Reflector Types by Phase-Sensitive Ultrasonic Data Processing and Imaging". *Journal of Nondestructive Evaluation* 27, 1–3: 35–45. doi:10.1007/s10921-008-0035-3.

Mayer, K., Marklein, R., Langenberg K.-J., & Kreutter, T. (1990): "Three-dimensional imaging system based on fourier transform synthetic aperture focusing technique," *Ultrasonics*, vol. 28, no. 4, pp. 241–255.

McCann, D.M, & Forde, M.C. (2001): "Review of NDT Methods in the Assessment of Concrete and Masonry Structures". *NDT & E International* 34, 2: 71–84. doi:10.1016/S0963-8695(00)00032-3.

McMechan, G.A. (1983): "Migration by Extrapolation of Time-Dependent Boundary Values". *Geophysical Prospecting* 31, 3: 413–20. doi:10.1111/j.1365-2478.1983.tb01060.x.

Mehta, K., Sheiman, J.L., Snieder, R., & Calvert, R. (2008a): "Strengthening the Virtual-Source Method for Time-Lapse Monitoring". *GEOPHYSICS* 73, 3: S73–80. doi:10.1190/1.2894468.

Mehta, K., Snieder, R., Calvert, R., & Sheiman, R. (2008b): "Acquisition Geometry Requirements for Generating Virtual-Source Data". *The Leading Edge* 27, 5: 620–29. doi:10.1190/1.2919580.

Mielentz, F. (2007): "Einsatzpotenzial von laufzeitgesteuerten Ultraschall-Gruppenstrahlern an Betonbauteilen (Application potential of ultrasonic phased arrays on concrete constructions)". BAM-Dissertationsreihe 24. Bremerhaven: Wirtschaftsverl. NW, Verl. für neue Wiss.

Mielentz, F., Feller, V., Krause, M., & Orglmeister, R. (2015): "Ultraschallprüfung von Betonbauteilen – Laufzeitgesteuerte Gruppenstrahler Mit Punktkontaktprüfköpfen (Ultrasonic Testing of Concrete Constructions – Phased Arrays)." *Materials Testing* 57, no. 4: 329–36. doi:10.3139/120.110723.

Mindess, S., Young, J.F., & Darwin, D. (2003): *Concrete*. 2nd ed. Upper Saddle River, NJ: Prentice Hall.

Montaldo, G., Tanter, M., & Fink, M. (2004): "Real Time Inverse Filter Focusing through Iterative Time Reversal". *The Journal of the Acoustical Society of America* 115, 2: 768. doi:10.1121/1.1636462.

Müller, S., Niederleithinger, E., Krause, M., & Bohlen, T. (2010): "Reverse time migration: a seismic imaging technique applied to ultrasonic data," in Proceedings of the SMT Conference of NDE/NDT for Highways and Bridges: Structural Materials Technology (SMT), New York, NY, USA, August 2010.

Müller, S., Niederleithinger, E., Krause, M., & Bohlen, T. (2012): "Reverse Time Migration: A Seismic Imaging Technique Applied to Ultrasonic Data". *International Journal of Geophysics*, Volume 2012, Article ID 128465, 7 pages, Doi:10.1155/2012/128465.

Müller, S., & Niederleithinger, E. (2014): "Anwendung der Reverse Time Migration auf Ultraschall-Echo-Messungen in der zerstörungsfreien Prüfung im Bauwesen". DGZfP-Jahrestagung, Potsdam. http://www.ndt.net/article/dgzfp2014/papers/di1c4.pdf.

Müller, G., Weber M., Rümpker G., & Gajewski D. (2007): "Theory of elastic waves". Potsdam/Frankfurt/Hamburg, 2007. http://gfz-potsdam.de/mhw/tew/.

Murnaghan, F. D. (1937): "Finite Deformations of an Elastic Solid". *American Journal of Mathematics* 59, 2: 235. doi:10.2307/2371405.

Naus, D.J. (2005): "The effect of elevated temperature on concrete materials and structures-a literature review". Oak Ridge National Laboratory, for the U.S. Department of Energy under Contract No. DE-AC05-00OR2275. http://info.ornl.gov/sites/publications/files/Pub1043.pdf.

Niederleithinger, E., Abraham, O., & Mooney, M. (2016): Foreword (to: Special issue on Geophysical Methods in Civil Engineering). Near Surface Geophysics, 14(6), 479-480.Doi: 10.3997/1873-0604.2016043.

Niederleithinger, E., Wolf, J., Mielentz, J., Wiggenhauser, H., & Pirskawetz, S. (2015a): "Embedded Ultrasonic Transducers for Active and Passive Concrete Monitoring". *Sensors* 15, 5: 9756–72. doi:10.3390/s150509756.

Niederleithinger, E., Krompholz R., Müller S., Lautenschläger R., & Kittler J. (2015b): "36 Jahre Talsperre Eibenstock – 36 Jahre Überwachung des Betonzustands durch Ultraschall". In *38. Dresdner Wasserbaukolloquium 2015 "Messen und Überwachen im Wasserbau und am Gewässer"*. Dresden.

Niederleithinger, E., & Ranz Garcia, J. (2014): Quality assurance of diaphragm walls by sonar measurements – model study. *Proceedings of the ICE - Geotechnical Engineering*, 167(2), 217-226, Doi: 10.1680/geng.13.00038.

Niederleithinger, E., Sens-Schönfelder C., Grothe S., & Wiggenhauser H. (2014): "Coda Wave Interferometry used to localize compressional load effects on a concrete specimen". In *Proceedings of 7th European Workshop on Structural Health Monitoring (EWSHM)*. Nantes, France.

Niederleithinger, E., Weller, A., & Lewis, R. (2012): Evaluation of Geophysical Techniques for Dike Inspection. JEEG, v. 17 no. 4 p. 185-195. Doi: 10.2113/JEEG17.4.185.

Niederleithinger, E. (2012): Optimization and Extension of the Parallel Seismic Method. *Soils & Foundation*, v. 52, n. 6, pp. 1093–1101. Doi: 10.1016/j.sandf.2012.11.023.

Niederleithinger, E., & Wunderlich C. (2012): "Influence of small temperature variations on the ultrasonic velocity in concrete". In *Proceedings of QNDE 2012*, 390–97. Denver. doi:10.1063/1.4789074.

Niederleithinger E., Shokouhi P., Stähler S., & Nowak T.-R. (2010): Proceedings of ECNDT, Moscow, p. 1-9.

Oeser, J., Bunge, H.-P., & Mohr, M. (2006): "Cluster Design in the Earth Sciences Tethys". In *High Performance Computing and Communications*, herausgegeben von Michael Gerndt und Dieter Kranzlmüller, 4208:31–40. Berlin, Heidelberg: Springer Berlin Heidelberg. http://link.springer.com/10.1007/11847366_4.

Ohdaira, E., & Masuzawa, N. (2000): "Water Content and Its Effect on Ultrasound Propagation in Concrete — the Possibility of NDE". *Ultrasonics* 38, 1–8: 546–52. doi:10.1016/S0041-624X(99)00158-4.

Paasschens, J.C.J. (1997): "Solution of the Time-Dependent Boltzmann Equation". *Physical Review E* 56, 1: 1135–41. doi:10.1103/PhysRevE.56.1135.

Pacheco, C., & Snieder, R. (2005): "Time-lapse travel time change of multiply scattered acoustic waves". *The Journal of the Acoustical Society of America* 118, 3: 1300. doi:10.1121/1.2000827.

Page, J.H., Schriemer, H.P., Bailey, A.E., & Weitz, D.A. (1995): "Experimental Test of the Diffusion Approximation for Multiply Scattered Sound". *Physical Review E* 52, 3: 3106–14. doi:10.1103/PhysRevE.52.3106.

Parvulescu, A., & Clay, C.S. (1965): "Reproducibility of Signal Transmissions in the Ocean". *Radio and Electronic Engineer* 29, 4: 223. doi:10.1049/ree.1965.0047.

Payan, C., Quiviger, A., Garnier, V., Chaix, J.F., & Salin, J. (2013): "Applying Diffuse Ultrasound under Dynamic Loading to Improve Closed Crack Characterization in Concrete". *The Journal of the Acoustical Society of America* 134, 2: EL211. doi:10.1121/1.4813847.

Payan, C., Garnier, V., & Moysan, J. (2010): „Potential of Nonlinear Ultrasonic Indicators for Nondestructive Testing of Concrete“. *Advances in Civil Engineering* 2010: 1–8. doi:10.1155/2010/238472.

Payan, C., Garnier, V., Moysan, J., & Johnson, P.A. (2009): "Determination of Third Order Elastic Constants in a Complex Solid Applying Coda Wave Interferometry". *Applied Physics Letters* 94, 1: 11904. doi:10.1063/1.3064129.

Planès, T., Larose, E., Margerin, L., Rossetto, V., & Sens-Schönfelder, C. (2014): "Decorrelation and Phase-Shift of Coda Waves Induced by Local Changes: Multiple Scattering Approach and Numerical Validation". *Waves in Random and Complex Media* 24, 2: 99–125. doi:10.1080/17455030.2014.880821.

Planès, T., & Larose, E. (2013): "A Review of Ultrasonic Coda Wave Interferometry in Concrete". *Cement and Concrete Research* 53: 248–55. doi:10.1016/j.cemconres.2013.07.009.

Podvin, P., & Lecomte, I. (1991): "Finite Difference Computation of Traveltimes in Very Contrasted Velocity Models: A Massively Parallel Approach and Its Associated Tools". *Geophysical Journal International* 105, 1: 271–84. doi:10.1111/j.1365-246X.1991.tb03461.x.

Poupinet, G., Ellsworth, W.L., & Frechet, J. (1984): "Monitoring Velocity Variations in the Crust Using Earthquake Doublets: An Application to the Calaveras Fault, California". *Journal of Geophysical Research: Solid Earth* 89, B7: 5719–31. doi:10.1029/JB089iB07p05719.

Qiu, R., Zhou, C., Guo, N., & Zhang, J. (2006): "Time Reversal With MISO for Ultrawideband Communications: Experimental Results". *Antennas and Wireless Propagation Letters* 5, 1: 269–73. doi:10.1109/LAWP.2006.875888.

Ramamoorthy, S. K., Kane, Y., & Turner, J.A. (2004): "Ultrasound Diffusion for Crack Depth Determination in Concrete". *The Journal of the Acoustical Society of America* 115, 2: 523. doi:10.1121/1.1642625.

Reynolds, J. M. (2011): An Introduction to Applied and Environmental Geophysics. John Wiley & Sons, Ltd.

Rossetto, V., Margerin, L., Planès, T., & Larose, E. (2011): "Locating a weak change using diffuse waves: Theoretical approach and inversion procedure". *Journal of Applied Physics* 109, 3: 34903. doi:10.1063/1.3544503.

Roux, P., & Fink, M. (2000): "Time Reversal in a Waveguide: Study of the Temporal and Spatial Focusing". *The Journal of the Acoustical Society of America* 107, 5: 2418. doi:10.1121/1.428628.

Royer, D., & Dieulesaint, E. (2000): *Elastic Waves in Solids*. Advanced Texts in Physics. Berlin ; New York: Springer.

Saenger, E. H., Kocur, G. K., Jud, R., & Torrilhon, M. (2011): „Application of Time Reverse Modeling on Ultrasonic Nondestructive Testing of Concrete“. *Applied Mathematical Modelling* 35, 2: 807–16. doi:10.1016/j.apm.2010.07.035.

Saint-Pierre, F., Rivard, P., & Ballivy, G. (2007): "Measurement of Alkali–silica Reaction Progression by Ultrasonic Waves Attenuation". *Cement and Concrete Research* 37, 6: 948–56. doi:10.1016/j.cemconres.2007.02.022.

Salvermoser, J., Hadziioannou, C., & Stähler, S.C. (2015): "Structural Monitoring of a Highway Bridge Using Passive Noise Recordings from Street Traffic". *The Journal of the Acoustical Society of America* 138, 6: 3864–72. doi:10.1121/1.4937765.

Sansalone, M., & Carino, N. (1988): "Impact echo method". *Concrete International* 10: 38–46.

Sato, H., & Fehler, M.C. (1988): *Seismic Wave Propagation and Scattering in the Heterogeneous Earth : Second Edition*. Berlin, Heidelberg: Springer Berlin Heidelberg.

Sava, P., & Hill, S.J. (2009): "Overview and Classification of Wavefield Seismic Imaging Methods". *The Leading Edge* 28, 2: 170–83. doi:10.1190/1.3086052.

Sayers, C.M. (1988): "Stress-Induced Ultrasonic Wave Velocity Anisotropy in Fractured Rock". *Ultrasonics* 26, 6: 311–17. doi:10.1016/0041-624X(88)90028-5.

Schaff, D.P., & Beroza, G.C. (2004): "Coseismic and Postseismic Velocity Changes Measured by Repeating Earthquakes: COSEISMIC AND POSTSEISMIC VELOCITY CHANGES". *Journal of Geophysical Research: Solid Earth* 109, B10. doi:10.1029/2004JB003011.

Schickert, M., Krause, M., & Müller, W. (2003): "Ultrasonic Imaging of Concrete Elements Using Reconstruction by Synthetic Aperture Focusing Technique". *Journal of Materials in Civil Engineering* 15, 3: 235–46. doi:10.1061/(ASCE)0899-1561(2003)15:3(235).

Schneider, W.A. (1978): "Integral Formulation for Migration in Two and Three Dimensions". *GEOPHYSICS* 43, 1: 49–76. doi:10.1190/1.1440828.

Schubert, M., Stoppel, M., & Wiggenhauser, H. (2015): "Automatic Scanning System for Nondestructive Testing of Vertical and Bottom Surfaces". In *International Symposium Non-Destrctive Testing in Civil Engineering (NDT-CE)*, paper 107. Berlin. http://www.ndt.net/article/ndtce2015/papers/107_schubert_marcus.pdf

Schön, J.H. (2004): "Physical Properties of Rocks: Fundamentals and Principles of Petrophysics". Elsevier, Amsterdam.

Sens-Schönfelder, C., & Larose, E. (2008): "Temporal Changes in the Lunar Soil from Correlation of Diffuse Vibrations". *Physical Review E* 78, 4. doi:10.1103/PhysRevE.78.045601.

Sens-Schönfelder, C., & Wegler, U. (2006): "Passive image interferometry and seasonal variations of seismic velocities at Merapi Volcano, Indonesia". *Geophysical Research Letters* 33, 21. doi:10.1029/2006GL027797.

Shapiro, S.A., & Kneib, G. (1993): "Seismic Attenuation By Scattering: Theory and Numerical Results". *Geophysical Journal International* 114, 2: 373–91. doi:10.1111/j.1365-246X.1993.tb03925.x.

Shokouhi, P., Riviere, J., Le Bas, P.-Y., & Ulrich, T. J. (2017): „Nonlinear Acoustic Testing for Concrete Materials Evaluation". *Materials Evaluation* 75, Nr. 3.

Shokouhi, P., Zoëga, A., Wiggenhauser, H., & Fischer, G. (2012): "Surface Wave Velocity-Stress Relationship in Uniaxially Loaded Concrete". *ACI Materials Journal* 109, 2. doi:10.14359/51683700.

Shokouhi, P., Zoëga, A., & Wiggenhauser, H. (2010): "Nondestructive Investigation of Stress-Induced Damage in Concrete". *Advances in Civil Engineering* 2010: 1–9. doi:10.1155/2010/740189.

Sieber, S., (2015): "Image Denoising of Migrated Ultrasonic Echo Data Acquired on Concrete". Master thesis BAM/RWTH Aachen.

Snieder, R. (2002): "General theory of elastic wave scattering". In *Pike, R. and P. Sabatier (eds.): Scattering and Inverse Scattering in Pure and Applied Science*, 528–42. San Diego: Academic Press.

Snieder, R. (2006): "The Theory of Coda Wave Interferometry". *Pure and Applied Geophysics* 163, 2–3: 455–73. doi:10.1007/s00024-005-0026-6.

Snieder, R., Gret, A., Douma, H., & Scales, J. (2002): "Coda Wave Interferometry for estimating nonlinear behavior in seismic velocity". *Science* 295: 2253–55.

Snieder, R., Sheiman, J. L., & Calvert, R. (2006): "Equivalence of the Virtual-Source Method and Wave-Field Deconvolution in Seismic Interferometry". *Physical Review E* 73, 6. doi:10.1103/PhysRevE.73.066620.

Song, G., Gu, H., & Mo, Y.-L. (2008): "Smart aggregates: multi-functional sensors for concrete structures—a tutorial and a review". *Smart Materials and Structures* 17, 3: 33001. doi:10.1088/0964-1726/17/3/033001.

Spane, F. A. (2002): "Considering Barometric Pressure in Groundwater Flow Investigations". *Water Resources Research* 38, 6: 14-1-14–18. doi:10.1029/2001WR000701.

Spies, M., Rieder, H., Orth, T., & Maack, S. (2012) "Simulation of ultrasonic arrays for industrial and civil engineering applications including validation". In *Review Prog. Quant. Nondestr. Eval.*, 31:841–48, 2012. doi:10.1063/1.4716312.

Spruit, R., van Tol, F., Broere, W., Slob, E., & Niederleithinger, E. (2014): "Detection of anomalies in diaphragm walls with Crosshole Sonic Logging". *Canadian Geotechnical Journal* 51 (4): 369–380. Doi: 10.1139/cgj-2013-0204.

Stähler, S., Niederleithinger, E., & Sens-Schönfelder, C. (2011): "Monitoring stress changes in a concrete bridge with Coda Wave Interferometry". *Journal of the Acoustical Society of America*, 129(4), 1945–1952, Doi:10.1121/1.3553226.

Stoppel, M., Taffe, A., Wiggenhauser, H., Kurz, J.H., & Boller, C. (2011): "Automated multi-sensor systems in civil engineering for condition assessment of concrete structures". In *Concrete solutions 2011 - 4th International conference on concrete repair (Proceedings)*, 397–403. Dresden, Germany: Taylor & Francis.

Streicher, D., Algernon D., Wöstmann J., Behrens M., & Wiggenhauser H. (2006): "Automated NDE of Post-Tensioned Concrete Bridges Using Imaging Echo Methods", WE1.3.1. Berlin. http://www.ndt.net/article/ecndt2006/doc/We.1.3.1.pdf.

Suaris, W., & Fernando, V. (1987): "Ultrasonic Pulse Attenuation as a Measure of Damage Growth During Cyclic Loading of Concrete". *ACI Materials Journal* 84, 3. doi:10.14359/1898.

Taffe, A. (2008): "Zur Validierung quantitativer zerstörungsfreier Prüfverfahren im Stahlbetonbau am Beispiel der Laufzeitmessung (On the validation of quantitative nondestructive test methods in reinforced concrete constructions by the example of time of flight measurements)", PhD thesis, RWTH Aachen.

Tanter, M., Aubry, J.-F., Gerber, J., Thomas, J.-L., & Fink, M. (2001): "Optimal Focusing by Spatio-Temporal Inverse Filter. I. Basic Principles". *The Journal of the Acoustical Society of America* 110, 1: 37. doi:10.1121/1.1377051.

Tanter, M., Thomas, J.-L., & Fink, M. (2000): "Time Reversal and the Inverse Filter". *The Journal of the Acoustical Society of America* 108, 1: 223. doi:10.1121/1.429459.

Toupin, R.A., & Bernstein, B. (1961): "Sound Waves in Deformed Perfectly Elastic Materials. Acoustoelastic Effect". *The Journal of the Acoustical Society of America* 33, 2: 216. doi:10.1121/1.1908623.

Tronicke, J. (2007): "The Influence of High Frequency Uncorrelated Noise on First-Break Arrival Times and Crosshole Traveltime Tomography". *Journal of Environmental & Engineering Geophysics* 12, 2: 173–84. doi:10.2113/JEEG12.2.173.

Ulrich, T.J., Anderson, B., Le Bas, P.-Y., Payan, C., Douma, J., & Snieder, R. (2012): "Improving time reversal focusing through deconvolution: 20 questions", 045015–045015. doi:10.1121/1.4764487.

Van Den Abeele, K., & De Visscher, J. (2000): "Damage Assessment in Reinforced Concrete Using Spectral and Temporal Nonlinear Vibration Techniques". *Cement and Concrete Research* 30, 9: 1453–64. doi:10.1016/S0008-8846(00)00329-X.

Vignon, F., Aubry, J.-F., Saez, A., Tanter, M., Cassereau, D., Montaldo, G., & Fink, M. (2006): "The Stokes Relations Linking Time Reversal and the Inverse Filter". *The Journal of the Acoustical Society of America* 119, 3: 1335. doi:10.1121/1.2161452.

Wolf, J., Niederleithinger, E., Mielentz, F., Grothe, S., & Wiggenhauser, H. (2014): "Überwachung von Betonkonstruktionen mit eingebetteten Ultraschallsensoren". *Bautechnik* 91, 11: 783–96. doi:10.1002/bate.201400073.

Wang, L. (2005): "Damage Identification in a Composite Plate using Prestack Reverse-time Migration Technique". *Structural Health Monitoring* 4, 3: 195–211. doi:10.1177/1475921705055233.

Wapenaar, K., Broggini, F., & Snieder, R. (2012): "Creating a Virtual Source inside a Medium from Reflection Data: Heuristic Derivation and Stationary-Phase Analysis: Creating a Virtual Source from Reflection Data". *Geophysical Journal International* 190, 2: 1020–24. doi:10.1111/j.1365-246X.2012.05551.x.

Wesley, J.P. (1965): "Diffusion of Seismic Energy in the near Range". *Journal of Geophysical Research* 70, 20: 5099–5106. doi:10.1029/JZ070i020p05099.

Wiggenhauser, H., Samokrutov, A., Mayer, K., Krause, M., Alekhin, S., and Elkin, V. (2016): „Large Aperture Ultrasonic System for Testing Thick Concrete Structures“. *Journal of Infrastructure Systems* 23:1:B4016004. doi:10.1061/(ASCE)IS.1943-555X.0000314.

Wu, T. T., & Lin, T.F. (1998): "The Stress Effect on the Ultrasonic Velocity Variations of Concrete under Repeated Loading". *ACI Materials Journal* 95, 5. doi:10.14359/394.

Zellner, W., & Svensson, H. (1983): "Incremental Launching of Structures". *Journal of Structural Engineering* 109, 2: 520–37. doi:10.1061/(ASCE)0733-9445(1983)109:2(520).

Zhang, Y., Planès, T., Larose, E., Obermann, A., Rospars, C., & Moreau, G. (2016): "Diffuse Ultrasound Monitoring of Stress and Damage Development on a 15-Ton Concrete Beam". *The Journal of the Acoustical Society of America* 139, 4: 1691–1701. doi:10.1121/1.4945097.

Zhang, Y., Abraham, O., Tournat, V., Le Duff, A., Lascoup, B., Loukili, A., Grondin, F., & Durand, O. (2013a): "Validation of a Thermal Bias Control Technique for Coda Wave Interferometry (CWI)". *Ultrasonics* 53, 3: 658–64. doi:10.1016/j.ultras.2012.08.003.

Zhang, Y., Tournat, V., Abraham, O., Durand, O., Letourneur, S., Le Duff, A., & Lascoup, B. (2013b): „Nonlinear Mixing of Ultrasonic Coda Waves with Lower Frequency-Swept Pump Waves for a Global Detection of Defects in Multiple Scattering Media“. *Journal of Applied Physics* 113, Nr. 6 (14. Februar 2013): 064905. doi:10.1063/1.4791585.

Zhang, Y., Abraham, O., Grondin, F., Loukili, A., Tournat, V., Le Duff, A., Lascoup, B., & Durand, O. (2012): "Study of stress-induced velocity variation in concrete under direct tensile force and monitoring of the damage level by using thermally-compensated Coda Wave Interferometry". *Ultrasonics* 52, 8: 1038–45. doi:10.1016/j.ultras.2012.08.011.

Zhang, Y., Abraham, O., Larose, E., Planes, T., Le Duff, A., Lascoup, B., Tournat, V., El Guerjouma, R., Cottineau, L.M., & Durand, O. (2011): "Following Stress Level Modification of real size concrete structures with Coda Wave Interferometry (CWI)". In: *Review of Progress in QNDE*, edited by D. O. Thompson and D. E. Chimenti, American Institute of Physics, Melville, NY, pp. 1291-1298, doi:10.1063/1.3592082.

Zhao, J., Bao, T., Chen, S. and Kundu, T (2016): „Smart Aggregate-Piezoceramic Patch Combination for Health Monitoring of Concrete Structures“. *Journal of Sensors* 2016 (2016): 1–7. doi:10.1155/2016/3270916.

Zhou, C., Guo, N., & Qiu, R. C. (2006): "Experimental Results on Multiple-Input Single-Output (MISO) Time Reversal for UWB Systems in an Office Environment", 1–6. IEEE. doi:10.1109/MILCOM.2006.302328.

Zhou, C., & Qiu, R.C. (2006): "Spatial Focusing of Time-Reversed UWB Electromagnetic Waves in a Hallway Environment", 102–6. IEEE. doi:10.1109/SSST.2006.1619051.

Zhou, L., Yuan, F.G., & Meng, W.J. (2007): "A pre-stack migration method for damage identificationin composite structures". *Smart Structures and Systems,* 3, 4: 439–54.

Zoëga, A., Shokouhi, P., & Wiggenhauser, H. (2009): "Propagation Time of Elastic Surface Waves on Concrete Specimens under Uniaxial Loads". *Journal of Structural Engineering* 36, 1 (o. J.): 11–15.

10 Glossary of terms used in NDT-CE vs. Seismics

Table 10-1: Glossary

NDT term	Seismic/geophysical term	Remarks
monostatic	constant offset	Refers to distance source-receiver
multi-static	multiple offsets	As above
Reconstruction or imaging	migration	Focusing the reflected energy to points of origin (reflectors), producing images of the subsurface
A-scan	(seismic) trace	Single time series from a specific source-receiver combination
B-scan	seismic section, seismogram	Set of traces/A-scans acquired along a line on the surface or vertical section through a data volume. Vertical coordinate of a B-Scan might be time or depth. Perpendicular vertical sections are sometimes calls D-scans.
C-scan	time slice	Horizontal slice through a data volume (traces/A-scans acquired over an area) for a certain time or depth
array	array	Set of transmitters/receivers. It might either refer to a group of transmitters or receivers, which are coupled together as a single channel or of a group of transmitters/receivers which are controlled separately (e. g a phased array or a multi-static device). Arrays of arrays also exist.
radar	Ground Penetrating Radar (GPR)	
Source function, Point spread function	Source function, source wavelet	Mathematical description of source excitation. May or may not include directional characteristics.

11 Addendum/Erratum to section 6.4.5

Section 6.4.5 contains an issue simplification concerning the temperature development in the specimen under test, which was not properly discussed at the time of writing. This does not affect the successful demonstration of coda wave imaging. However, one of the reviewers remarked that it must be addressed in more detail. The author agrees.

In this section the authors performed and evaluated an ultrasonic time lapse experiment on a large concrete model, subjected to a temperature anomaly by a heat cartridge. As a part of the data acquisition system failed, just very sparse temperature data were recorded while the ultrasonic data were recorded without problems. Due to the time schedule of the involved researchers there was no opportunity to repeat the measurement at that time.

To provide some means to evaluate the ultrasonic velocity anomaly detected in the concrete model, the authors tried to back-calculate the temperature field at the time of measurement from the very sparse temperature data using several assumptions and simplifications:

1) The geometry was simplified to a 2D infinite inhomogeneous medium (in the original manuscript, 3D was noted, but this was a typo. All equations and calculations are 2D).
2) Any boundary conditions (insulated boundaries at sides and bottom, free surface on top) and the changing surrounding atmospheric temperatures have been neglected.
3) Any parameters in the equations were selected to fit the existing temperature data, not necessarily meeting literature values.

Based on this the 2D temperature values in a horizontal section of the model at the time of the ultrasonic measurements have been calculated (Figures Figure 6-40 and Figure 6-41), and compared with the ultrasonic results, showing some qualitative correlation.

A more realistic approximation of the temperature problem would be a rectangular parallelepiped (neglecting a bearing out on side of the body) with constant or periodic boundary conditions. Analytic or semi analytic solutions for the 3D heat equation and several types of initial and boundary conditions are known since long [1]. They are based either on a Fourier series or Greens Function approach. However, homogeneity or other assumption are made and convection at the free surface is not considered.

As more experiments are planned at this concrete model for 2020, it was decided to set up a full numerical model, which can be extended later to include any geometry deviations, various objects inside the model and arbitrary boundary conditions. In a first step, a homogeneous parallelepiped was modeled (neglecting the bearing out on one side of the body), using realistic boundary conditions (including the 10 cm Polystyrene at the bottom and the sides), atmospheric temperatures at the top surface and a small cylindrical heat source at the correct location. Abaqus [2] was chosen as a finite element solver. All calculations were carried out at Ruhr-Universität Bochum by Felix Clauss (whose support is highly appreciated).

The temperature dependent material properties for the simulation were selected according to the Eurocode [3], which does give ranges for the respective parameters. The range for the thermal conductivity and specific heat are shown in Figure 11-1 and Figure 11-2, respectively. Important simulation parameters are given in Table 11-1. The grid is shown in Figure 11-3.

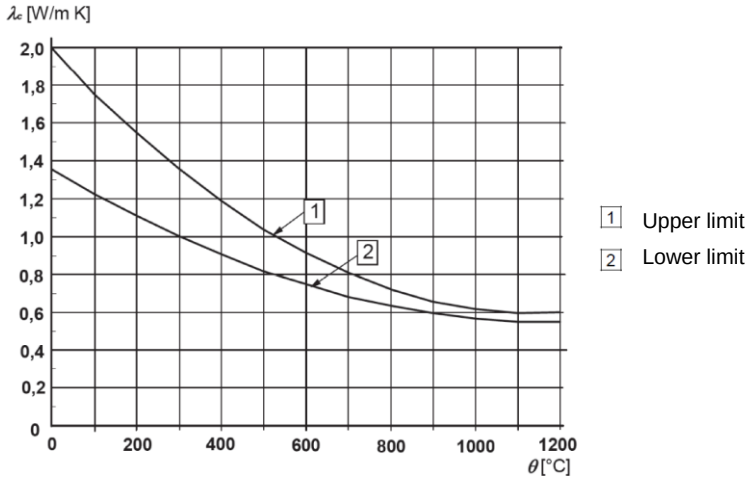

Figure 11-1: Thermal conductivity of concrete according to Eurocode [3]. The lower limit values were used for the simulation shown in Figure 11-4.

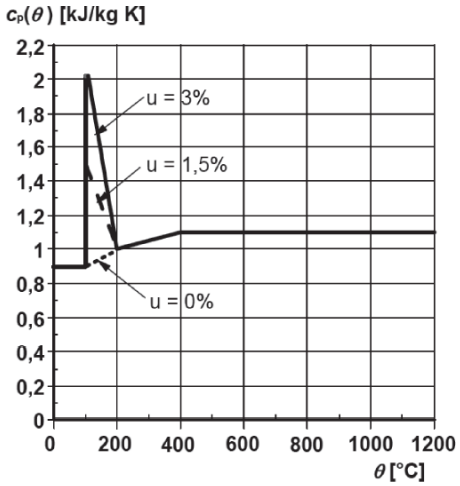

Figure 11-2: Specific heat of concrete according to Eurocode [3] for various moisture contents (u). As the concrete model has a free weather exposed surface and the measurements were done in spring, the maximum curve (u = 3%) was used for the simulation shown in Figure 11-4.

Table 11-1: Simulation parameters (thermal parameters of concrete see figures)

parameter	Value
Software	Abaqus 6.14
Equation	3D heat conduction
Polystyrene density	10 $kg \cdot m^{-3}$
" thermal cond.	0,035 $W \cdot m^{-1} \cdot K^{-1}$
" specific heat	1500 $J \cdot kg^{-1} \cdot K^{-1}$
Concrete density	2400 $kg \cdot m^{-3}$ (for T ≤115 °C), decreasing to 2250 $kg \cdot m^{-3}$ (for T = 550 °C)
Mean ambient temperature	11 °C
Total time simulated	32 h
Time step	Default: 900s, automatically adapted when instabilities occurred
Cell size	Varying 10 cm – 1 mm (see Figure 11-3)
Calculation time	6,5 h – 8 h (17 CPUs)

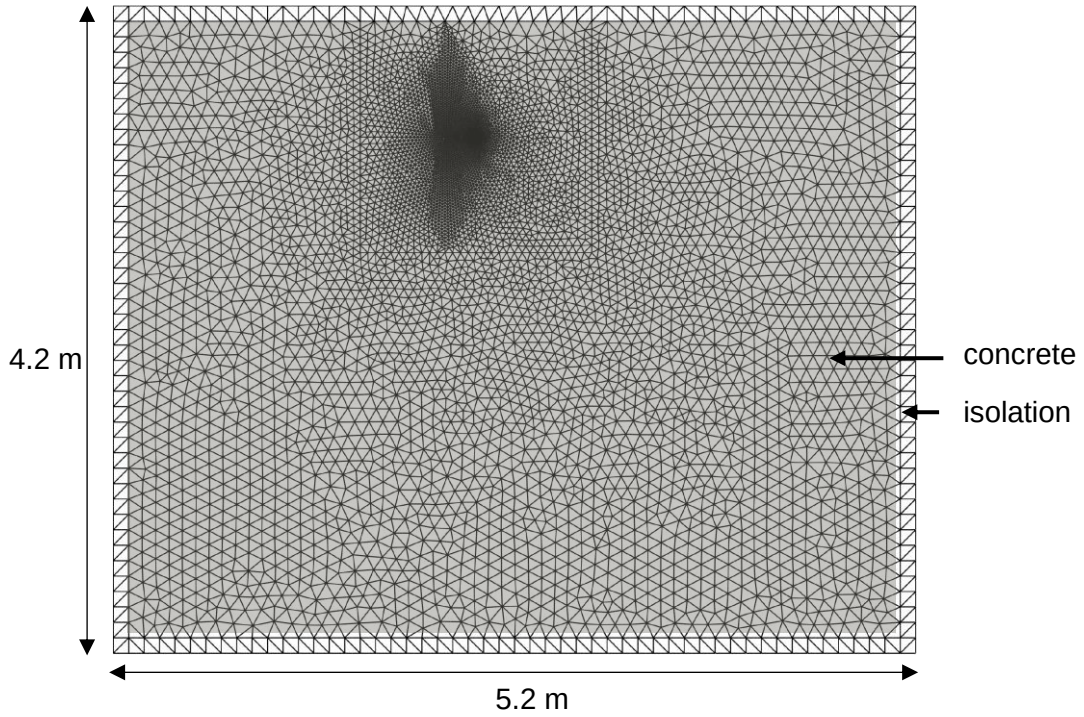

Figure 11-3: Simulation grid, top view, cross section at level of ultrasonic trasnducers (4 m x 5m of concrete, 10 cm of polystyrene isolation)

The simulations have been carried out using several combinations of material parameters. The results shown in Figure 11-4 were calculated using the maximum specific heat and the minimum heat capacity given by the Eurocode, resulting in the highest temperature level close to the cartridge.

The shape of the temperature anomaly in the horizontal cross section (Figure 11-4, top) resembles the shape of the temperature anomaly estimated in section 6.4.5, Figure 6-41, except the distortion towards the boundary (not taken into account in the earlier calculations), supporting the cause that the ultrasonic monitoring technique was able to pinpoint the affected area correctly (within the limitations stated in section 6.4.5).

However, the amplitude of the anomaly is different. In the simulation shown here, the temperature at the position of the heat cartridge was about 3°C above the ambient temperature at the time of the ultrasonic measurement, while sensor readings in 2014 were close to 500 °C. In fact, the simulation results are closer to what was to be expected from the ultrasonic results than the temperature sensor readings. The maximum ultrasonic velocity change (center of the anomaly in Figure 6-43 left) is about 1%, giving a temperature dependence of -0.33 % per K. Earlier investigations on the temperature dependence of ultrasonic velocity of concrete have given values around -0.16 % K^{-1} [4], with somewhat lower values in an investigation performed by the authors of this thesis (-0.05 % per K^{-1}, [5]). Note, that these values are for small, reversible changes in the range of 0 °C to 50 °C. The difference in magnitude can be related to permanent changes due to two hours of excessive heating at T > 500 °C. This is supported by the changes in scattering cross section detected by the ultrasonic experiments around the heat cartridge (Figure 6-43 right).

Still, the temperature change which can be expected from the ultrasonic results (-1% velocity change equals a temperature rise of around 20 K) are much closer to the simulation results than the to the measured temperature values. As a result, the temperature readings at the sensors must be doubted. The experiment should be repeated with new and

additional sensors, together with an optimized arrangement of ultrasonic transducers (e. g. use of embedded transducers instead of external ones). Unfortunately, this was not possible due to logistic limitations at BAM before the deadline of the publication of this work.

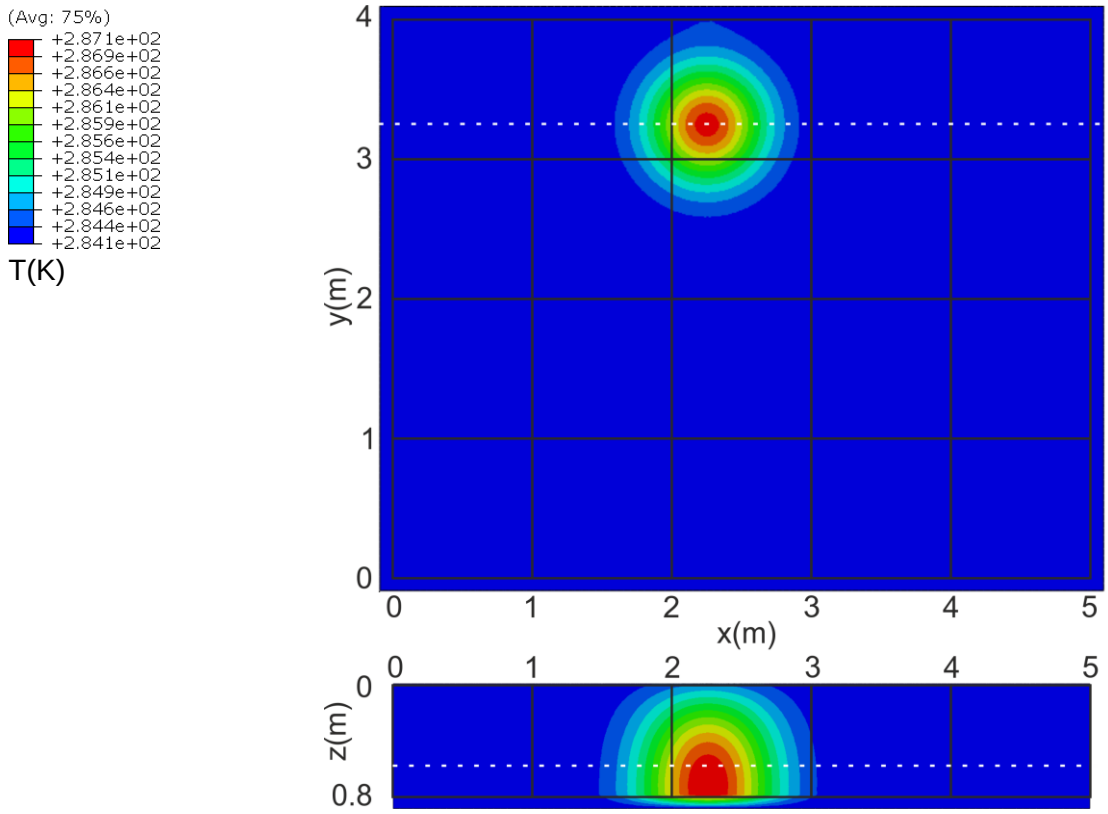

Figure 11-4: Result of the simulation: Temperature distribution in K at time of ultrasonic measurements. Top: Horizontal cross section at level of ultrasonic transducers. Bottom: vertical cross section at position of heat cartridge. Grid shows concrete part of the model. Dashed white lines: Intersection of sections.

References

[1] Carslaw, H.S., & Jaeger, J. C., 1959: Conduction of Heat in Solids. Oxford University Press, Oxford, UK.

[2] DS Simulia: Abaqus 6.14, Abaqus/CAE User's Guide. http://ivt-abaqusdoc.ivt.ntnu.no:2080/v6.14/books/usi/default.htm, Downloaded 019-10-22.

[3] Norm DIN-EN1992-1-2:2004 + AC:2008: Eurocode 2: Bemessung und Konstruktion von Stahlbeton- und Spannbetontragwerken. Teil 1-2: Allgemeine Regeln – Tragwerksberechnung für den Brandfall.

[4] Planès, T., & Larose, E. (2013): "A Review of Ultrasonic Coda Wave Interferometry in Concrete". *Cement and Concrete Research* 53: 248–55. doi:10.1016/j.cemconres.2013.07.009.

[5] Niederleithinger, E., & Wunderlich C. (2012): "Influence of small temperature variations on the ultrasonic velocity in concrete". In *Proceedings of QNDE 2012*, 390–97. Denver. doi:10.1063/1.4789074.